# archives of thermodynamics

QUARTERLY

## Aims and Scope

The aim of the quarterly journal Archives of Thermodynamics (AoT) is to disseminate knowledge between scientists and engineers worldwide and to provide a forum for original research conducted in the field of thermodynamics, heat transfer, fluid flow, combustion and energy conversion in various aspects of thermal sciences, mechanical and power engineering. Besides original research papers, review articles are also welcome.

The journal scope of interest encompasses in particular, but is not limited to:

| | |
|---|---|
| Classical and extended non-equilibrium thermodynamics, | Energy transition, |
| Thermodynamic analysis including exergy, | Advanced energy carriers, |
| Thermodynamics of heating and cooling, | Energy storage and efficiency, |
| Thermodynamics of nuclear power generation, | Energy in buildings, |
| Thermodynamics in defense engineering, | Hydrogen energy, |
| Advances in thermodynamics, | Combustion and emissions, |
| Experimental, theoretical and numerical heat transfer, | Turbomachinery, |
| Thermal and energy system analysis, | Thermal energy conversion, |
| Renewable energy sources including solar energy, | Integrated energy systems, |
| Secondary fuels and fuel conversion, | Distributed energy generation, |
| Heat and momentum transfer in multiphase flows and nanofluids, | Thermal incineration of wastes and waste heat recovery. |

# archives
# of thermodynamics

## Editorial Office

**Terms of subscription outside Poland**

Annual subscription rate outside Poland (2023) is 152 EUR. Price of single issue is 38 EUR. Previously published volumes are available on request. Subscription orders should be sent directly to **IMP PAN Publishers, The Szewalski Institute of Fluid Flow Machinery PASci, ul. Fiszera 14, 80-231 Gdansk, Poland**; dr Jarosław Frączak, phone: (+48) 58-52-25-230; e-mail: jfrk@imp.gda.pl. Payments should be transferred to the bank account of IMP PAN: IBAN 28 1130 1121 0006 5498 9520 0011 at Bank Gospodarstwa Krajowego; Code SWIFT: GOSKPLPW

**Warunki prenumeraty w Polsce**

Roczna prenumerata (2023 r.) wynosi 260.00 PLN. Cena pojedynczego numeru wynosi 65.00 PLN. Osiągalne są również wydania archiwalne. Zamówienia z określeniem okresu prenumeraty, nazwiskiem i adresem odbiorcy należy kierować bezpośrednio do Wydawcy (Instytut Maszyn Przepływowych im. R. Szewalskiego PAN, ul. Fiszera 14, 80-231 Gdańsk, dr Jarosław Frączak, e-mail: jfrk@imp.gda.pl). Wpłaty prosimy kierować na konto Instytutu Maszyn Przepływowych PAN nr 28 1130 1121 0006 5498 9520 0011 w Banku Gospodarstwa Krajowego

**Articles in** *Archives of Thermodynamics* **are abstracted and indexed within:**

Applied Mechanics Reviews • Arianta • Baidu Scholar • BazTech • Cabell's Directory • Celdes • Chemical Abstracts Service (CAS) – CAplus • CNKI Scholar (China National Knowledge Infrastucture) • CNPIEC • EBSCO (relevant databases) • EBSCO Discovery Service • Elsevier – SCOPUS • ESCI (Emerging Sources Citation Index) • Genamics JournalSeek • Google Scholar • Inspec • Index Copernicus • J-Gate • Journal TOCs • Naviga (Softweco) • Paperbase • Pirabase • POL-index • Polymer Library • Primo Central (ExLibris) • ProQuest (relevant databases) • ReadCube • Referativnyi Zhurnal (VINITI) • SCImago (SJR) • Summon (Serials Solutions/ProQuest) • TDOne (TDNet) • TEMA Technik und Management • Ulrich's Periodicals Directory/ulrichsweb • WorldCat (OCLC)

Typeset in LaTeX by
    Drukarnia Braci Grodzickich Sp.j. 05-500 Piaseczno, ul. Geodetów 47a

Printed and bound by
    Gimpo, 02-858 Warszawa, ul. Transportowców 11

# Contents

# Impact of raw liquid natural gas composition on combustion properties and emission characteristic

**PAWEŁ CZYŻEWSKI**[*]
**RAFAŁ ŚLEFARSKI**
**JOANNA JÓJKA**

Poznan University of Technology, Institute of Thermal Energy,
Piotrowo 3a, 60-965, Poznan, Poland

**Abstract** The article presents the results of numerical and analytical investigations of the influence of raw liquid natural gas (LNG) composition on parameters characterizing the combustion process. The high content of higher hydrocarbons influences the thermodynamic combustion process described with parameters like the adiabatic flame temperature, laminar flame speed and ignition delay time. A numerical study of the impact of LNG fuels on emission characteristics using the Cantera code has been performed. Results have shown that the change of grid natural gas to some types of liquid natural gas can result in an incomplete combustion process and an increase of emission of toxic compounds such as carbon monoxide and unburned hydrocarbons. For all investigated fuels the laminar flame speed rises by about 10% compared to natural gas, while the adiabatic flame temperature is nearly the same. The ignition delay time is decreased with an increase of ethane share in the fuel. The analysis of chemical pathways has shown that hydrogen cyanide and hydrogen formation is present, particularly in the high temperature combustion regimes, which results in an increase of nitric oxide molar fraction in flue gases by even 10% compared to natural gas. To summarize, for some applications, liquid natural gases cannot be directly used as interchangeable fuels in an industry sector, even if they meet the legal requirements.

**Keywords:** Toxic compounds; Fuel flexibility; Liquid natural gas; NO emission

---

[*]Corresponding Author. Email: pawel.czyzewski@put.poznan.pl

**Nomenclature**

| | | |
|---|---|---|
| $d$ | – | relative density of fuel |
| HFL | – | higher flammability limit, % |
| HHV | – | higher heating value, MJ/Nm$^3$ |
| LHV | – | lower heating value |
| LFL | – | lower flammability limit, % |
| MN | – | methane number |
| $T$ | – | temperature, K |
| $p$ | – | pressure, Pa |
| $X_i$ | – | mole fraction of fuel components |
| $T_A$ | – | adiabatic flame temperature, K |
| $S_L$ | – | laminar flame speed, m/s |
| $T_I$ | – | ignition temperature, K |
| $t$ | – | time, s |
| $t_d$ | – | ignition delay time |
| $V_a$ | – | volume of theoretical combustion air, Nm$^3$ |
| $V_f$ | – | volume of fuel, m$^3$ |
| Wb | – | Wobbe index, MJ/Nm$^3$ |

**Greek symbols**

| | | |
|---|---|---|
| $\lambda$ | – | air excess ratio |
| $\rho$ | – | density, kg/m$^3$ |

**Acronyms**

| | | |
|---|---|---|
| AVL | – | Adelson–Velsky and Landis method |
| EU | – | European Union |
| HC | – | hydrocarbons |
| HCN | – | hydrogen cyanide |
| LNG | – | liquid natural gas |
| NCN | – | cyanonitrene |
| NG | – | natural gas |

# 1    Introduction

The achievement of the energy transition objectives enforced by the EU climate legislation [1] is based on the assumption of the use of natural gas (NG) as a transfer fuel between fossil fuels and a system based on the use of zero-emission sources. NG is approved as a carrier that allows the compensation of energy shortages from unstable renewable energy sources [2,3]. In view of the inadequacies of the available energy storage methods [2], natural gas is a fuel that offers the possibility of being utilized in systems with the possibility of high power generation with a rapid start-up time [5,6]. Until recently, this development was accompanied by attractive natural gas prices

that were not competitive with coal [7,8] while incurring lower carbon dioxide emission costs [3] making the use of natural gas for electricity generation a favorable method to reduce carbon dioxide emissions [4]. The generation of a unit of electricity in the combustion of natural gas contributes to two times less emission of carbon dioxide compared to the combustion of coal. These factors have resulted in a very dynamic process of increasing the share of energy produced from natural gas in the energy mix of many countries. A diametrical change in the NG market occurred in 2021, when, after a period of low prices for imported natural gas, a drastic several-fold increase in its price was observed. It was caused by an imbalance in the market resulting from the post-pandemic economic recovery and then the geopolitical situation related to Russia's military invasion of Ukraine. This has triggered a trend of turning away from Russian NG and the need to revise the existing energy policy towards seeking alternative solutions. One of them involves drastically increasing the use of natural gas transported by ships in the form of liquid natural gas (LNG) from countries distant from Europe.

Nowadays, LNG constitutes a large part of NG consumption and represents 36% [5] of the world natural gas market (for many countries covering even total fuel consumption) and is forecasted to get the majority of the gas market in 2035 (this trend can be accelerated by abandoning Russian NG). This situation implies that obstacles related to LNG consumption will be playing an important role, especially in the nearest future [6,7]. The diversification of natural gas supplies by increasing the share of LNG and gas from multiple geological deposits of different world regions requires analysis of the impact of their physical and chemical parameters on the combustion process and its emission.

In general imported liquefied gas contains more higher hydrocarbons [8] and is characterized by a different level of impurities. It involves many subsequent issues regarding their further utilization in energetic devices and the resulting emissions of carbon dioxide and toxic substances to the atmosphere. A great importance should be attached to the connection between the properties of the flammable mixture and final maintenance/emission outcomes. Many parameters describing the properties of natural gas and its utilization are applied [7]. These determining the most important impact are: lower heating value, energy content, combustion characteristics, impurities content, the Wobbe index, methane number [9], European standards compatibility, sulfur compounds content, dioxygen ($O_2$) and carbon dioxide ($CO_2$) shares, water and hydrocarbons dew points, damage risk, safety, burner controls, billing and Joule–Thomson effect.

Due to the fluctuations of nominal electricity production from renewable energy sources such as wind power and photovoltaics as well as the inadequacies of existing energy storage methods [2, 3], the import of electricity would not be able to replenish energy shortages in the absence of windy and overcast days. Most available energy storage technologies [10] require considerable financial, material and spatial efforts. For the time being, the most favourable method to overcome these obstacles to ensure the stable supply of electricity while reducing carbon emissions is the utilization of natural gas.

Unlike coal-fired steam boilers [11] supplying steam turbines, natural gas powered turbines [12] and engines have the ability to be quickly deployed and in the case of gas-steam systems, generate amounts of electricity comparable even to those fired with coal [13].

The energy policy of most industrialized countries is impacted by undertaking efforts to develop the potential of natural gas imports and to increase the diversification of supply sources. These include the planning and construction of many LNG terminals (14 units) [14] and pipelines connecting them with existing natural gas infrastructure [15]. The former European LNG market was focused on terminal operators in France, Spain, Italy, Belgium and the Netherlands. Recently, the Baltic Sea basin countries like Poland, Sweden, Lithuania and Finland have joined the group of European importers with their own LNG terminals.

LNG composition is usually different from the composition of natural gas supplied in onshore natural gas transmission networks (Table 1). This

Table 1: Example of liquid natural gas compositions at several LNG production locations [16]

| Source name | LNG composition (%vol) | | | | |
|---|---|---|---|---|---|
| | $CH_4$ | $C_2H_6$ | $C_3H_8$ | $C_4H_{10}$ | $N_2$ |
| Alaska | 99.72 | 0.05 | 0.01 | 0.00 | 0.22 |
| Algeria (Arzew) | 86.98 | 9.35 | 2.33 | 0.63 | 0.71 |
| Baltimore Gas&Electric | 93.32 | 4.65 | 0.84 | 0.18 | 1.01 |
| San Diego Gas&Electric | 92.00 | 6.15 | 0.95 | 0.20 | 0.70 |
| Qatar | 90.90 | 6.43 | 1.66 | 0.74 | 0.27 |
| Australia NWS | 86.26 | 8.23 | 3.29 | 0.96 | 1.26 |
| Malaysia | 91.69 | 4.64 | 2.60 | 0.93 | 0.14 |
| Russia – Sakhalin | 92.54 | 4.47 | 1.97 | 0.95 | 0.07 |
| Nigeria | 91.60 | 5.64 | 2.15 | 0.58 | 0.03 |
| Norway | 92.03 | 5.75 | 1.31 | 0.45 | 0.46 |
| Gas E (NG) | 94.67 | 1.20 | 0.40 | 0.40 | 3.33 |

situation implies that obstacles related to LNG consumption will play an important role, especially in the nearest future.

This article deals with a comprehensive analysis of LNG mixed natural gases utilization in EU public transmission systems.

## 2 Methods

The gaseous fuel introduced to the EU countries' transmission and distribution networks should meet the quality parameters described in different legal regulations of individual Member States on special conditions for the functioning of the gas system [17]. These document concern the minimum value of the higher heating value (HHV) for gaseous fuels with the Wobbe index (Wb). For high-methane natural gas of group E, the Wobbe index (Wb) is ranging from 45 MJ/m$^3$ to 56.9 MJ/m$^3$. Further regulations (ISO 13686:2013(en) [18]) define other quality parameters for gaseous fuels such as:

- hydrogen sulfide content $< 7$ mg/m$^3$,

- mercaptan sulfur content $< 16$ mg/m$^3$ (ISO 6326-3:1989(en) [19]),

- total sulfur content $< 40$ mg/m$^3$ (ISO 6326-1:2007)(en), ISO 6326-5:1989(en)),

- content of mercury vapor $< 30$ μg/m$^3$ (ISO 6978-1:2003(en) [20], ISO 6978-2:2003(en) [21]),

- dew point temperature $+3.7$°C (since 1st of Apr. to 30th of Sept.) and $-5$°C (since 1st of Oct. to 31st of March) (ISO 6327:1981(en) [22]).

One of the basic parameters determining the possibility of the various gaseous fuels replacement is the Wobbe index, which refers to the amount of chemical energy contained in the fuel stream. The values of basic quality parameters of gaseous fuels are based on the molar composition of the fuel obtained as a result of chromatographic analysis and standardized corresponding with ISO procedure (ISO 6976:2016 [23]).

The Wobbe index is calculated as the ratio of heat of combustion related to the unit of the volume of gaseous fuel to the square root of its relative density:

$$\mathrm{Wb} = \frac{\mathrm{HHV}}{\sqrt{d}} \,. \tag{1}$$

The relative gas density $d$ stands for the ratio of the natural gas density and air density under the same reference conditions. The following calculations represent in general open systems placed inside manufacturing facilities, operating at the ambient pressure of 101325 Pa and temperature of 298.15 K. For the standardized volumetric flow (ISO 13443:1996 [24]), the reference values are corresponding to the normal gas state ($p = 101325$ Pa and $T = 273.15$ K).

The second group of physicochemical parameters characterizing the interchangeability of gaseous fuels are the operating parameters associated with the combustion process such as: the unitary amount of air needed to completely combust the supplied fuel ($V_a/V_f$), the lower and upper flammability limit of the gas mixture (LFL, HFL) and the methane number (MN).

The quantity of air needed to completely burn the fuel unit is determined based on the stoichiometric equations of the fuel oxidation process. Assuming a molar fraction of oxygen in the air at the level of 0.21, this dependence takes the form:

$$\frac{V_a}{V_f} = \frac{1}{0.21}\left[2X_{\mathrm{CH4}} + 0.5\left(X_{\mathrm{CO}} + X_{\mathrm{H2}}\right) + \left(m + \frac{n}{4}\right)\mathrm{C}_m\mathrm{H}_n - X_{\mathrm{O2}}\right], \quad (2)$$

where $X_i$ is the molar ratio of individual fuel components.

Lower and upper flammability limits refer to the lower and upper limit of the gaseous or vaporized fuel concentration in the air at a fixed temperature and pressure respectively which can lead to flame propagation. The values of LFL and HFL for fuel mixtures can be calculated based on the formulas:

$$\mathrm{LFL} = \frac{1}{\displaystyle\sum_{i=1}^{n}\frac{x_i}{\mathrm{LFL}_i}}, \quad (3)$$

and

$$\mathrm{HFL} = \frac{1}{\displaystyle\sum_{j=1}^{n}\frac{x_i}{\mathrm{HFL}_i}}, \quad (4)$$

where $\mathrm{LFL}_i$ and $\mathrm{HFL}_i$ are the lower and upper limits of individual components of gaseous fuel, and $n$ is the number of flammable components.

The next important parameter which can be used as an interchangeability factor of gaseous fuels is methane number. The methane number describes resistance to auto-ignition of fuel and thus engine knock resistance when operating with a given fuel. For gaseous fuels, the value of MN is in

the range from 0 (for hydrogen) up to 100 (for methane). Knock resistance is rising with the MN increase. The value of methane number can be calculated based on many numerical codes created mostly on data delivered by Leiker *et al.* [25] or using the methodology presented by Kubesh [26]. For the purpose of industrial applications, a simplified method based on the ISO standard (ISO/TR 22302:2014) can be used. Other commonly used methods are the linear correlation method, hydrogen/carbon (H/C) ratio method or AVL method.

The last group of parameters which describe gaseous fuels are the thermodynamics properties of the combustion process such as the adiabatic flame temperature ($T_A$) [28], laminar flame speed ($S_L$) [29] and self-ignition temperature ($T_I$) [30]. These parameters define the selection of appropriate combustion technology and influence on the stability of the combustion process. The adiabatic flame temperature is the maximum temperature that can be obtained after the complete combustion process without heat losses to the surroundings. The value of $T_A$ for different fuel blends can be calculated using numerical codes which take into account detailed combustion kinetics such as Chemkin-PRO or Cantera [31]. $T_A$ depends on the initial parameters of substrates like temperature and pressure. Reaction mechanisms are based on the experimental measurements and validated [32, 33], where $T_A$, $S_L$ and $T_I$ are considered especially important parameters as characteristic mixture properties. The second parameter which can be obtained using numerical modelling of the combustion process is the laminar flame speed $S_L$ [32]. The $S_L$ is the velocity at which the flame front is moving in relation to the fresh gases in one-dimensional geometry [29]. The value of $S_L$ is influenced by the fuel composition, excess of air as well as temperature and pressure of substrates ($S_L$ decreases with the growth of pressure and increases with the growth of temperature of reagents). For stoichiometric flames at normal substrates conditions, $S_L$ values range from 5 (for carbon monoxide) to 280 cm/s (for hydrogen), being around 42 cm/s for pure methane [33]).

A parameter characterizing gaseous fuels which can be delivered from numerical modelling is the ignition temperature. According to the definition presented by Le Chaterier, $T_I$ is the minimum temperature for which the amount of heat delivered from the combustion process is higher than the amount of heat lost to the preheating zone of reactants. For initial substrates' temperatures higher than the ignition temperature, a specific time interval could be noticed with a temperature peak as well as with the pressure rising. Proceeding further, autoignition is the spontaneous homo-

geneous ignition of the fuel-air mixture. The time for a mixture to reach autoignition is referred to as the ignition delay time, which is strongly dependent on the reactivity of the mixture [36–38].

In this work, the thermodynamic properties of gaseous fuels ($T_A$, $S_L$ and $T_I$) were calculated using a 1D FreeFlame combustion model from the Cantera software libraries [34]. The mechanism UC SanDiego was chosen as a representation of C1–C4 combustion chemistry, which includes NOx formation pathways [35]. The FreeFlame model represents a freely propagating flat reaction front including the reacting mixture movement and its transport properties. Calculations were conducted using a procedure, which was developed and validated for an axisymmetric methane-air flame with an approximate combustion chamber length of 0.5 m [36]. Estimation of the combustion chamber length was introduced as a linear grid, which was automatically refined with a slope and curvature control of 0.06 and 0.12, respectively. The calculated flame front propagated initially with the laminar burning velocity using mixture-averaged transport properties. The highest value of the temperature achieved by the modelled gas was the adiabatic flame temperature. This initial solution for each tested point was recalculated using a multicomponent transport in order to improve predictions of emissions and $S_L$. For the adiabatic flame temperature and the laminar flame speed, inlet mixture gas state parameters were kept at the constant level for all investigated LNG gases ($T = 300$ K and $p = 101325$ Pa), while the air excess ratio was changed in the range from 0.8 up to 1.8. Nitric oxide (NO) and carbon monoxide (CO) emission calculations were conducted using FreeFlame model with a radiative heat loss and a burner-stabilized BurnerFlame model. The BurnerFlame model was introduced to compare the CO emission when a fuel change was performed without an adjustment of the air stream. The air/fuel ratio of NG was a reference value. The performed simulations of non-adiabatic flames were in a better correlation to the mentioned NG burner tests [36] than those of perfectly insulated adiabatic flames, because of intensified heat exchange between the reacting mixture and surroundings. All emission values were recalculated to the dry reference base.

The ignition temperature and the ignition delay time ($t_d$) were calculated using a 0D model designed for the present investigations [37]. Each $T_I$ as well as $t_d$ value was obtained from a reactor filled with a perfectly stirred combustible mixture and surrounded by a non-expanding adiabatic wall. Rising the substrates' initial temperature to the mixture ignition temperature resulted in the initiation of the spontaneous exothermal reactions,

which affected the pressure and temperature of the modelled closed vessel. The calculated $T_I$ was the lowest substrates' initial temperature for which the heat release was greater than the preheat zone consumption, and the combustion process started. The ignition delay time for selected fuels could be determined in two ways. First, as a relation between the reactor pressure change and time $\mathrm{d}p/\mathrm{d}t$, and second, as a specified temperature change given in absolute values $\Delta T$. In the divergent formulation, the $\mathrm{d}p/\mathrm{d}t$ function is examined and the simulation time corresponding to the maximum value of the function corresponds to the ignition delay time. For selected LNG and NG compositions, the initial temperature range from 800 K to 900 K was tested for a stoichiometric mixture with a 1 K step and an overall simulation time of 10 s with a $10^{-6}$s time step. The mixture ignition temperature was marked as an initial mixture temperature if the combustion process occurred at a time below the total simulation time. Further investigations with the ignition delay time were performed for the before mentioned conditions. The initial temperature of the mixture was raised from 800 K to 1400 K with a 1 K step. The simulation time, where a significant temperature rise was observed as a mixture ignition delay time was compared to the value obtained by a divergent formulation approach. The temperature change between the following time steps $\Delta T$ at the end of mixture preheating was estimated at 5 K. The marked calculation point corresponds to the peak of the pressure function $\mathrm{d}p/\mathrm{d}t$ and results in the gas temperature value of approximately 50% of the adiabatic flame temperature.

## 3 Results and discussion

### 3.1 Physicochemical properties of LNG

As it was mentioned in the previous chapter, the composition of natural gas obtained after the regasification process of LNG varies from that of natural gas delivered by the transition system. The major difference is the amount of high hydrocarbons that influence many physicochemical and thermodynamic parameters of fuel. The natural gas parameters received after the regasification process of LNG calculated based on Eqs. (1)–(4) are presented in Table 2. The methane number was found from the numerical code MWN_MN delivered by the European Association of Internal Combustion Engine Manufacturers [38].

As it is shown in Table 2, all investigated fuels fulfil the requirements of most EU market legislation acts with respect to the high heating value and

Table 2: Physico-chemical properties of LNG gases

| LNG source name | $\rho$ | $d$ | HHV | Wb | $V_a$ | LFL | HFL | MN |
|---|---|---|---|---|---|---|---|---|
| | (kg/m$^3$) | (–) | (MJ/Nm$^3$) | (MJ/Nm$^3$) | (Nm$^3_{air}$) | (%) | (%) | (–) |
| Alaska | 0.717 | 0.555 | 39.66 | 53.24 | 9.5 | 5.3 | 15.0 | 99.8 |
| Algeria (Arzew) | 0.819 | 0.634 | 44.19 | 55.50 | 10.6 | 4.8 | 14.5 | 71.0 |
| Baltimore Gas & Electric | 0.764 | 0.591 | 41.38 | 53.81 | 9.9 | 5.1 | 14.9 | 82.8 |
| San Diego Gas & Electric | 0.771 | 0.597 | 41.72 | 54.01 | 10.0 | 5.0 | 14.9 | 81.4 |
| Qatar | 0.792 | 0.613 | 43.19 | 55.16 | 10.4 | 4.9 | 14.6 | 74.5 |
| Australia NWS | 0.833 | 0.645 | 44.50 | 55.41 | 10.7 | 4.7 | 14.5 | 68.6 |
| Malaysia | 0.796 | 0.616 | 43.43 | 55.35 | 10.4 | 4.9 | 14.6 | 73.0 |
| Russia – Sakhalin | 0.787 | 0.609 | 43.05 | 55.18 | 10.3 | 4.9 | 14.6 | 74.6 |
| Nigeria | 0.792 | 0.613 | 43.33 | 55.36 | 10.4 | 4.9 | 14.5 | 74.9 |
| Norway | 0.779 | 0.603 | 42.45 | 54.67 | 10.2 | 5.0 | 14.7 | 77.8 |
| Gas E (NG) | 0.754 | 0.583 | 39.36 | 51.54 | 9.4 | 5.4 | 15.4 | 90.4 |

Wobbe index. For all LNG fuels, the HHV was higher than 34 MJ/Nm$^3$ and Wb was lower than 56.9 MJ/Nm$^3$. According to Barczynski and Łaciak [39], the energetic devices for domestic solutions should be supplied with natural gas with the Wobbe index changing within the range of $\pm 5\%$, which gives the absolute margin value of 2.6 MJ/Nm$^3$ for gas E (natural gas – base case). As it can be observed for LNG gases with a high content of high hydrocarbons, the difference between the value of Wb for certain fuels and gas E is even higher than 7% (LNG sources like: Qatar, Australia, Malesia and Algeria). It means that these fuels can be used as interchangeable fuels only for industrial devices where the easiest correction of the combustion process parameters is possible. Another important parameter is the amount of air delivered to the combustion process, which for the gas E group is equal to about 9.4–9.5 m$^3$ of air per one Nm$^3$ of fuel. The calculated value of $V_a$ (air volume) has shown that for some LNG sources, this value is even more than 10% higher than that for natural gas delivered by transition networks, which introduces the risk of an incomplete oxidation process of fuel components and intensified emission of toxic compounds such as carbon monoxide (CO) or unburned hydrocarbons. The incomplete combustion process results also in a decrease of the combustion efficiency [40]. The higher content of hydrocarbons in the fuel causes a decrease of fuel knocking combustion resistance in a great part of energetic devices – reciprocating gas engines. For LNG fuels with the overall amount of high hydrocarbons above 7% (Qatar, Australia, Malesia and Algeria), the value of MN decreases

by even 30% compared to that of gas E. Complete interchangeability of the above-mentioned fuels requires modification of gas engine operating parameters such as the ignition delay time, engine boost and composition of combustion mixtures [41]. Even a slight shift of the range of engine working parameters can introduce recurring instabilities into the cycle, in some cases resulting in engine failure. In an extreme case, it can induce the engine stop. For example, the gas engine provider Westport Company require the usage of fuel with a minimum methane number of 75 for engines ISL G and ISX12 G [42].

In the case of lower and upper flammability limits for natural gas from the regasification process of LNG, the change is negligible. The higher amount of hydrocarbons in the fuels shifts the LFL to the lower values, which can result in an easier ignition of gas-fuel mixtures.

The influence of LNG composition on the laminar flame speed, the adiabatic flame temperature as well as ignition parameters has been numerically studied for five LNG gas compositions with Norway gas and grid natural gas as base cases (Table 3).

Table 3: Numerical calculation input

| LNG source name | Fuel name | Initial calculation parameters | | |
|---|---|---|---|---|
| | | $T_{sub}$ | $p_{sub}$ | Air excess ratio |
| Algeria (Arzew) | LNG1 | | | |
| Qatar | LNG2 | | | |
| Russia – Sakhalin | LNG3 | 300 K | $10^5$ Pa | 1–1.8 |
| Baltimore Gas & Electric | LNG4 | | | |
| Norway | LNG5 | | | |
| Gas E | NG | | | |

Results of numerical calculations of the laminar flame speed and adiabatic flame temperature are shown in Fig. 1 [16] (the air excess ratio was calculated according to formula $\lambda = (20.9\%)/(20.9\% - O_2 \text{ m}\%)$, where $O_2$ m% is the measured volume value of oxygen in the dry exhaust gases). In both cases, it can be observed that for all investigated LNG gases the influence of fuel composition is negligible. For the calculation of $T_A$, the maximum difference was around 5 K (for LNG1) for the whole studied air excess ratio. It results from the adiabatic flame temperature definition, where the maximum temperature depends mostly on the amount of energy delivered from the fuel/air mixture and processes such as thermal dissociation and toxic

compounds' formation. For the investigated fuels, the amount of energy delivered from 1 kg of the fuel/air mixture was almost constant (ranging from 3.85 MJ/kg up to 4.04 MJ/kg).
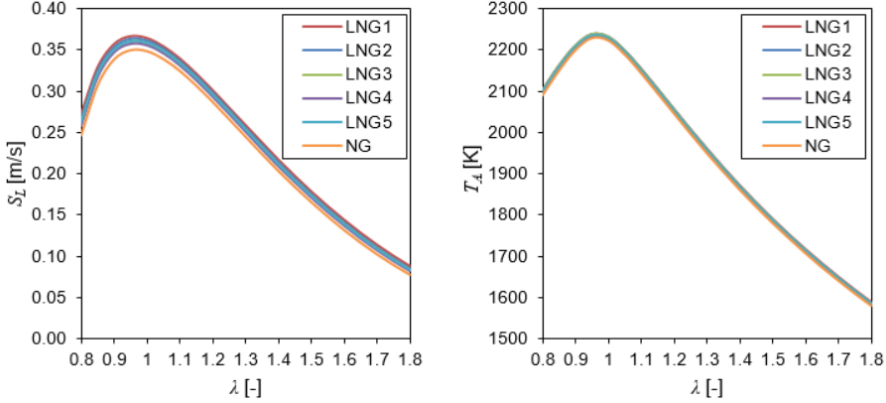


Figure 1: Laminar flame speed and adiabatic flame temperature *versus* air excess ratio.

In the case of laminar flame speed, the most significant change of $S_L$ value was observed in rich and stoichiometric conditions. The increase of HC share in the LNG fuels induced an increase of the $S_L$ value even by 10% for LNG1 (the highest content of ethane). It has been established that for combustible mixtures of a similar structure, the laminar flame speed is directly correlated with the adiabatic flame temperature. In the analyzed cases, where the calculated $T_A$ and mass burning rate are very similar for all investigated LNG fuels, there is a secondary effect which causes a deviation in the laminar flame speed. Since liquid natural gas is a mixture of simple alkanes (C1–C4), the $S_L$ deviation is caused mainly by the global consumption rate and density-compensated diffusivity [43].

The next analyzed parameters for the selected fuels (Table 3) are the ignition temperature and ignition delay time. For the estimation of $T_I$ and $t_d$, the procedure described in Section 2 was used. The calculated value of ignition temperature was at the same level in the range from 801 K to 806 K for the 10 s ignition induction time. The influence of LNG composition on the value of ignition delay time (Fig. 2) was observed.

For the whole investigated range of air excess ratio, the shorter ignition delay time was observed for LNG1 while the ignition process of NG was delayed by about 0.05 s. It was also noticed that the most significant impact on the value of ignition time has the amount of ethane in the fuel. This is

(a) $\lambda = 1.0$ and the constant volume reactor
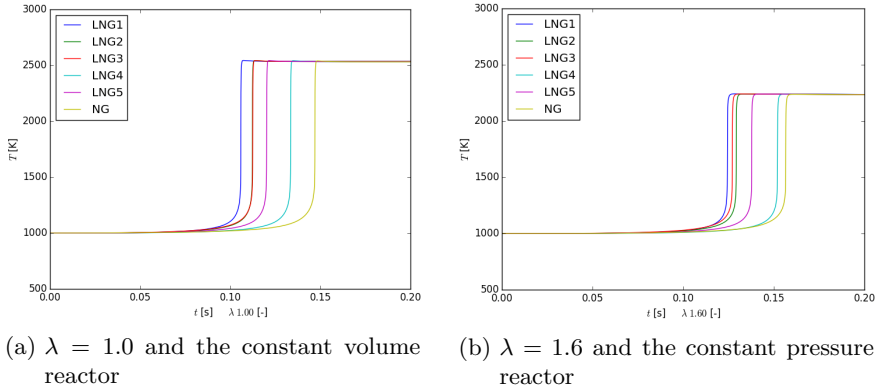
(b) $\lambda = 1.6$ and the constant pressure reactor

Figure 2: Ignition delay time for investigated fuels.

due to the character of the ethane oxidation process where a larger quantity of ethylene is produced and consequently more vinyl radicals are formed. They are more reactive than acryl radicals released from the combustion of longer chain alkenes (e.g., propane, butane). Moreover, slight differences in the maximum pressure value were observed for the combustion of provided mixtures in the constant volume.

To conclude, it can be said that for all studied LNG compositions, a significant influence on the combustion parameters such as $T_A$, $S_L$ and $T_i$ was not observed. It suggests that from this point of view, the LNG could be used interchangeably without loss of flame stability.

## 3.2 Emission characteristics

A second important parameter describing the combustion process is the emission of toxic compounds such as nitric oxides, carbon monoxide and unburned hydrocarbons. In this work, the emission analysis was divided into two parts. In the first, only the influence of fuel composition was taken into account. The results of nitric oxides and carbon monoxide emission are presented in Fig. 3.

Based on the results of numerical calculations of toxic compounds presented in this figure it can be noticed that the amount of air delivered to the combustion process has the most significant impact on the emission value. The impact of LNG composition (impact of the amount of high hydrocarbons) is most visible for rich and close to stoichiometric conditions. The nitric oxide emission rises by about 10% (25 ppm) for LNG1 and LNG5
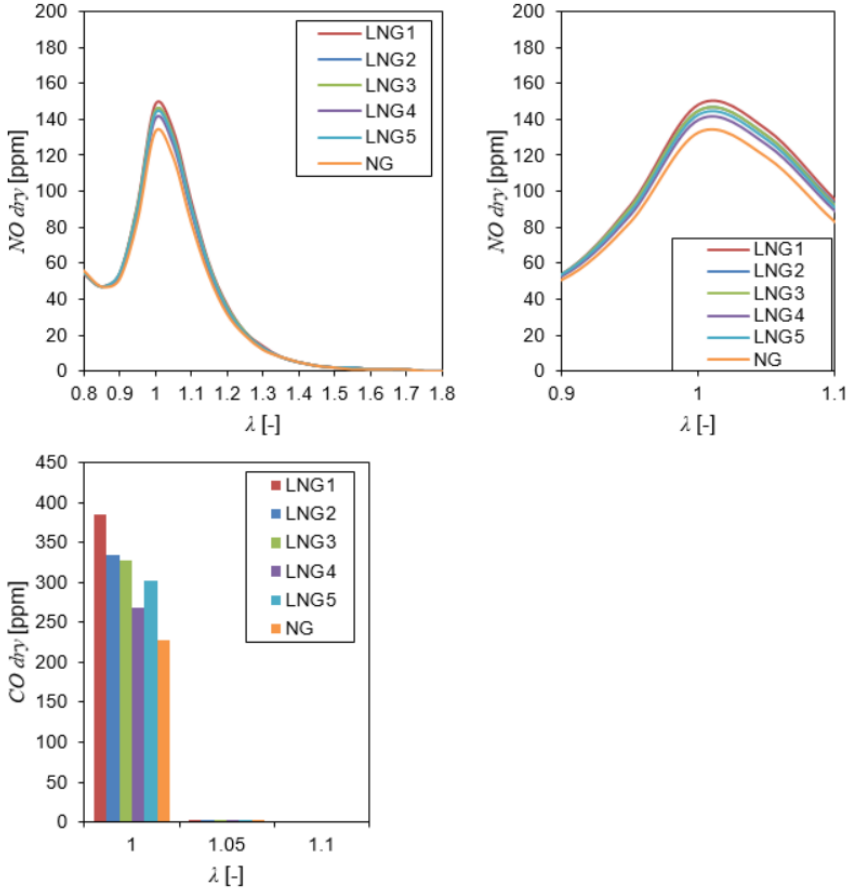
Figure 3: Emission characteristic of NO and CO; 1D FreeFlame with the radiative heat loss.

compared to NG. As it was presented before, $T_A$ is almost constant for all analyzed fuels. Therefore, it can be concluded that an increase of nitric oxide (NO) emissions is determined by a pathway other than thermal, probably by a prompt mechanism. The study on the combustion process of alkanes [44] has shown an increased amount of hydrogen cyanide (HCN) in the flame in the case of combustion of ethane, propane and butane in rich conditions. HCN originating from NCN (cyanonitrene) reactions is then the precursor of NO formation [45] according to the aforementioned prompt mechanism. The influence of LNG composition on carbon monoxide is negligible in the whole range of considered air excess ratios.

In the second case, constant amounts of air equal to 12.3, 12.9 and 13.5 $\mathrm{kg_{air}/Nm^3_{fuel}}$ corresponding to air excess ratio equal to 1.05, 1.1 and 1.15 (for NG combustion process) were taken as initial parameters of the combustion process. Conditions of the atmospheric pressure and constant temperature of substrate $T = 300$ K were used. This scenario simulates the real operating conditions of an energetic device for which the fuel type has been changed without any regulation. As it can be seen in Fig. 4, the fuel change from natural gas to LNG fuels resulted in a sharp increase of carbon monoxide emissions, which indicates an incomplete combustion process.
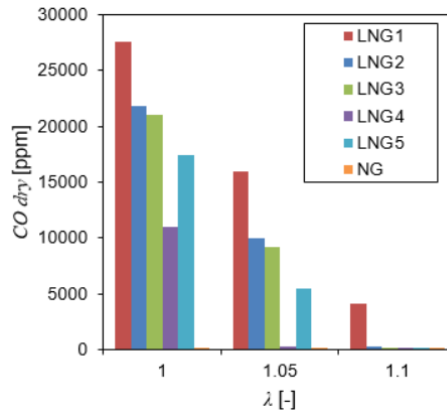


Figure 4: Carbon monoxide emission for a constant amount of air delivered to the combustion process; 1D BurnerFlame.

It can be noticed that even for the combustion process of NG taking place with the air excess ratio $\lambda = 1.1$ (2% of $O_2$ in dry flue gases), the introduction of LNG1 (instead NG) results in the emission of CO of about 4000 ppm. For the combustion processes with a lower air excess ratio, the molar fraction of carbon monoxide reached even a few per cent. Next to carbon monoxide, a significant amount of hydrogen (up to 1%) is observed. Such combustion processes cause a decrease of the combustion efficiency (up to 10%) [40] and can be dangerous for safety of the maintenance personnel.

## 4 Conclusions

The composition of LNG depends on the source location and varies mainly by different amounts of high hydrocarbons. As it was shown, the amount of high hydrocarbons in the fuel can reach even 10% of the molar fraction,

which has an influence main parameters of the combustion process and emission characteristics. The impact of LNG composition on parameters like the lower and upper flammability limits, adiabatic flame temperature, laminar flame speed or ignition temperature is negligible and does not influence the flame stability. The increased number of high hydrocarbons, especially the amount of ethane, can even improve the fuel ignition process and lead to a more stable combustion process. On the other side, an increase of hydrocarbons in LNG indicates a significant decrease of fuel resistance to knocking combustion processes, which disqualifies the utilization of raw LNG as a potential fuel for reciprocating gas engines. It was presented that replacing natural gas with LNG increased the nitric oxides emission even by a few percent.

The results showed that in the case of raw liquid natural gas introduced as a fuel to energy devices operating with a low air excess ratio, a significant increase in emission of carbon monoxide (even by a few per cent) and unburned hydrocarbons was noticed. It decreases the combustion efficiency and leads to the introduction of a large amount of toxic compounds into the environment.

Summarizing, it can be said that raw LNG can be used as interchangeable fuel to natural gas. However, in some industrial applications additional modifications are required, for example introduction of anti-knocking combustion systems, control of operating parameters or introduction of additional toxic compounds reduction systems.

# References

[1] Looi K.K., Baheta A.T., Habib K.: *Experimental performance and comfort analyses of photovoltaic thermoelectric system in a room air-conditioning application.* Heat Transf. Eng. **42**(2021), 1172–83. doi: 10.1080/01457632.2020.1777010

[2] Mosiężny J., Ziegler B., Czyżewski P.: *Numerical study of heat and mass flow in phes layered bed heat storage.* Int. J. Numer Methods Heat Fluid Flow. **30**(2020), 6, 3199–3209.

[3] Li H., Chen L., Wang D., Zhang H.: *Analysis of the price correlation between the international natural gas and coal.* Energy Procedia **142**(2017), 3141–6. doi: 10.1016/j.egypro.2017.12.376

[4] Mac Kinnon M.A., Brouwer J., Samuelsen S.: *The role of natural gas and its infrastructure in mitigating greenhouse gas emissions, improving regional air quality, and renewable resource integration.* Prog. Energy Combust. Sci. **64**(2018), 62–92. doi: 10.1016/j.pecs.2017.10.002

[5] *Natural gas trade via pipeline and LNG shipping worldwide from 2000 to 2019, with a forecast until 2050* https://www.statista.com/statistics/1165885/global-natural-gas-trade-by-flow-type/ (accessed March 16, 2020).

[6] Lisowski F„ Lisowski E.: *Design of internal supports for double-walled liquefied natural gas road tanker.* Heat Transf. Eng. **43**(2021), 238–47. doi: 10.1080/01457632.2021.1874653

[7] Akinsipe O., Anozie A., Babatunde D.: *A study of LNG processes to determine the effect of end flash systems on efficiency.* Arch. Thermodyn. **41**(2020), 2, 35–63. doi: 10.24425/ather.2020.132959

[8] Xu S., Chen X., Fan Z., Chen Y., Nie D., Wu Q.: *The influence of chemical composition of LNG on the supercritical heat transfer in an intermediate fluid vaporizer.* Cryogenics (Guildf) **91**(2018), 47–57. doi: 10.1016/j.cryogenics.2018.01.011

[9] Roy P.S., Ryu C., Park C.S.: *Predicting Wobbe index and methane number of a renewable natural gas by the measurement of simple physical properties.* Fuel **224**(2018), 121–7. doi: 10.1016/j.fuel.2018.03.074

[10] Liu C., Li F., Ma L.P., Cheng H.M.: *Advanced Materials for Energy Storage.* Adv. Mater. **22**(2010), 28–62. doi: 10.1002/adma.200903328

[11] Hernik B., Zabłocki W.: *Numerical research of combustion with a minimum boiler load.* Arch. Thermodyn. **41**(2020), 4, 93–114. doi: 10.24425/ather.2020.135855

[12] Joachimiak D., Frackowiak A.: *Experimental and numerical analysis of the gas flow in the axisymmetric radial clearance.* Energies **13**(2020), 21, 5794. doi: 10.3390/en13215794

[13] Kindra V.O., Milukov I.A., Shevchenko I.V., Shabalova S.I., Kovalev D.S.: *Thermodynamic analysis of cycle arrangements of the coal-fired thermal power plants with carbon capture.* Arch. Thermodyn. **42**(2021), 4, 103, 21. doi: 10.24425/ather.2021.139653

[14] Rogers D., Nelson R., Howell N.: *LNG in Europe: An Overview of European Import Terminals.* King & Spalding LLP, Georgia 2018.

[15] Wood D.A.: *A review and outlook for the global LNG trade.* J. Nat. Gas Sci. Eng. **9**(2012), 16–27. doi: 10.1016/j.jngse.2012.05.002

[16] Agentschap NL.: *Gas Composition Transition Agency Report 2013. The status of the transition to high-calorific-value gas.* Ministerie van Economische Zaken, 2013.

[17] EN 16726:2015 (E): *Gas infrastructure – Quality of gas – Group H – European Standard – Final Draft.* 2015.

[18] ISO 13686:2013(en) *Natural gas – Quality designation.* 2013.

[19] ISO 6326-3:1989 *Natural gas – Determination of sulfur compounds – Part 3: Determination of hydrogen sulfide, mercaptan sulfur and carbonyl sulfide sulfur by potentiometry.* 1980.

[20] ISO 6978-1:2003 *Natural gas – Determination of mercury – Part 1: Sampling of mercury by chemisorption on iodine.* 2003.

[21] ISO 6978-2:2003 *Natural gas – Determination of mercury – Part 2: Sampling of mercury by amalgamation on gold/platinum alloy.* 2003.

[22] ISO 6327:1981 *Gas analysis – Determination of the water dew point of natural gas – Cooled surface condensation hygrometers.* 1981.

[23] ISO 6976:2016 *Natural gas – Calculation of calorific values, density, relative density and Wobbe indices from composition.* 2016.

[24] ISO 13443:1996 *Natural gas – Standard reference conditions.* 1996.

[25] Leiker M., Christoph K., Rankl M., Cartellieri W., Pfeifer U.: *The evaluation of the antiknocking property of gaseous fuels by means of the methane number and its practical application to gas engines.* In: Proc. 9th Int. Cong. on Combustion Engines, Stockholm 1971.

[26] Kubesh J., King S., Liss W.: *Effect of gas composition on octane number of natural gas fuels.* SAE Tech. Pap. 922359, 1992. doi: 10.4271/922359

[27] ISO 15403-1:2006 *Natural gas – Natural gas for use as a compressed fuel for vehicles – Part 1: Designation of the quality.* 2006.

[28] Kayadelen H.K.: *A multi-featured model for estimation of thermodynamic properties, adiabatic flame temperature and equilibrium combustion products of fuels, fuel blends, surrogates and fuel additives.* Energy **143**(2018), 241–56. doi: 10.1016/j.energy. 2017.10.106

[29] Wei W., Yu Z., Zhou T., Ye T.: *A numerical study of laminar flame speed of stratified syngas/air flames.* Int. J. Hydrogen Energy. **43**(2018), 9036–45. doi: 10.1016/j.ijhydene.2018.03.167

[30] Fieweger K., Blumenthal R., Adomeit G.: *Shock-tube investigations on the self-ignition of hydrocarbon-air mixtures at high pressures.* Symp. Combust. **25**(1994), 1579–1585. doi: 10.1016/S0082-0784(06)80803-9

[31] Goodwin D., Moffat H., Speth R.: *Cantera: An Object-Oriented Software Toolkit For Chemical Kinetics, Thermodynamics, And Transport Processes. Version 2.3.0.* 2017. doi: 10.5281/zenodo.170284

[32] Sher E., Levinzon D.: *Scaling-down of miniature internal combustion engines: Limitations and challenges.* Heat. Transf. Eng. **26**(2005), 1–4. doi: 10.1080/01457630 591004780

[33] Hermanns R.T.E., Konnov A.A., Bastiaans R.J.M., De Goey L.P.H., Lucka K., Köhne H.: *Effects of temperature and composition on the laminar burning velocity of CH4+H2+O2+N2 flames.* Fuel **89**(2010), 114–21. doi: 10.1016/j.fuel.2009.08.010

[34] Goodwin D.G, Moffat H.K., Schoegl I., Speth R.L, Weber B.W.: *Cantera: An object-oriented software toolkit for chemical kinetics, thermodynamics, and transport processes. Version 2.6.0.* 2022. doi: 10.5281/zenodo.6387882

[35] *Chemical-Kinetic Mechanisms for Combustion Applications.* Univ. Calif., San Diego 2022.

[36] Slefarski R.: *Study on the combustion process of premixed methane flames with CO2 dilution at elevated pressures.* Energies **12**(2019), 3. doi: 10.3390/en12030348

[37] Smith G.P., Golden D.M., Frenklach M., Moriarty N.W., Eiteneer B., Goldenberg M., Bowman C.T., Hanson R.K., Song S., Gardiner W.C., Lissianski J.V.V., Zhivey Q.: *GRI-Mech 3.0.* 2020 http://combustion.berkeley.edu/gri-mech/ (accessed March 10, 2021).

[38] https://www.euromot.eu/publication-and-events/publications/ (accessed Jan. 16, 2019).

[39] Barczyński A., Łaciak M.: *Interchangeability of gaseous fuels (natural gas)*. Wiadomości Naft. Gazow. **8**(2014), 196 (in Polish).

[40] Odgers J., Kretschmer D.: *Gas turbine fuels and their influence on combustion*. Abacus Press, Swinburne 1986.

[41] Mozgovoy A., Burmeister F., Albus R.: *Contribution of LNG use for the low calorific natural gas network's safe and sustainable operation*. Energy Procedia **64**(2015), 83–90. doi: 10.1016/j.egypro.2015.01.011

[42] https://www.cumminswestport.com/models/isx12-g (accessed Oct. 16, 2018).

[43] Davis S.G., Law C.K.: *Determination of fuel structure effects on laminar flame speeds of $C_1$ to $C_8$ hydrocarbons*. Combust. Sci. Technol. **140**(1998), 1–6, 427–449. doi: 10.1080/00102209808915781

[44] Sutton J.A., Williams B.A., Fleming J.W.: *Investigation of NCN and prompt-NO formation in low-pressure C1-C4 alkane flames*. Combust. Flame **159**(2012), 2, 562–76. doi: 10.1016/j.combustflame.2011.08.023

[45] Lamoureux N., Desgroux P., Bakali A., Pauwels J.F.: *Experimental and numerical study of the role of NCN in prompt-NO formation in low-pressure CH4–O2–N2 and C2H2–O2–N2 flames*. Combust. Flame **157**(2010), 1929–1941. doi: 10.1016/j.combust flame.2010.03.013

# Thermodynamics-based measurement of the velocity of high-temperature smoke

**HAOYU WANG**[*]

Department of Fire Engineering, China Fire and Rescue Institute, Nanyan 4, Changping District, 102202, Beijing; China

**Abstract**   In view of the high cost and difficulty of ensuring the accuracy in the measurement of fire smoke velocity, the measurement system developed using platinum resistance temperature detectors and an 8-bit microcontroller, is used to realize the fast measurement of high-temperature fire smoke velocity. The system is based on the thermodynamic method and adopts the Kalman filter algorithm to process the measurement data, so as to eliminate noise and interference, and reduce measurement error. The experimental results show that the Kalman filter algorithm can effectively improve the measurement accuracy of fire smoke velocity. It is also shown that the system has high measurement accuracy, short reaction time, low cost, and is characterized by high performance in the measurement of high-temperature smoke velocity in experiments and practice.

**Keywords:** Thermodynamics; Smoke; Flow velocity; Measurement; Kalman filter algorithm

## Nomenclature

| | | |
|---|---|---|
| $\eta$ | – | Einstein coefficient |
| $C_p$ | – | specific heat capacity, J/kgK |
| $l$ | – | distance between two temperature detectors, m |
| $q$ | – | heat flux density, J/m$^2$ |

---

[*]Corresponding Author. Email: taofuyanukc119@163.com

$r$ – radius of the tube, m
$x$ – state variable
$v$ – flow rate of the measured gas, m/s
$\rho$ – density, kg/m$^3$

**Greek symbols**

$\eta$ – Einstein coefficient

# 1 Introduction

The smoke spreading in fire buildings poses a fatal threat to indoor personnel. The research on smoke flow and control in buildings has attracted extensive attention [1]. The smoke velocity as an important parameter of smoke movement is commonly referred to in related studies and is worth measuring. However, it is difficult to obtain the velocity of high-temperature smoke due to the smoke heat and the blockage and erosion caused by numerous carbon black particles and droplets [2]. Two types of smoke velocity measurement are mainly adopted, one is based on the pressure difference with a pitot tube, and the other is based on a leveraged hot-wire device [3]. The Pitot tube, is conducive to measuring high flow rates, and the error will be greater at low flow rates [4]; the accuracy of the hot-wire device is high, but the probe is prone to be blocked and damaged by the carbon black particles in the smoke. The probe price is high, and the damage of the probe will greatly increase the experimental cost. Hence, finding a low-cost, applicable and reliable measurement method is necessary. Zhou *et al.* [5] proposed an approach to measure the smoke velocity by using the temperature pulse information of smoke. This method used the polarity correlation technology to process temperature data with a short response time and high accuracy, but the measurement was limited by the distance from the fire source and the severity of combustion. The error was even larger when the fire source was far away or the combustion remained relatively stable. Shen *et al.* [6] utilized thermodynamics to measure the coal flow rate in coal-fired boiler pneumatic conveying. However, the measurement of smoke velocity by the thermodynamic method has a large error. To improve the accuracy, the data filtering technology can be used to eliminate the noise and interference in measurement, so as to restore the real data and improve the measurement accuracy.

The principles of the thermodynamic method and Kalman filter algorithm are introduced first; then the structure of the thermodynamics-based velocity measurement system is presented, and the measurement results with the hot wire equipment are compared. Finally, the conclusions are given.

## 2    The measurement principle of thermodynamics

The measurement principle is demonstrated in Fig. 1. The smoke flows from the combustion chamber into the velocity measuring tube, the middle of which is heated by a fixed heat source. The measurement system is composed of two probes, a signal converter and a microcontroller. The velocity probes are made of platinum resistance temperature detectors, one of which measures the smoke temperature as $T_1$, the other is heated to a temperature higher than the smoke as $T_2$.
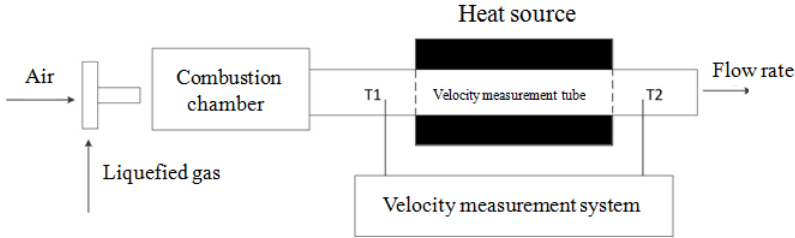


Figure 1: Measuring principle of smoke velocity based on thermodynamics.

According to the principle of heat transfer and energy conservation

$$C_p \rho v \pi r^2 \left(T_2 - T_1\right) = q 2\pi r l, \tag{1}$$

where $C_p$ is the specific heat capacity of the smoke, $\rho$ is the smoke density, $\nu$ is the flow rate of the measured gas, $r$ is the radius of the tube, $q$ is the heat flux density of the heat source, and $l$ is the distance between two platinum resistances temperature detectors.

From Eq. (1), we have

$$\Delta T = T_2 - T_1 = \frac{2ql}{C_p r} \frac{1}{\rho v}. \tag{2}$$

Since the smoke density varies little in the actual measurement environment, the flow rate of the measured smoke can be calculated through the measurement of the temperature difference ($\Delta T$) from above relationship [7].

# 3  The mechanism of the Kalman filter

The Kalman filter is an algorithm that uses the state equation of a linear system to optimally estimate the system through the input and output observation data [8]. To make the measurement result closer to the real data, the Kalman filter algorithm introduces the state variable formula and adds the changing noise to the formula to compensate for the unpredictable error. The state variable in the Kalman filter algorithm can be expressed as follows:

$$x_k = \mathbf{A}x_{k-1} + \mathbf{B}u_{k-1} + w_{k-1}\,, \tag{3}$$

where $x$ is the filtered state variable; $\mathbf{A}$ is the state matrix; $u$ is the control variable; $\mathbf{B}$ is the control matrix; $w$ is the process noise, and $k$ represents the $k$th process.

The measurement results calculated by the thermodynamic method can be expressed as follows:

$$z_k = \mathbf{H}x_k + y_k\,, \tag{4}$$

where $z$ is the result of thermodynamic measurement; $\mathbf{H}$ is the gain matrix, $x$ is the variable of state, and $y$ is the measurement noise. Due to the error of $z$, it cannot be directly used as a measurement result, and it needs to be converted into a state variable through the gain matrix $\mathbf{H}$.

The distribution of the process noise $w$ and the measurement noise $v$ in the algorithm can be expressed by relations:

$$p(w) \sim N(0, Q), \tag{5}$$

$$p(v) \sim N(0, R), \tag{6}$$

where $p$ and $N$, representing the process noise and observation noise, are independent, and follow normal distribution from 0 to $Q$ and 0 to $R$, respectively In a real system, the process noise covariance matrix $\mathbf{Q}$ and the observation noise covariance matrix $\mathbf{R}$ change with each iteration [9].

The filtering process of the Kalman filter algorithm is shown in Fig. 2 [10].
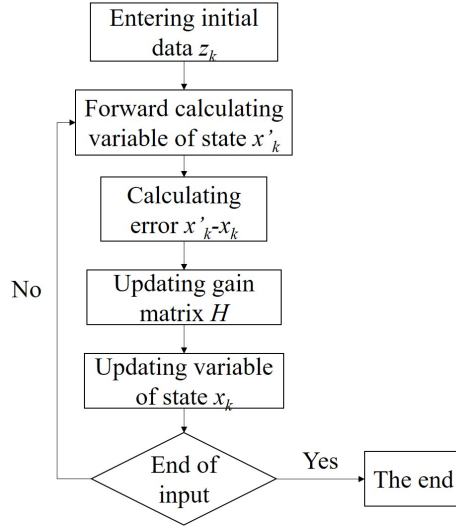
Figure 2: Flow chart of the Kalman filter algorithm.

# 4   The velocity component measurement system

The hardware of the velocity measurement system mainly includes two platinum resistance temperature detectors Pt100, a data acquisition module, a velocity display screen and an 8-bit microcontroller (MCU) 8051, as shown in Fig. 3. The temperature measurement range of the Pt100 resistance tem-
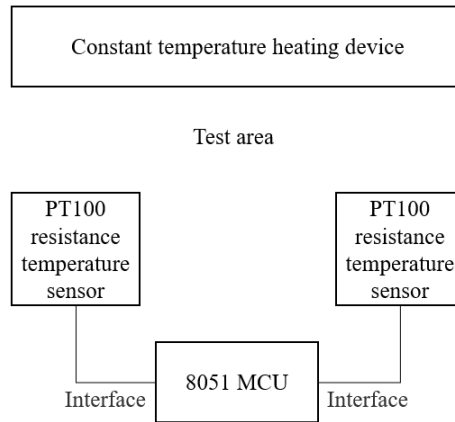


Figure 3: Structure of the velocity measurement system.

perature sensor is 0–550°, which meets the experimental requirements. The
sensor also has the advantages of anti-vibration, corrosion resistance, opti-
mal stability and high accuracy. In addition, compared with the probe of
the hot wire device, the probe of the sensor is a closed structure, which will
not be blocked by smoke particles and is easy to clean. 8051 MCU is widely
used in data acquisition and processing.

The system software is written in 8051 MCU C language and consists
of two modules: real-time data acquisition and velocity calculation display.
The Kalman filter algorithm is adopted for data processing. The data ac-
quisition frequency is 1000 Hz; the measurement range is 0–20 m/s; the
accuracy is 0.1 m/s, and the error is ±10%. The data acquisition time of
the system is 2 s; the calculation time is 3 s, and the total response time
is less than 5 s, which is in accordance with the response time required in
experiments and actual measurements.

## 5  Experimental results and analysis

The smoke velocity measurement experiments were carried out in a 1/3
scale simulated high-rise building, as shown in Figs. 4–6. The experimental
house has 10 storeys, each with a storey height of 1m. The mixture of lique-
fied petroleum gas (LPG) and the air was burned in the experimental room,
producing high-temperature smoke. Then the smoke entered the corridor
through the open door. The flow rate and temperature of the smoke were
adjusted by changing the flow rate of liquefied gas and air. Considering the
size of the fire source and the smoke velocity, the horizontal corridor directly
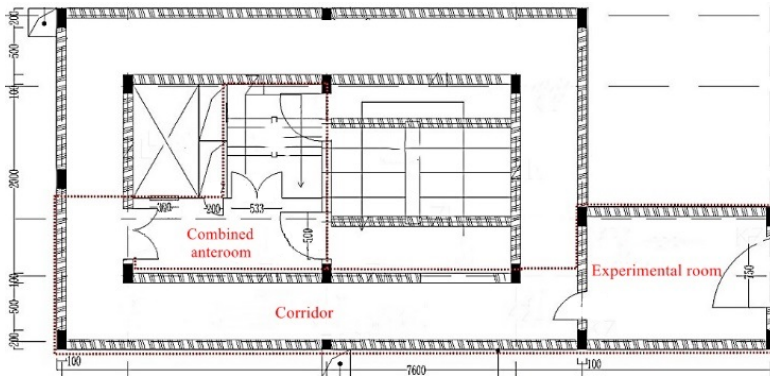


Figure 4: 1/3 scale fire experiment house plan.

connected with the experimental room on the third floor was selected as the velocity measurement section of the experiment. The schematic diagram of the chosen 'room-corridor' section is illustrated in Fig. 7.



Figure 5: The northern side of the experimental house.



Figure 6: The southern side of the experimental house.

To verify the accuracy of the measurement results, a handheld high-temperature anemometer (model 6162) manufactured by Kanomax,was selected for simultaneous measurement at the same measuring point. Then the results of the measurement system and the anemometer are compared. The anemometer includes a host and a probe, which is suitable for two types of probes, the medium-temperature model 0203 and the high-temperature
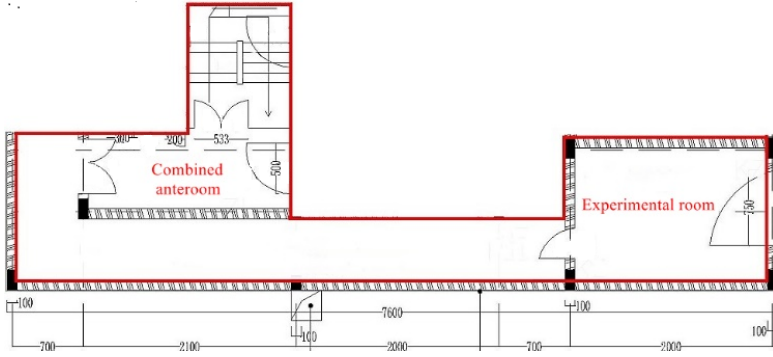
Figure 7: The 'room-corridor' plan of the experiment.

model 0204. The experiment used the high-temperature model 0204 probe, and the host response time was less than 4 s.

Before the experiment, the equipment was calibrated under normal temperature and 0.5 m/s wind speed, and the results are shown in Fig. 8. It shows that the measurement results are basically consistent at room temperature and constant wind speed.
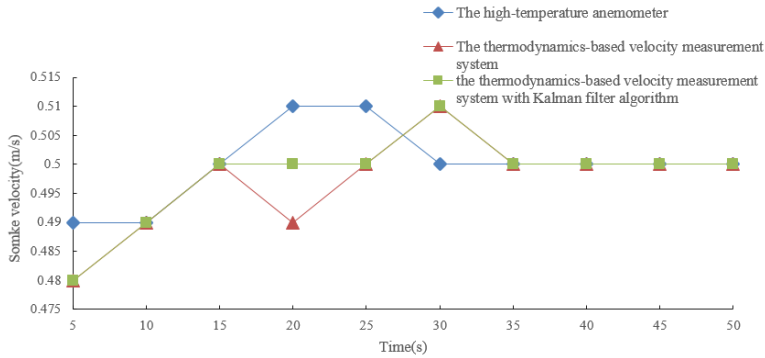


Figure 8: Results of the calibration test.

Two comparative experiments were conducted in total. The measuring point of the first experiment was located at a horizontal distance of 3.2 m from the corridor to the experimental room (the room of fire origin), and a vertical distance from the corridor floor of 0.85 m.The measuring point of the second experiment was located at a horizontal distance of 4.2 m from the corridor to the experimental room, and a vertical distance from the corridor floor of 0.85 m. According to the similarity criterion of the physical

model, the scale of the distance and height of the 1/3 scale simulated high-rise building experiment house to the actual size is 1 to 3. To this end, the actual location of the measuring points is 9.6 m and 12.6 m of horizontal distance from the room, and the vertical height is 0.45 m under the ceiling. The smoke velocity is relatively stable and is convenient for measurement. The data collection cycle is 5 s. The results of the first experiment are shown in Figs. 9 and 10.



Figure 9: Results of the first experiment.



Figure 10: Error analysis of the first experiment.

Figure 9 illustrates the comparison of the measurement results from the two methods, and Fig. 10 displays the error diagram of the thermodynamics-based velocity measurement system with the Kanomax model 6162 hand-held anemometer as the standard. The upper end of the error line is the

direct measurement result based on the thermodynamic method, and the lower end is the measurement result of the software system obtained with the Kalman filter algorit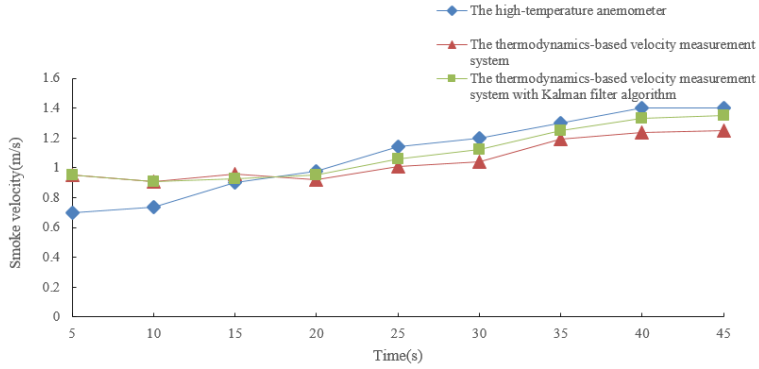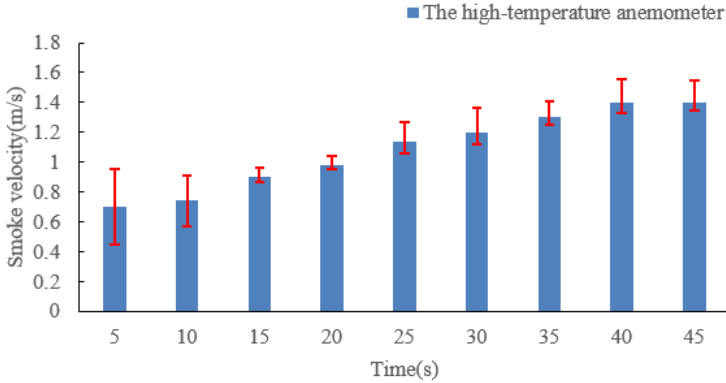hm. It can be seen that the measurement results of the smoke velocity of the Kalman filter algorithm at the same location are closer to those of the handheld high-temperature anemometer. At the beginning of the experiment, the deviation between the two measurement systems is relatively large, but the results tend to be consistent after 15 s. This is because the Kalman filter algorithm needs to receive initial data for iterative calculations to eliminate noise and interference at the beginning of the measurement. After that, the change of the gain matrix tends to be stable, and the measurement accuracy is significantly improved. Compared with the handheld anemometer, the average deviation of the measurement results of the thermodynamic method is 9.9%, and that processed by the Kalman filter algorithm is 6.6%, improved by 33.3%.

The measurement results of the second experiment are shown in Figs. 11 and 12. Figure 11 shows the comparison of the measurement results of the two methods. Figure 12 shows the error diagram of the thermodynamics-based velocity measurement system based on the Kanomax model 6162 handheld anemometer. The upper end of the error line is the direct measurement results based on the thermodynamic method, and the lower end is the measurement results of the software system with the Kalman filter algorithm. As shown in Figs. 11 and 12, the measurement results of smoke velocity with the Kalmanfilter algorithm at the same location are closer to those of the handheld high-temperature anemometer. At the beginning of the experiment, the deviation between the two measurement systems is
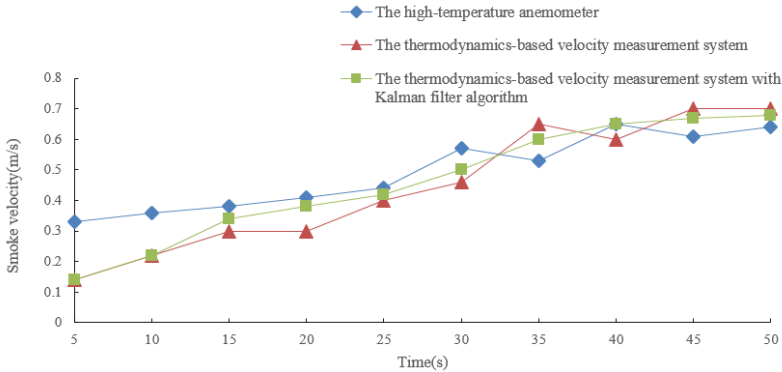


Figure 11: Results of the second experiment.
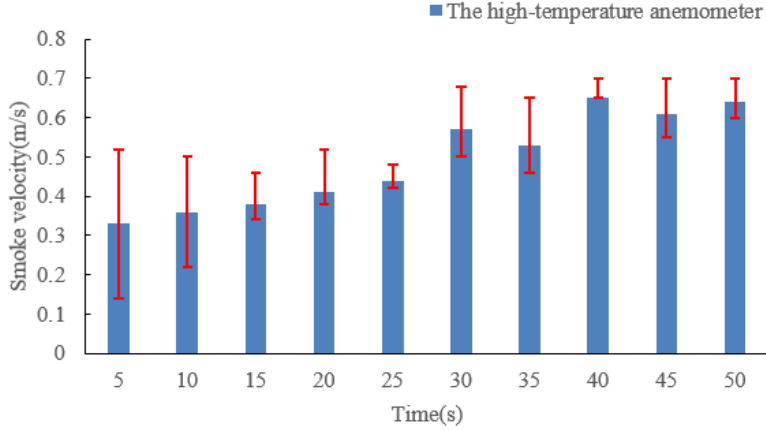
Figure 12: Error analysis of the second experiment.

relatively large, and the results tend to be consistent after 15 s. Compared with the handheld anemometer, the average deviation of the measurement results based on the thermodynamic method is 13.89%, and that based on the Kalman filter algorithm is 9%, improved by 35.2%.

In the initial stage of the experiment, the temperature in the corridor was low; the Pt100 resistance value was large, and the signal value generated in the circuit was too small, resulting in large errors [11, 12]. As the experiments progressed, the temperature in the corridor gradually increased; the platinum resistance value decreased, and the signal value in the circuit increased. The accuracy of the system was improved. Since the Kalman filter algorithm needs initial data for iterative calculation in the initial stage, it cannot effectively eliminate the error in this stage.

Due to the differentials in the algorithms and types of probes in the two experiments, as well as the diversity of smoke particles and the complexity of motions, the deviation between the thermodynamics-based measurement results and the high-temperature anemometer measurement results is still within the acceptable range in the actual gauge. Although the measurement accuracy in the low temperature area is not satisfying, the thermodynamics-based smoke velocity measurement system has relatively high accuracy from the overall perspective.

In addition, the experiments show that the data sampling frequency will affect the measurement accuracy [13]. The measurement accuracy can be optimized by increasing the sampling frequency, and the sampling fre-

quency cannot be increased indefinitely due to the limitation of hardware conditions [14]. When the sampling frequency is 1000 Hz, the measurement accuracy can meet the measurement requirements under general experimental conditions. The experiments show that the data acquisition time will also affect the measurement accuracy. The longer is the data acquisition time, the higher is the measurement accuracy. Due to the limitations of hardware conditions and response time requirements, the data acquisition time cannot be too long [15]. When the data acquisition time is 2 s, higher measurement accuracy can be available, and the response time of the system is also within an acceptable range.

## 6    Conclusions

The velocity of high-temperature smoke was measured by the thermodynamic method, and the results demonstrate that the system has high accuracy and measurement precision. The results show that:

1. The Kalman filtering algorithm effectively improves the accuracy of measuring smoke velocity by the thermodynamic method.

2. Compared with the handheld high-temperature anemometer, the accuracy of the thermodynamic smoke velocity measurement system based on the Kalman filter algorithm can meet the requirements of experimental measurement, and the system has lower cost and higher equipment reliability.

3. At the beginning of the experiment, the results of the measurement system based on the thermodynamic method have a larger deviation than that of the handheld high-temperature anemometer. Due to the characteristics of the algorithm, the Kalman filter algorithm has no obvious effect at this stage. This error needs to be further corrected by a neural network model with more test data.

4. When the data sampling frequency is 1000 Hz and the acquisition time is 2 s, the accuracy of the smoke velocity measurement system reaches 0.1 m/s.

It is worth noting that the error of the system at low temperatures is larger than that at high temperatures. Although the response time can

meet most experimental requirements, there is still room for further improvement. These problems needs to be further solved in the follow-up study.

# References

[1] Trawiński P.: *Development of real gas model operating in gas turbine system in Python programming environment.* Arch. Thermodyn. **41**(2020), 4, 23–61. doi: 10.24425/ather.2020.135853

[2] Shibata K., Shimizu M., Inaba S.I., Takahashi R., Yagi J.I.: *One-dimensional flow characteristics of gas-powder two phase flow in packed beds.* Tetsu-to-Hagane **77**(1991), 2, 236–243 (in Japanese). doi: 10.2355/tetsutohagane 1955.77.2_236

[3] Pan L.W.: *On the characteristics of smoke stratified transportation with smoke control in tunnel.* Univ. Sci. Technol. China, Hefei 2011 (in Chinese).

[4] Nguyen D.T., Choi Y.M., Lee S.H., Kang W.: *Experimental investigation on the optimum geometry of an s-type pitot tube for GHG emission monitoring.* J. Phys. Conf. Ser. **1065**(2018), 9, 092009. doi: 10.1088/1742-6596/1065/9/092009

[5] Zhou J., Yuan Z.F., Pu X.G., Wang K., Lu Y.G., Cen K.F.: *Study of zero-crossing polarity correlation for velocity measurement of high temperature flue gas.* Proc. CSEE **19**(1999), 3, 12–14. doi: 10.3321/j.issn:0258-8013.1999.03.003

[6] Shen A., Sun Z.K., Zhou L., Hu B., Yuan Z.L., Yang L.J.: *Experimental study on coupling of turbulent and chemical agglomeration to promote coal particles removal by electrostatic precipitator.* Proc. CSEE **39**(2019), 10, 2954–2962. doi: 10.13334/j.0258-8013.pcsee.180842

[7] Joachimiak M., Joachimiak D., Krzyślak P.: *Analysis of heat flow in a tube bank of a condenser considering the influence of air.* Arch. Thermodyn. **38**(2017), 3, 119–134. doi: 10.1515/aoter-2017-0019

[8] Xue C., Huang Y., Zhu F., Zhang Y., Chambers J.A.: *An outlier-robust Kalman filter with adaptive selection of elliptically contoured distributions.* IEEE T. Signal Process. **70**(2022), 994–1009. doi: 10.1109/TSP.2022.3151199

[9] Cai W., Nasser B.B., Djemai M., Laleg-Kirati T.M.: *Kalman filter design for intermittent optical wireless communication systems on time scales.* arXiv prep. arXiv:2203.16166[eess.SY], (2022). doi: 10.48550/arXiv.2203.16166

[10] Gonzalez-Cagigal M.A., Rosendo-Macias J.A., Gomez-Exposito A.: *Parameter estimation of fully regulated synchronous generators using unscented Kalman filters.* Electr. Pow. Syst. Res. **168**(2019), 210–217. doi: 10.1016/j.epsr.2018.11.018

[11] Treichel Z., Dabrowski D., Peryt M., Roslon K.: *Verification of operation Pt100 platinum resistance thermometer to measure the electronic elements inside time-of-flight (TOF) detector.* Acta Phys. Pol. B Proc. Suppl. **11**(2018), 4, 759–764. doi: 10.5506/APHYSPOLBSUPP.11.759

[12] Ruan C.Z.: *A design of temperature measurement system based on Pt100 resistance.* J. Wuyi Univ. **33**(2014), 2, 62–65. doi: 10.14155/j.cnki.35-1293/g4.2014.02.013

[13] Zhang H., Guo C.S., Chen Y.: *Inverse material characterization through finite element simulation of material tests and numerical optimization.* Procedia Manuf. **34**(2019), 455–462. doi: 10.1016/j.promfg.2019.06.198

[14] Wang H.Q., Wang Y.H., Ren S.T., Meng Q.T., Wang Y.L.: *Research on frequency response characteristics of ring type electrostatic sensor for gas-solid two-phase flow detection.* Laser Optoelectron. Prog. **57**(2020), 17, 149–154. doi: 10.3788/LOP57.171202

[15] Hu H.L., Tang K.H., Tang C.H., Wang X.X.: *Fundamentals of electrical capacitance sensing and its applications for two-phase flow parameter detection.* J. Northwest Univ. (Nat. Sci. Edn.) **49**(2019), 681–690. doi: 10.16152/j.cnki.xdxbzr.2019-05-002

# Influence of the primary components of the high-speed train on fire heat release rate

**YUANLONG ZHOU**[a*]
**HAIQUAN BI**[b]
**HONGLIN WANG**[b]

[a] University of Science and Technology of China, State Key Laboratory of Fire Science, Hefei, Anhui 230026, China

[b] Southwest Jiaotong University, School of Mechanical Engineering, Chengdu 610031, China

**Abstract** A numerical model of the high-speed train carriage fire is established in this study. The influence of ceilings, sidewalls, luggage racks, seats, and floors on the heat release rate (HRR) of the high-speed train is studied by numerical methods. The results indicate that the heat release rate per unit area (HRRPUA) of ceiling and seat material dramatically influences the peak HRR and the time to peak HRR of train carriage fire. When the peak HRRPUA of interior ceiling material 1 decreases from 326 to 110 kW/m$^2$, the peak HRR of the high-speed train fire decreases from 36.4 to 16.5 MW, with a reduction ratio of 54.7%. When seat materials with low HRRPUA are used, the peak HRR reduction ratio is 44.8%. The HRRPUA of the sidewall, luggage rack, and floor materials has little effect on the peak HRR of the carriage fire. However, the non-combustible luggage rack can delay the time when the HRR reaches its peak.

**Keywords:** High-speed train; Carriage fire; Primary components; Heat release rate; Numerical methods

## Nomenclature

| | | |
|---|---|---|
| $C_s$ | – | Smagorinsky constant |
| $D_i$ | – | component mass diffusion coefficient, m$^2$/s |
| $f$ | – | force (except gravity), N |

*Corresponding Author. Email: zylong505@163.com

| $g$ | – | gravitational acceleration, m/s$^2$ |
| $h_s$ | – | sensible enthalpy, J/kg |
| $k$ | – | coefficient of heat conductivity, W/(m K) |
| $\dot{m}_i'''$ | – | mass formation rate of the $i$th component in unit volume, kg/(m$^3$ s) |
| $Q$ | – | heat release rate of the fire, kW |
| $\mathbf{q_r}$ | – | radiant heat flux vector |
| $P$ | – | pressure, Pa |
| $R_g$ | – | specific gas constant, J/(kg K) |
| $S_{ij}$ | – | strain tensor |
| $T$ | – | thermodynamic temperature, K |
| $t$ | – | time, s |
| $U$ | – | velocity of airflow, m/s |
| $u$ | – | velocity vector |
| $u_i,\ u_j$ | – | velocity components, m/s |
| $x$ | – | distance along the train carriage centre line |
| $x_i,\ x_j$ | – | Cartesian coordinates |
| $Y_i$ | – | volume fraction of the $i$th component |

**Greek symbols**

| $\mu$ | – | kinematic viscosity, m$^2$/s |
| $\mu_{\mathrm{LES}}$ | – | turbulent viscosity coefficient |
| $\rho$ | – | density, kg/m$^3$ |
| $\tau_{ij}$ | – | residual stress tensor |

**Acronyms**

| HRR | – | heat release rate |
| HRRPUA | – | heat release rate per unit area |
| LES | – | large eddy simulation |

# 1   Introduction

The high-speed train has been favoured by the rail transportation industry worldwide. In the past decade, China's high-speed railway has developed rapidly. By the end of 2022, the mileage of the high-speed railway in China has exceeded 42 000 km. High-speed railways and trains have become an essential part of modern transportation and essential infrastructure for economic development [1].

The flame and smoke will spread rapidly in the high-speed train carriage when a fire occurs. The safe evacuation of personnel is challenging, often causing heavy casualties and property losses [2]. The heat release rate (HRR) is the primary variable in high-speed train fire safety design and fire hazard evaluation. How to accurately calculate the HRR of high-speed train fire and analyze its influencing factors has become the focus of high-speed train fire research [2]. However, the existing calculation methods for the

fire HRR, such as the average heat release rate method [3] and Duggan method [4], can not reflect the influence of primary train components on the fire HRR, which makes the HRR calculated by the average heat release rate method and Duggan method much higher than the actual value.

The high-speed train fire is a complex combustion process. Its fire development process and HRR are mainly affected by the combustion characteristics of train materials, structures, and environmental factors [5]. The National Institute of Standards and Technology has conducted many combustion tests to analyze materials' flammability and smoke production characteristics [6]. They measured the HRR of seats by cone calorimeter [7] and studied the influence of seat combustion characteristics on fire spread. By comparing the small-scale test with the full-scale test, they found that the combustion characteristics of small-scale material can reflect the combustion characteristics of full-scale material in the actual combustion, consistent with the European Railway Research Institute [8].

With the extensive application of new composite materials in manufacturing train structures, the research on combustion tests of train material has not stopped. Kim *et al.* [9] used a small-scale material combustion test to study the fire-proof performance of train composite material. Lee *et al.* [10] conducted a combustion test to analyze the fire performance of train materials. Duggan [4] used a cone calorimeter to carry out many combustion tests of train materials. The research results showed that different radiation intensities should be used for different structure surfaces in the material combustion test. For example, the radiation intensity received by the ceiling, sidewall, and floor material surface should be 50, 35, and 25 kW/m$^2$, respectively. This study provides a reference for selecting radiation intensity in the high-speed train material combustion test.

From 2000 to 2003, the Commonwealth Scientific and Industrial Research Organisation (CSIRO) conducted a series of full-scale train fire experiments. The results showed that the fire spread characteristics in the carriage are related to the layout of the train carriage [2]. The number of combustibles and the relative position of combustibles has a significant impact on the fire spread characteristics, which are the primary factors in controlling the flame spread [11]. Although scholars have researched the combustion characteristics of train materials and fire spread characteristics, there is little research on the combustion characteristics of train structures.

Taking a high-speed train in China as the research object, this paper studies the influence of the primary components of high-speed trains on the fire HRR through numerical methods. The study results can provide a reference for establishing a calculation method for high-speed train fire HRR.

# 2 Material and component combustion experiments

The heat release rate per unit area (HRRPUA) and the ignition temperature of materials are the main parameters of the high-speed train fire numerical simulation, which can be obtained by cone calorimeter [7] and ignition temperature tester [2] experiments, respectively. This section describes the high-speed train carriage's material and component combustion experiments in detail.

## 2.1 Material of train carriage

The structure of a high-speed train carriage is complex, and there are many interior decoration materials. The sidewalls, ceilings, luggage racks, seats, floors, and cables account for a large proportion and impact the fire spread characteristics in the carriage, which is the primary component of the high-speed train. Figure 1 shows the schematic diagram of the high-speed train carriage structure. The length is 24.2 m, the width is 3.4 m, and the height is 2.9 m.



(a) Train carriage sectional view



(b) Train carriage plan view
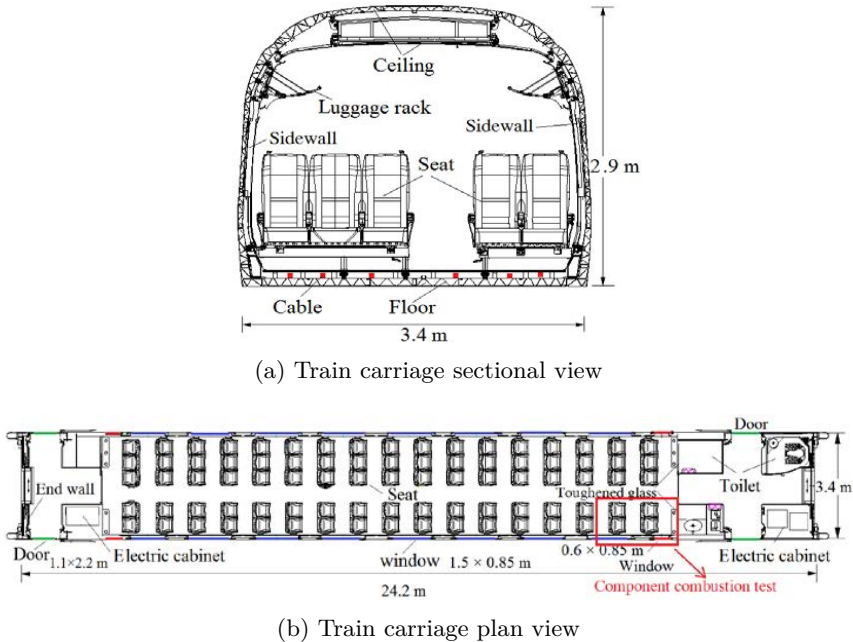
Figure 1: Schematics of the train structure.

The surface areas and thickness of the main combustible structures in the high-speed train carriage are given in Table 1. Figure 2 shows the proportion of the surface area of the main structure of the carriage.

Table 1: The surface area of each combustible structure of a train carriage.

| Structure | Composition | Surface area (m$^2$) | Thickness (mm) | Radiation intensity (kW/m$^2$) |
|---|---|---|---|---|
| Ceiling | Cold-resistant material | 127.9 | 20 | 50 |
| | Interior ceiling material 1 | 63.8 | 50 | |
| | Interior ceiling material 2 | 74.5 | 50 | |
| | Interior ceiling material 3 | 5.5 | 20 | |
| Wall | Cold-resistant material | 92.6 | 20 | 35 |
| | Sidewall | 76.1 | 30 | |
| | End wall | 15.3 | 20 | |
| | Electrical cabinet wall | 47.1 | 20 | |
| | Toilet wall | 28.6 | 20 | |
| | Window glass | 22.4 | 35 | |
| | Toughened glass | 21.5 | 20 | |
| Floor | Cold-resistant material | 78.7 | 25 | 25 |
| | Floorcloth | 76.8 | 15 | |
| | Floor | 78.7 | 20 | |
| Seat | Seat armrest | 73.0 | 6 | 25 |
| | Seat cushion | 18.0 | 50 | |
| | Seat back | 72.0 | 50 | |
| Cable | Cable | 29.2 | 6 | 50 |
| Luggage rack | Luggage rack | 31.5 | 20 | 50 |
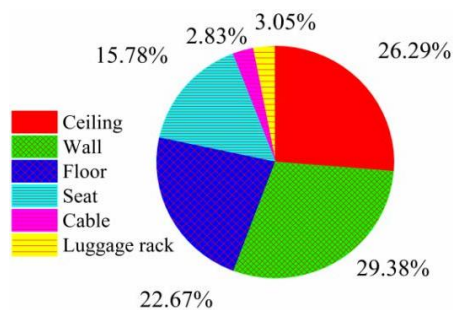


Figure 2: The proportion of the surface area of primary components of a train carriage.

Figure 1b also shows the component's location in the combustion experiment. This component includes two rows of seats and part of the end wall, sidewall, ceiling, luggage rack, and floor material. Figure 3 shows the actual view of the high-speed train component combustion experiment. During the experiment, propane fuel was used as an ignition source, the power of the ignition source was 15 kW, and the duration was 3 min.
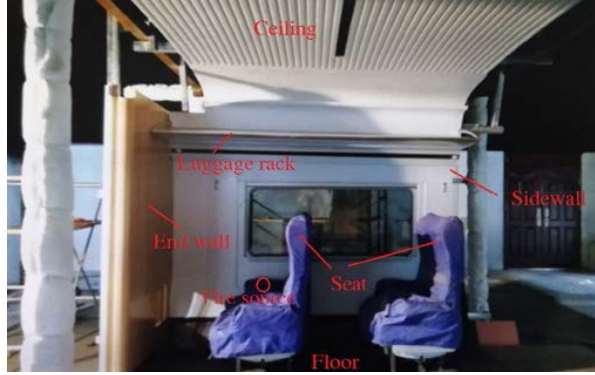


Figure 3: Actual view of the high-speed train component combustion test.

## 2.2   Experimental setup and method

Figure 4 presents a schematic of the cone calorimeter and ignition temperature tester. The radiation intensity received by the material surface of each component was determined according to the research results of Duggan [4].



(a) Schematic cone of calorimeter          (b) Schematic of ignition temperature tester

Figure 4: Schematics of the cone calorimeter and ignition temperature tester.

The cone calorimeter experiments in this study were performed following the ISO 5660-1 standard [12,13]. Before the experiments, each material sample was placed in a constant-climate room at a temperature of $23 \pm 2°C$ and relative humidity of $50 \pm 5\%$ for 48 h. Three combustion experiments were performed for each material to ensure the reproducibility of the experiment results, and the average of the three results was recorded.

The material ignition test was performed following the ASTM D1929 standard [2]. Before the experiment, each material sample was processed according to the method mentioned above. During the experiment, the sample was placed in the furnace tube. The temperature in the furnace tube was continuously adjusted using the thermostat. As the temperature in the furnace tube continued to rise to the point at which the material sample was just ignited, the temperature in the furnace tube was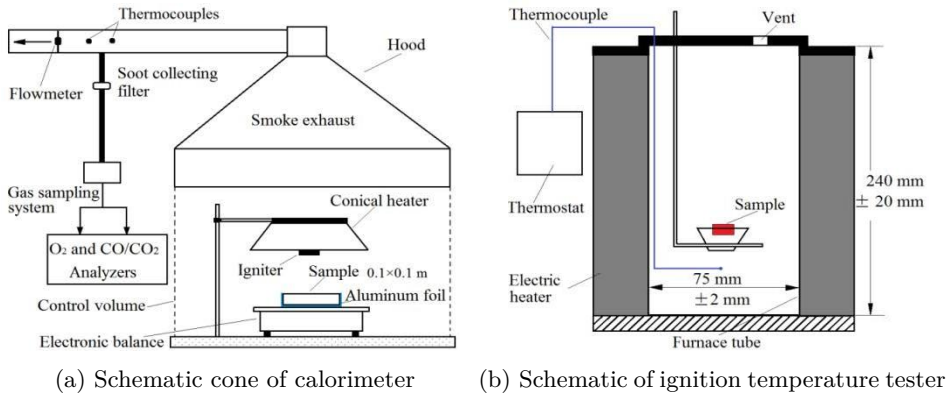 taken to be the ignition temperature of the material. The ignition temperature of each material was measured three times, and then the average value of the test data was taken.

## 2.3    Material heat release rate and ignition temperature

Figure 5 presents the HRRPUA of each combustible material of primary componentsin a high-speed train carriage.When analyzing the influence of the train's primary components on the fire HRR, replacing the material in the original carriage with different materials is necessary. The HRRPUA of each replacement material is shown in Fig. 6. The ignition temperatures of the combustible materials constituting the primary components of the high-speed train carriage are presented in Table 2.



(a) HRRPUA of ceiling material          (b) HRRPUA of wall material
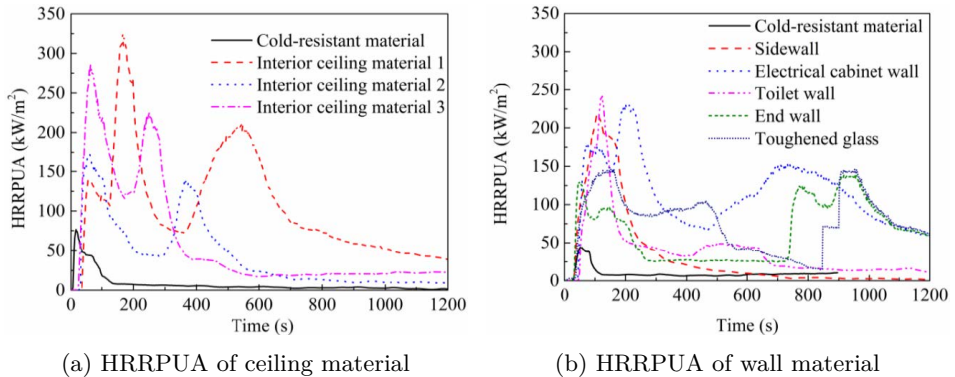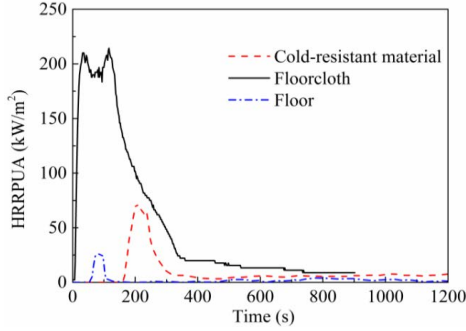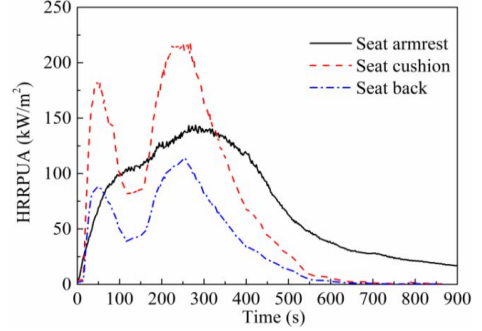
Figure 5: For caption see next page.

(c) HRRPUA of floor material



(d) HRRPUA of seat material
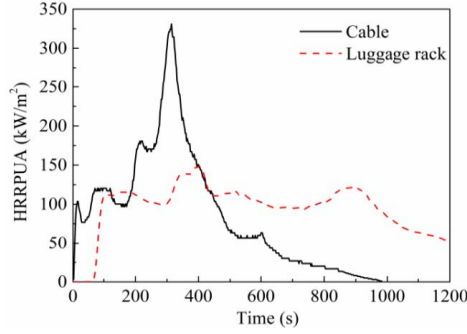


(e) HRRPUA of cable and luggage rack

Figure 5: The heat release rate per unit area of different combustible materials in the train carriage.
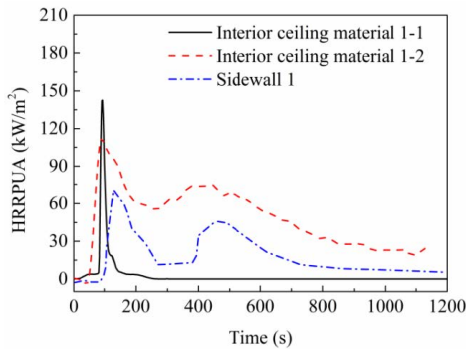


(a) Ceiling and wall
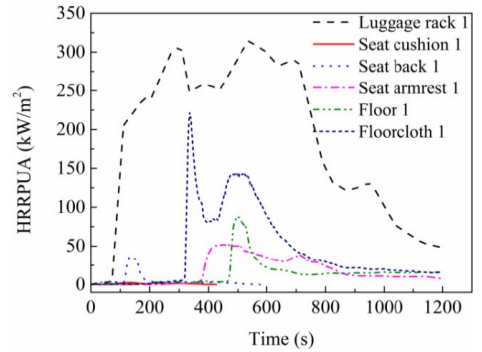


(b) Luggage rack, seat, and floor

Figure 6: The heat release rate per unit area of each replaced material.

Table 2: Ignition temperatures of combustible materials in high-speed trains.

| Structure | Composition | Ignition temperature (°C) |
|---|---|---|
| Ceiling | Cold-resistant material | 278 |
| | Interior ceiling material 1 | 450 |
| | Interior ceiling material 2 | 520 |
| | Interior ceiling material 3 | 526 |
| Wall | Cold-resistant material | 536 |
| | Sidewall | 520 |
| | End wall | 440 |
| | Electrical cabinet wall | 480 |
| | Toilet wall | 470 |
| | Window glass | 600 |
| | Toughened glass | 530 |
| Floor | Cold-resistant material | 450 |
| | Floorcloth | 780 |
| | Floor | 433 |
| Seat | Seat armrest | 350 |
| | Seat cushion | 460 |
| | Seat back | 460 |
| Cable | Cable | 350 |
| Luggage rack | Luggage rack | 526 |

# 3 Numerical method

## 3.1 Governing equations

During a fire, the flow of smoke is a three-dimensional, unsteady, and compressible turbulent flow. The Fire Dynamics Simulator (FDS, version 6.7.4) [14–17] program is used to simulate the train fire (a computational fluid dynamics (CFD) model of fire-driven fluid flow), and the turbulent flow of smoke is solved by the large eddy simulation (LES) [18–20]. The governing equations are shown below [21–24]:

Mass conservation equation

$$\frac{\partial \rho}{\partial t} + \nabla \cdot U\rho = 0, \tag{1}$$

where $t$ is the time, $\rho$ and $U$ are the density and velocity of airflow, respectively.

Component conservation equation

$$\frac{\partial(\rho Y_i)}{\partial t} + \nabla \cdot \rho Y_i U = \nabla \cdot \rho D_i \nabla Y_i + \dot{m}_i''', \tag{2}$$

where $\dot{m}_i'''$ is the mass formation rate of the $i$th component in unit volume, $D_i$ is the component mass diffusion coefficient, and $Y_i$ is the volume fraction of the $i$th component.

Momentum conservation equation

$$\frac{\partial(\rho U)}{\partial t} + \nabla \cdot \rho U U + \nabla P = \rho g + f + \nabla \cdot \tau_{ij}, \tag{3}$$

$$\tau_{ij} = \mu \left[ 2S_{ij} - \frac{2}{3}\delta_{ij}(\nabla \cdot U) \right], \tag{4}$$

$$S_{ij} = \frac{1}{2}\left( \frac{\partial u_i}{\partial x_j} + \frac{\partial u_j}{\partial x_i} \right), \tag{5}$$

$$\delta_{ij} = \begin{cases} 1, & i = j, \\ 0, & i \neq j, \end{cases} \tag{6}$$

where $g$ is the gravitational acceleration, $f$ is the force (except gravity), $\tau_{ij}$ is the viscous stress tensor, $S_{ij}$ is the strain tensor, and $\mu$ is the kinematic viscosity.

Energy conservation equation

$$\frac{\partial(\rho h_s)}{\partial t} + \nabla \cdot U\rho h_s = \frac{Dp}{Dt} - \nabla \cdot \mathbf{q}_r + \nabla \cdot UP + \nabla \cdot k\nabla T + \sum_i \nabla \cdot h_{s,i}\rho D_i \nabla Y_i, \tag{7}$$

where $h_s$ is the sensible enthalpy, $\mathbf{q}_r$ is the radiant heat flux vector, $k$ is the coefficient of heat conductivity, and $T$ is the thermodynamic temperature.

Meanwhile, the state equation of ideal gas was also needed. Its form is shown below:

$$P = \rho R_g T, \tag{8}$$

where $P$ is the pressure, and $R_g$ is the specific gas constant.

When LES is used to solve turbulent flow, the governing equations need to be transformed:

$$\frac{\partial \overline{u}_i}{\partial t} + \frac{\partial \overline{u}_i \partial \overline{u}_j}{\partial x_j} = -\frac{1}{\rho}\frac{\partial \overline{P}}{\partial x_i} + \mu \frac{\partial^2 \overline{S}_{ij}}{\partial x_j \partial x_j} - \frac{\partial(\tau_{ij})}{\partial x_j}, \tag{9}$$

$$\overline{S}_{ij} = \frac{1}{2}\left( \frac{\partial \overline{u}_i}{\partial x_j} + \frac{\partial \overline{u}_j}{\partial x_i} \right), \tag{10}$$

where the the overbar indicates filtering, $\tau_{ij}$ represents the effect of small eddy on large eddy, and it needs to be calculated by establishing a subgrid scale model, such as the Smagorinsky model:

$$\tau_{ij} - \frac{1}{3}\tau_{kk} \cdot \delta_{ij} = -2\overline{S}_{ij} \cdot \mu_{\mathrm{LES}} \, , \tag{11}$$

$$\mu_{\mathrm{LES}} = \rho \left(C_s \Delta\right)^2 \left[2\overline{S}_{ij} \cdot \overline{S}_{ij} - \frac{2}{3}\left(\nabla \cdot \overline{u}\right)^2\right]^{\frac{1}{2}} \, , \tag{12}$$

where $\mu_{\mathrm{LES}}$ is the turbulent viscosity coefficient at a subgrid scale, $C_s$ is the Smagorinsky constant, $u_i$, $u_j$ are the velocity components in $x$ and $y$ direction, and $x_i$, $x_j$ represent the Cartesian coordinates.

## 3.2   Numerical model

Figure 7a shows the numerical model of the high-speed train fire based on the high-speed train carriage structure. The HRRPUAmethod is used



(a) Numerical model of a train fire



(b) Computational domain of the numerical model
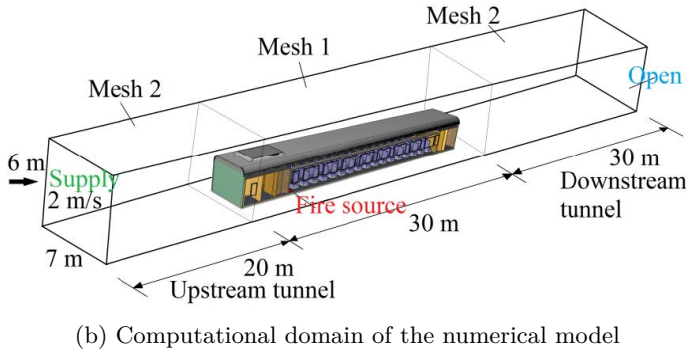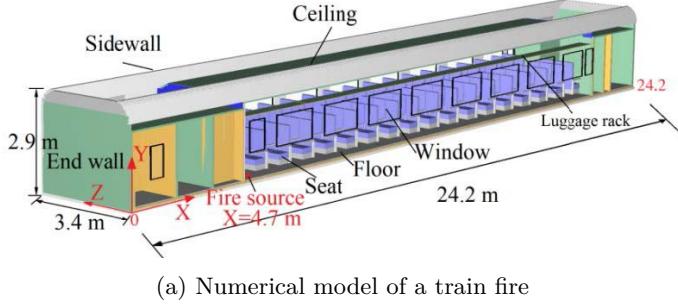
Figure 7: Numerical model of a train fire and the computational domain of the model.

for fire simulation [25, 26]. In this method, it is necessary to input the curve of the HRRPUA and the ignition temperature of each structural material (as shown in Section 2.3). Figure 7b shows the computational domain of the numerical model for a high-speed train fire in a railway tunnel. The width of the tunnel is 7 m, and the height is 6 m. The length of the upstream tunnel is 20 m, and the length of the downstream tunnel is 30 m. The 'supply' boundary condition is applied to the tunnel entrance, and the velocity is 2 m/s [2]. The 'open' boundary condition is applied to the tunnel exit, and the 'inert' boundary condition is applied to the tunnel wall surface.

In this study, the window rupture temperature is 600°C [27]. The door on one side of the train carriage is open before the fire simulation. The fire source is at the end wall corner of the carriage (as shown in Fig. 7a). The fire source power is 150 kW, and the duration is 8 min [2].

## 3.3   Numerical mesh

As shown in Fig. 7b, the computational domain is divided into three regions. The mesh around and inside the train carriage is designated as 'Mesh 1', and that in the upstream tunnel and downstream tunnel is designated as 'Mesh 2'. The size of Mesh 1 is between 0.06 m and 0.10 m; Mesh 2 is twice as large. Figure 8 presents the HRR of train fires (original carriage)
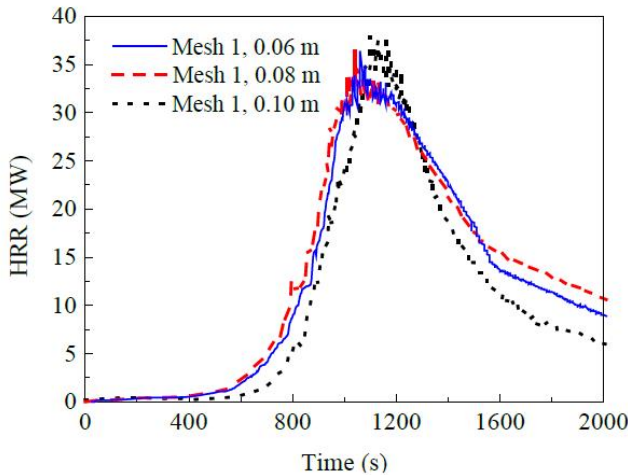


Figure 8: HRR of the train fire with different mesh sizes.

with different mesh sizes. As shown in Figure 8, when the size of Mesh 1 is reduced from 0.08 m to 0.06 m, the difference in the HRR curve of the train carriage fire is minimal. Therefore, in this study, the size of Mesh 1 is set as 0.08 m, the size of Mesh 2 is set as 0.16 m, and the total number of meshes is 2.95 million.

### 3.4 Comparison with component combustionexperiment

Figure 9a shows the FDS model established according to the component structure. The fire source is set on the seat surface. The fire source power is 15 kW, and the duration is 3 min. The mesh size of the FDS model is 0.08 m. Figure 9b presents a comparison between the HRRs of the numerical simulation and the component combustion experiment. The numerical simulation is consistent with the experimental conditions, indicating that the numerical method employed in this study can accurately simulate high-speed train fires.



(a) FDS model

(b) HRR comparison results
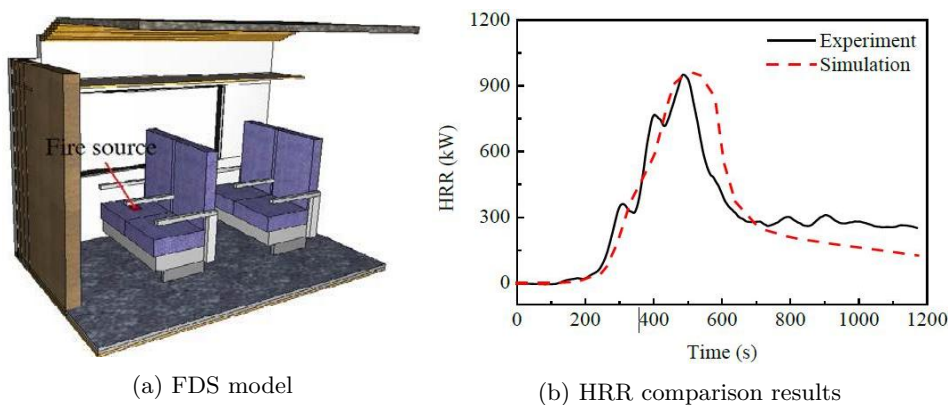
Figure 9: The Fire Dynamics Simulator model and heat release rate comparison results.

## 4    Results and discussion

In this section, the influence of ceilings, sidewalls, luggage racks, seats, and floors on the HRR of high-speed train fire is studied. The fire cases are shown in Table 3. The peak HRRPUA of different materials with the same structure is also given in Table 3.

Table 3: Case for fire simulation.

| Case | Original material | | Replaced material | |
|------|-------------------|--|-------------------|--|
| | Material | Peak HRRPUA $(kW/m^2)$ | Material | Peak HRRPUA $(kW/m^2)$ |
| A | The HRRPUA for all materials was shown in Fig. 5 (original carriage). | | | |
| B | Ceiling: interior ceiling material 1 | 326 | Ceiling: interior ceiling material 1-1 | 140 |
| C | Ceiling: interior ceiling material 1 | 326 | Ceiling: interior ceiling material 1-2 | 110 |
| D | Wall: sidewall | 219 | Wall: sidewall 1 | 123 |
| E | Luggage rack | 150 | Luggage rack 1 | 319 |
| F | Luggage rack | 150 | Luggage rack 2: non-combustible | 0 |
| G | Seat: seat armrest<br>Seat: seat cushion<br>Seat: seat back | 144<br>218<br>114 | Seat: seat armrest 1<br>Seat: seat cushion 1<br>Seat: seat back 1 | 52<br>2.5<br>36 |
| H | Floor: floor cloth<br>Floor: floor | 221<br>26 | Floor: floor cloth 1<br>Floor: floor 1 | 223<br>88 |

## 4.1   Effects of ceilings

The interior ceiling material 1 is the primary material of the ceilings, located on the inner surface of the carriage. Previous papers [1, 2] have studied the fire spread characteristics in the train carriage. The results indicated that when the fire occurs in the carriage, the flame spreads along with the ceiling to both ends of the carriage, causing the materials at both ends of the carriage to burn. The seat and floor then burn owing to the heat radiation from the ceiling. Therefore, whether the fire can spread in the carriage mainly depends on the combustion characteristics of the ceiling materials.

Figure 10 shows the HRR of train carriage fire under different interior ceiling materials 1. The peak HRRPUA of the material under the different cases is shown in Table 3. It can be seen from Fig. 10 that the peak HRR of Case A is 36.4 MW. However, the peak HRRs of Case B and Case C are 19.4 MW and 16.5 MW, respectively. Compared with Case A, the peak HRR of Case B and Case C decreased by 46.7% and 54.7%, respectively. Therefore, the peak HRR of train carriage fire decreases with the decrease of peak HRRPUA of interior ceiling material 1.
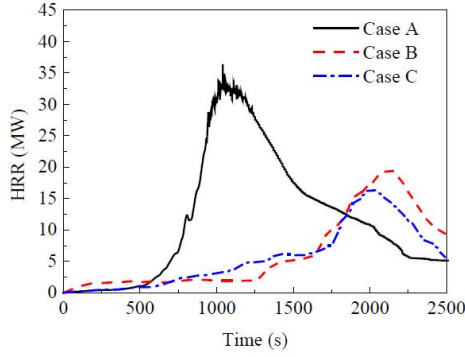
Figure 10: HRR under different ceiling materials.

The time when the train fire reaches the peak HRR is an important parameter in the design fire for train carriages [19]. It can be found from Fig. 10 that the interior ceiling material 1 has a significant influence on the time to peak HRR. The time to peak HRR of the train carriage fire in Case A is approximately 1040 s, while that in Case B and Case C is 2140 s and 2018 s, respectively. Therefore, the interior ceiling material with low HRRPUA can delay the time to peak HRR of the train carriage fire.

Figure 11 shows the HRR growth rate of train carriage fire with different interior ceiling materials 1. The HRR growth rate is calculated as follows:

$$\frac{dQ}{dt} = \frac{\Delta Q}{\Delta t} \,, \tag{13}$$

where $Q$ represents the HRR of the fire, $t$ represents time, $dQ/dt$ represents the HRR growth rate of the fire, and $\Delta t = 60$ s. As shown in Fig. 11, the
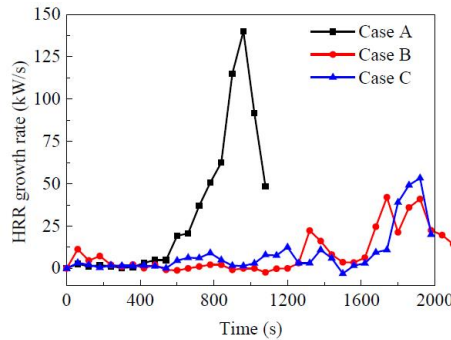


Figure 11: Increasing rate of the train fire HRR under different ceiling materials.

maximum HRR growth rate of Case A is 140 kW/s, while that of Case B and Case C is 41 kW/s and 53 kW/s, respectively. Before 580 s, the HRR growth rate of carriage fire under three cases is relatively close, but after 580 s, the fire HRR of Case A increases rapidly. However, the HRR growth rate of Case B and Case C is low in the whole fire development process.

Figure 12 shows the fire spreading process in the train carriage under three cases. For Case A, when the fire HRR reached the peak, the whole carriage was burning. For Case B and Case C, when the fire HRR reached the peak, the combustion intensity in the train carriage was weak, and some seat and floor materials were not burned. The reason for this phenomenon is that the peak HRRPUA of interior ceiling material 1 in Case B and Case C was low, which reduces the combustion intensity of ceiling material, resulting in the heat radiation on the surface of the seat and floor material being reduced, and some materials were not ignited.
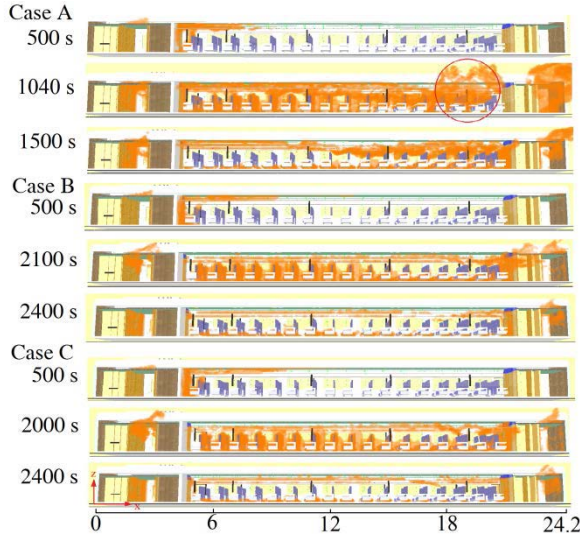


Figure 12: Fire spread in the train carriage.

Figure 13 shows the smoke temperature distribution at 0.1 m below the carriage ceiling in Case A and Case C, respectively. The measuring points are arranged along the train carriage centre line, and the coordinate origin is located at the end wall (as shown in Fig. 7a). It can be seen from Fig. 13 that before the fire HRR reaches the peak, the temperature near the fire source ($x = 4.7$ m) is the highest, and the temperature at both ends of the train carriage is lower. After the fire HRR reaches the peak, the temperature

at the end of the carriage on the right side of the fire source increases. The main reason for this phenomenon is the fire flashover characteristics in the carriage. The previous paper [1] studied the characteristics of fire flashover in train carriages. The results showed that when the HRR reaches the peak, the flashover intensity of the carriage end door area far away from the fire source (as shown in Fig. 12) is the largest, which makes the temperature of the end door area of the carriage increase.



(a) Case A                                (b) Case C
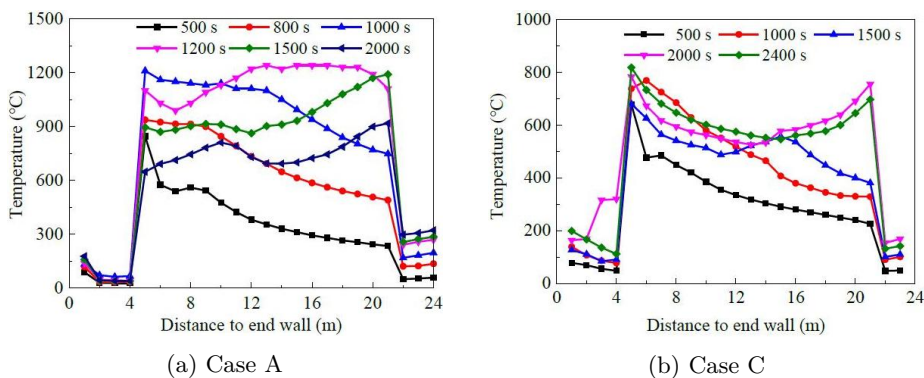
Figure 13: Distribution of smoke temperature below the ceiling at various times.

## 4.2   Effects of sidewalls

This section analyzes the influence of sidewall materials on the HRR of train carriage fire. Figure 14 shows the HRR of train carriage fire under two
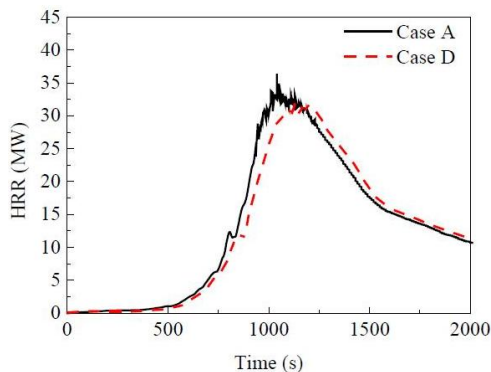


Figure 14: HRR under different sidewall materials.

cases. The peak HRRs for Case A and Case D are 36.4 MW and 31.5 MW, respectively. Compared with Case A, the decreased ratio of peak HRR of Case D is 13.5%. Moreover, the time to peak HRR in Case D is 1140 s, which is 100 s later than in Case A.

Figure 15 shows the temperature distribution on the surface of the sidewall. The temperature measuring point is 1.2 m away from the floor. The maximum temperature of the sidewall surface in Case A and Case D is 1100°C and 980°C, respectively, and the temperature difference is minimal. From the simulation results of the peak HRR and the time to peak HRR in Case A and Case D, it can be seen that reducing the HRRPUA of the sidewall material can not significantly reduce the HRR of the train carriage fire and delay the time to peak HRR. However, there are two reasons for this phenomenon: the first one is that the surface area of sidewall materials is 76.1 m$^2$, which accounts for 7.4% of the total area of train materials. The heat generated by the combustion of sidewall materials accounts for a small proportion of the heat generated by whole train combustion, so it has little impact on the peak HRR of the carriage fire; another reason is that the temperature difference of sidewall surface under different sidewall materials is small, which will not have a significant impact on the combustion of the seat and floor materials.



|              (a) Case A              |              (b) Case D              |
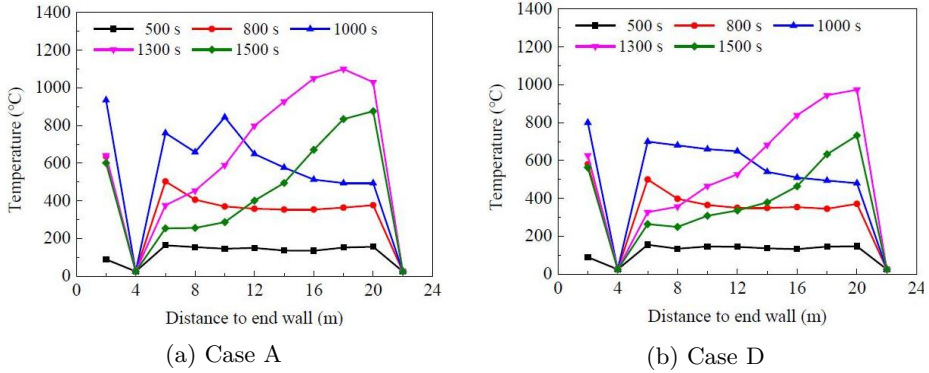
Figure 15: Temperature distribution on the sidewall surface in the carriage.

## 4.3   Effects of luggage racks

Figure 16 shows the HRR of the train carriage fire with different luggage rack materials. The peak HRRs in Case A, Case E, and Case F are 36.4, 36.7, and 34.1 MW, respectively. The peak HRR increases with the increase

of luggage rack material's HRRPUA, but the difference is small. In the three cases, the time to peak HRR is 1040, 1060, and 1240 s, respectively. From the comparison results of the peak HRR of the train carriage fire, whether the luggage rack is combustible or not, the impact of the luggage rack on the peak HRR of the train carriage fire is small. The main reason is that the area of the luggage rack accounts for a small proportion (3.05%) of the train carriage area.
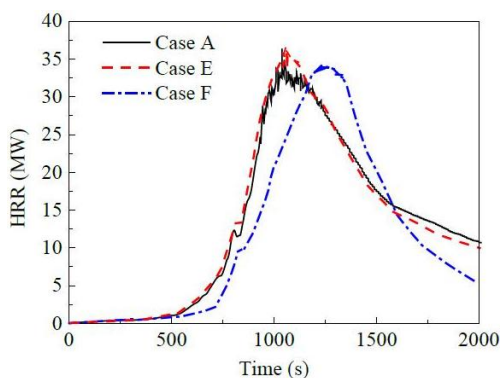


Figure 16: HRR under different luggage rack materials.

As shown in Fig. 16, when the carriage is equipped with a combustible luggage rack, the difference in the time to peak HRR of the train carriage fire is minimal. However, when the non-combustible luggage rack is used, the maximum delay time of the carriage fire HRR to the peak is 200 s. Figure 17 shows the flame spread in the initial growth stage of the fire in the train carriage. When a combustible luggage rack is used, the flame can spread to the ceiling, while when using a non-combustible luggage rack, the flame can not spread to the ceiling in the initial growth stage of fire.



(a) Combustible            (b) Non-combustible
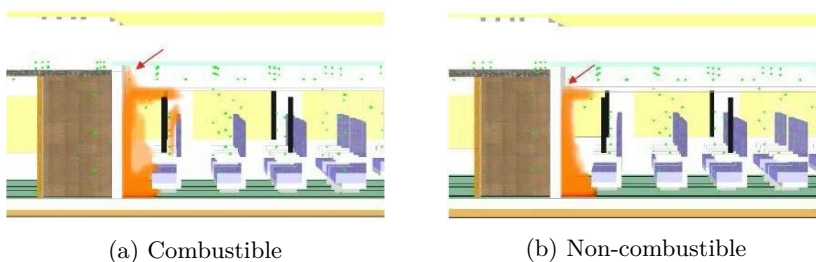
Figure 17: Influence of luggage rack on flame spread.

## 4.4    Effects of seats

Figure 18 shows the HRR of the train carriage fire in Case A and Case G. The peak HRR of Case A is 36.4 MW, and that of Case G is 20.1 MW. Compared with Case A, the reduction ratio of peak HRR of Case G is 44.8%. In Case G, the time to peak HRR is 1480 s, which is 440 s later than in Case A. Therefore, the seat material with low HRRPUA can significantly reduce the peak HRR of the train carriage fire and delay the time to peak HRR.
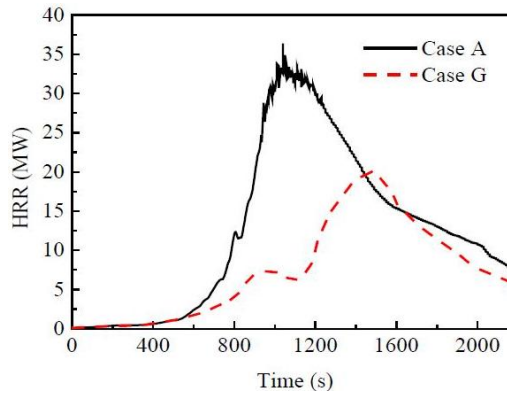


Figure 18: HRR under different seat materials.

Figure 19 shows the HRR growth rate of the carriage fire in Case A and Case G. The maximum HRR growth rate is 140 kW/s and 73 kW/s, respectively. For Case G, the fire HRR growth rate decreases significantly when
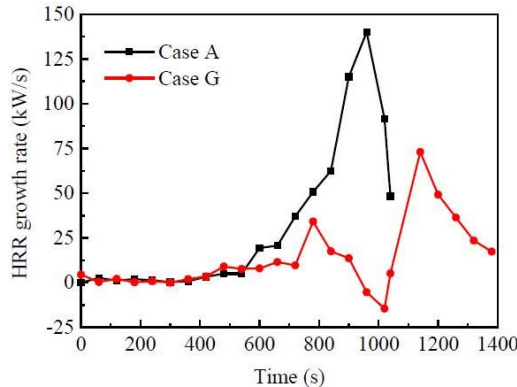


Figure 19: Increasing rate of the train fire HRR under different seat materials.

the fire develops from 780 s to 1020 s. After 1020 s, the fire HRR increases rapidly. The reason for this phenomenon is that: in the initial growth stage of fire development, combustion mainly occurs on the ceiling and the seat surface near the fire source. However, the HRRPUAs of seat materials are low, and the amount of heat generated by combustion is low. With the mass consumption of ceiling material, the HRR of the whole carriage is decreased. Then under the heat radiation of the ceiling, the rest of the seat and floor materials are ignited, and the fire HRR increases rapidly.

## 4.5 Effects of floors

Figure 20 shows the comparison results of fire HRR of Case A and Case H. As shown in Fig. 20, the peak HRR of Case H is 36.9 MW, which is 0.5 MW larger than in Case A. Moreover, the difference in time to peak HRR between the two cases is minimal, and the time to peak HRR is approximately 1040 s.
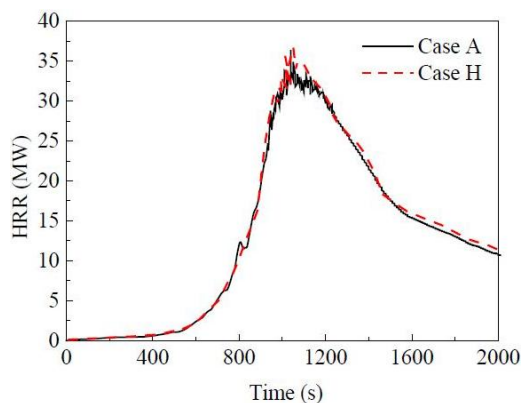


Figure 20: HRR under different floor materials.

Figure 21 shows the temperature distribution in the train carriage of Case A. The temperature near the fire source is the highest in the initial growth stage of the fire development in the carriage. With the development of the fire, the temperature in the carriage increases, and the high-temperature area gradually spreads to the right carriage of the fire source. At 1040 s, the high-temperature area spreads to the whole carriage, and the temperature of the whole ceiling material surface is about 1000°C. At this time, the fire heat release rate reaches a peak.
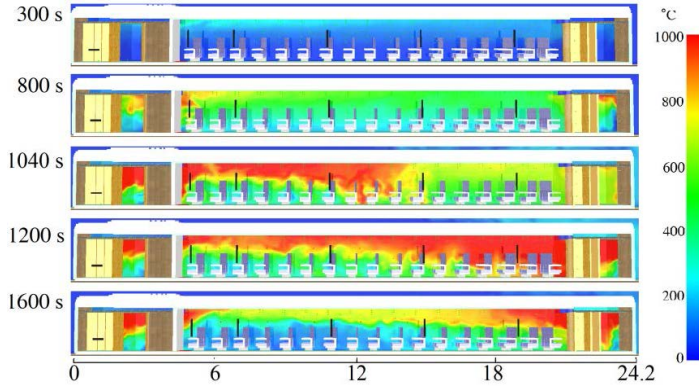
Figure 21: Temperature distribution in the train carriage.

Figure 22 shows the temperature distribution of the floor surface along the length of the train carriage. At the same computing time, the difference in temperature between Case A and Case H is very small. When the HRR of the train carriage fire reaches the peak (at 1040 s), the maximum temperature of the floor surface is approximately 740°C, and the temperature at both ends of the carriage is higher than that in the middle (approximately 360–480°C). However, as shown in Table 2, the ignition temperatures of floor cold-resistant, floor cloth, and floor materials are 450, 780, and 433°C, respectively. Therefore, only a tiny amount of floor material is ignited before the carriage fire reaches its peak. In the late stage of fire development, the temperature of the floor surface at the end of the carriage increases,



(a) Case A



(b) Case H
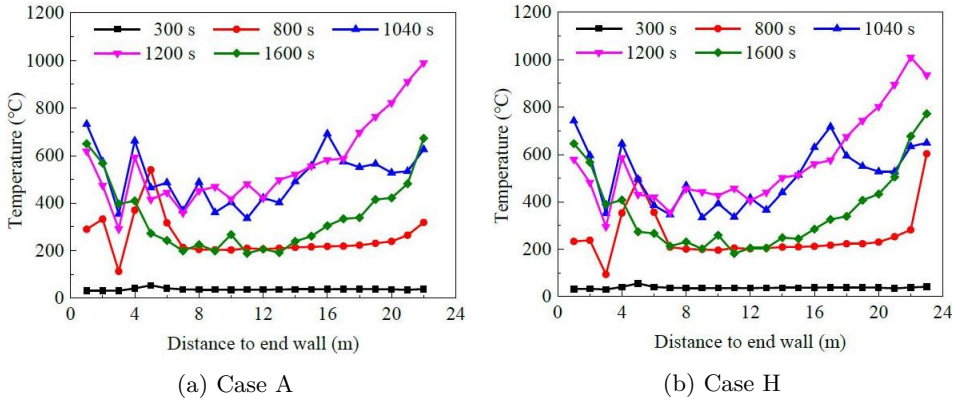
Figure 22: Temperature distribution on the floor surface in the carriage.

and the combustion intensity of the floor material at the end of the carriage increases.

# 5   Conclusions

In this study, based on the HRRPUA and ignition temperature of the high-speed train materials, a numerical model of the high-speed train fire is established. The accuracy of the numerical method is verified by comparing it with the component combustion experiments. Then, the effects of the ceilings, sidewalls, luggage racks, seats, and floors on carriage fire HRR are studied. The following conclusions are drawn:

- The HRRPUA of ceiling material dramatically influences the peak HRR and the time to peak HRR of high-speed train carriage fire. When the peak HRRPUA of interior ceiling material1decreases from $326 \text{ kW/m}^2$ to $110 \text{ kW/m}^2$, the peak HRR of the train carriage fire decreases from 36.4 MW to 16.5 MW, with a reduction ratio of 54.7%. The time to peak HRR increased from 1040 s to 2018 s.

- The sidewall material has a certain influence on the HRR of high-speed train carriage fire. When the peak HRRPUA of sidewall material decreases from $219 \text{ kW/m}^2$ to $123 \text{ kW/m}^2$, the peak HRR decreases from 36.4 MW to 31.5 MW, with a reduction ratio of 13.5%. Moreover, the influence of sidewall material on the surface temperature of the sidewall is small.

- The combustible luggage rack has little effect on the HRR of high-speed train carriage fire. However, the non-combustible luggage rack can delay the time when the HRR reaches its peak.

- The HRRPUA of seat material greatly influences the HRR of high-speed train carriage fire. When seat materials with low HRRPUA are used, the peak HRR of carriage fire is 20.1 MW, and the reduction ratio is 44.8%. Moreover, the time to peak HRR is delayed by 440 s.

- The combustion intensity of the floor materials in the high-speed train carriage is low. The HRRPUA of the floor materials has little effect on the HRR of the high-speed train carriage fire.

Although the research in this paper was carried out for specific train types, the research conclusions were also applicable to other high-speed train fires.

Moreover, the research results can provide guidance for the design of the high-speed train structure and fire protection, as well as the establishment of the calculation method of the high-speed train fire HRR.

# References

[1] Bi H.Q., Zhou Y.L., Wang H.L., Gou Q.L., Liu X.X.: *Characteristics of fire in high-speed train carriages.* J. Fire Sci. **38**(2020), 1, 75–95. doi: 10.1177/0734904119894527

[2] Zhou Y.L., Wang H.L., Bi H.Q., Liu X.X., Gou Q.L.: *Heat release rate of high-speed train fire in railway tunnels.* Tunn. Undergr. Sp. Tech. **105**(2020), 103563. doi: 10.1016/j.tust.2020.103563

[3] White N.: *Fire development in passenger trains.* PhD thesis, Victoria University, Melbourne 2010.

[4] Duggan G.J.: *Fire hazards, testing, materials and products.* In Proc. Conf. on Usage of ISO 5660 Data in UK Railway Standards and Fire Safety Cases, Rubber and Plastics Institute (Rapra), Shrewsbury, 13 March 1997, 1–8.

[5] Craig M., Asim T.: *Numerical investigations on the propagation of fire in a railway carriage.* Energies **13**(2020), 19, 4999. doi: 10.3390/en13194999

[6] Peacock R.D., Braun E.: *Fire Tests of Amtrak Passenger Rail Vehicle Interiors. Final Report.* 1978–1983 (Natl. Bur. Stand. Tech. Note 1193). NIST TN 1193, Washington, DC, 1984. doi: 10.6028/Nbs.tn.1193

[7] Lslam M.T., Klinger J.L., Reza M.T.: *Evaluating combustion characteristics and combustion kinetics of corn stover-derived hydrochars by cone calorimeter.* Chem. Eng. J. **452**(2023), 2, 139419. doi: 10.1016/j.cej.2022.139419

[8] Hirschler M.M.: *Use of heat release rate to predict whether individual furnishings would cause self propagating fires.* Fire Safety J. **32**(1999), 3, 273–296. doi: 10.1016/S0379-7112(98)00037-X

[9] Kim J.S., Jeong J.C., Cho S.H., Seo S.I.: *Fire resistance evaluation of a train car body made of composite material by large scale tests.* Compos. Struct. **83**(2008), 3, 295–303. doi: 10.1016/j.compstruct.2007.04.022

[10] Lee D.H., Park W.H., Jung W.S., Hwang J.H.: *Fire test of old type interiors of subway vehicle in ISO 9705 room.* J. Korean Soc. Rail. **13**(2010), 5, 481–487.

[11] Lönnermark A., Ingason H., Li Y.Z., Kumm M.: *Fire development in a 1/3 train carriage mock-up.* Fire Safety J. **91**(2017), 432–440. doi: 10.1016/j.firesaf.2017.03.016

[12] Ryu S., Mun S.Y., Hwang C.H.: *Effect of the cone heater scale compliant with the ISO 5660 standard on spatial uniformity of radiant heat flux.* Fire Sci. Eng. **34**(2020), 5, 27–33. doi: 10.7731/KIFSE.ad1befcd

[13] Knez N., Kariž M., Knez F., Ayrilmis N., Kuzman M.K.: *Effects of selected printing parameters on the fire properties of 3d-printed neat polylactic acid (PLA) and wood/PLA composites.* J. Renew. Mater. **9**(2021), 11, 1883–1895. doi: 10.32604/jrm.2021.016128

[14] Wang Z.Y., Ji J., Tan T.T., Gao Z.H., Zhou Y., Zhou F.: *Numerical study on the critical criterion for predicting the plug-holing under lateral mechanical exhaust in tunnel fires: Considering the effect of smoke flow in longitudinal direction.* Tunn. Undergr. Sp. Tech. **128**(2022), 104666. doi: 10.1016/j.tust.2022.104666

[15] Fan, C., Zhang, L., Jiao, S., Yang, Z., Li, M., Liu, X.: *Smoke spread characteristics inside a tunnel with natural ventilation under a strong environmental wind.* Tunn. Undergr. Sp. Tech. **82**(2018), 99–110. doi: 10.1016/j.tust.2018.08.004

[16] Liu Y., Shen J., Ma J., Li G., Zhao Z., Ni X., Wang X.: *Laser-based measurement and numerical simulation of methane-air jet flame suppression with water mist.* Process Saf. Environ. Protect. **148**(2021), 1033–1047. doi: 10.1016/j.psep.2021.02.028

[17] Zhao J., Xu Z., Ying H., Guan X., Chu K., Tagne S.M.S., Tao H.: *Study on smoke spread characteristic in urban interval tunnel fire.* Case Stud. Therm. Eng. **30**(2022), 101755. doi: 10.1016/j.csite.2022.101755

[18] Zhang M., Ong J.C., Pang K.M., Bai X.S., Walther J.H.: *Large eddy simulation of soot formation and oxidation for different ambient temperatures and oxygen levels.* Appl. Energ., **306**(2022), 118094. doi: 10.1016/j.apenergy.2021.118094

[19] Liu Y.X., Liu C.H., Brasseur G.P., Chao C.Y.H.: *Proper orthogonal decomposition of large-eddy simulation data over real urban morphology.* Sustain. Cities Soc. **25**(2022), 104324. doi: 10.1016/j.scs.2022.104324

[20] Peterson D.M.: *Simulation of a round supersonic combustor using wall-modelled large eddy simulation and partially-stirred reactor models.* P. Combust. Inst. (2022). doi: 10.1016/j.proci.2022.08.120

[21] Zhou Y.L., Wang H.L., Bi H.Q., Wang J.: *Experimental and numerical study of aerodynamic pressures on platform screen doors at the overtaking station of a high-speed subway.* Build. Environ. **191**(2021), 107582. doi: 10.1016/j.buildenv.2020.107582

[22] Bi H.Q., Wang Z.H., Wang H.L., Zhou Y.L.: *Aerodynamic phenomena and drag of a maglev train running dynamically in a vacuum tube.* Phys. Fluids **34**(2022), 9, 096111. doi: 10.1063/5.0104819

[23] Korib K., Ihaddadene N., Bouakkaz R., Khelili Y.: *Numerical simulation of forced convection of nanofluid around a circular cylinder.* Arch. Thermodyn. **40**(2019), 2, 3–16. doi: 10.24425/ather.2019.129539

[24] Saeed F.R., Al-Dulaimi M.A.: *Numerical investigation for convective heat transfer of nanofluid laminar flow inside a circular pipe by applying various models.* Arch. Thermodyn. **42**(2021), 1, 71–95. doi: 10.24425/ather.2021.136948

[25] Beji T., Merci B.: *Numerical simulations of a full-scale cable tray fire using small-scale test data.* Fire Mater. **43**(2019), 5, 486–496. doi: 10.1002/fam.2687

[26] Chen Y.J., Shu C.M., Ho S.P., Kung H.C., Chien S.W., Ho H.H., Hsu W.S.: *Analysis of smoke movement in the Hsuehshan tunnel fire.* Tunn. Undergr. Sp. Tech. **84**(2019), 142–150. doi: 10.1016/j.tust.2018.11.007

[27] Li Y.Z., Ingason H.: *A new methodology of design fires for train carriages based on exponential curve method.* Fire Technol. **52**(2016), 5, 1449–1464. doi: 10.1007/s10694-015-0464-3

# Heat transfer and friction characteristics in three-side solar air heaters with the combination of multi-v and transverse wire roughness

**DHANANJAY KUMAR**[*]

B.A. College of Engineering and Technology, Ghutia, P.O. Barakhurshi
Jamshedpur, Jharkhand 832304, India

**Abstract** The present paper describes the experimental analysis of heat transfer and friction factor for glass protected three-side artificially roughened rectangular duct solar air heaters (SAHs) having an arrangement of multiple-v and transverse wires (top wall multi-v and two side walls transverse) under the absorber plate, and compares their performance with that of one-side roughened solar air heaters under similar operating conditions. The investigated three-side solar air heaters are characterized by a larger rate of heat transfer and friction factor as compared to one-side artificially roughened SAHs by 24–76% and 4–36%, respectively, for the identical operating parameters. The air temperature below the three-side rugged duct is by 34.6% higher than that of the one-side roughened duct. Three-side solar air heaters are superior as compared to one-side artificially roughened solar air heaters qualitatively and quantitatively both.

**Keywords:** Absorber plate; Fluid flow; Heat transfer; Solar air heater; Reynolds number; Relative roughness height

## Nomenclature

$A_o$    –    area of orifice plate m$^2$
$A_p$    –    area of absorber plate, m$^2$
$H$    –    depth of the duct, m

---

[*]Corresponding Author. Email: dhananjaykumar84nit@gmail.com

$C_p$      –   specific heat of air at constant pressure, J/kgK
$D_h$      –   hydraulic diameter of solar air heater, $= 4WH/2(W + H)$, m
$d/w$      –   relative gap position
$e$        –   artificial roughness height, m
$f_r$      –   average friction factor
$e/D_h$    –   relative roughness height
$g$        –   gravitational acceleration, m/s$^2$
$h$        –   convective heat transfer coefficient, W/m$^2$K
$\Delta h_1$   –   difference in height of U-tube manometer fluid column, m
$\Delta h_2$   –   difference in height of micromanometer fluid column, m
$I$        –   intensity of solar radiation, W/m$^2$
$k$        –   thermal conductivity of air, W/m K
$L$        –   length of test section, m
$\dot{m}$  –   mass flow rate of air, kg/s
$\mathrm{Nu}_r$   –   average Nusselt number
$P$        –   roughness pitch, m
$Q_u$      –   heat gain, W
$P/e$      –   relative roughness pitch
$\Delta P_O$   –   pressure difference in U-tube manometer, Pa
$\Delta P_d$   –   pressure difference in micromanometer, Pa
$\mathrm{Re}$   –   Reynolds number
$t_a$      –   ambient temperature, K
$t_i$      –   inlet air temperature, K
$t_O$      –   outlet air temperature, K
$t_p$      –   average plate temperature, K
$t_f$      –   average air temperature, K
$\Delta t$ –   change in temperature, K
$V$        –   velocity of air inside the duct, m/s
$W$        –   width of duct, m
$w$        –   roughness width, m
$W/H$      –   duct aspect ratio
$W/w$      –   relative roughness width

**Greek symbols**

$\alpha$   –   angle of attack, degree
$\beta$    –   ratio of orifice diameter to pipe diameter
$\rho$     –   density of air, kg/m$^3$
$\rho_1$   –   density of fluid used in U-tube manometer, kg/m$^3$
$\rho_2$   –   density of fluid used in micromanometer, kg/m$^3$
$\mu$      –   dynamic viscosity of the air, kg/ms

**Subscripts**

$1r$   –   one side roughened duct
$3r$   –   three side roughened duct

# 1    Introduction

The thermal performance of a traditional solar air heater (SAH) is generally deficient due to a low rate of convective heat transfer between the absorber plate and air flowing in the duct. The low convective heat transfer coefficient is normally attributed to the occurrence of a viscous sub-layer, which can be broken by providing synthetic roughness on the air flow side of the absorber plate [1, 5, 6]. This creates turbulence in flow, so the effect of thermal resistance reduces and the heat transfer rate becomes enhanced [7, 10]. Solar air collector is a device in which the air is delivered through a four-sided cross-section duct underneath a metallic absorber plate with its sun-facing side black coated to enable immersion of incoming solar radiation and convert it into thermal energy. The glass shield is placed over the rectangular duct to reduce the convective and radiative losses [11–15]. The animated air is used for numerous applications such as space warming, crop drying, seasoning of timber and industrial purpose [16–18]. A schematic representation of a conventional SAH is illustrated in Fig. 1.
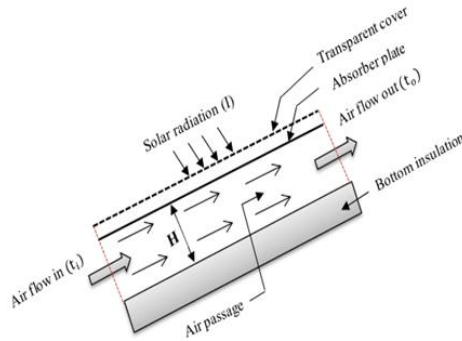


Figure 1: Schematic representation of traditional SAH.

The number of experimental and theoretical inquiries has been authorized by many investigators with fabricated roughness geometries on the absorber plate of the SAH duct [19–21]. The fabricated roughness was applied on a single side, double sides or three-sides of the absorber plate walls. Karwa and Chitoshiya made a tentative analysis of thermo-hydraulic performance of SAH with 60° v-down discrete rib roughness on the air-flow side of the absorber plate along with that of plain SAHs [22]. Kumar *et al.* [23] established the results of investigations of the effect of multi v-shaped ribs with gap roughness in one broad wall and found that an increase in the Nusselt number and friction factor as compared to plain SAHs can be 6.74

and 6.37 times, respectively. Maithani and Saini made attempts to increase the heat transfer factor of a SAH duct roughened in the form of v-shaped ribs through regular gaps as turbulence promoters [24]. Gupta *et al.* [25] installed the inclined ribs as an inclined state which carried greater thermal enactment as related to a transverse and flat plate SAH duct; they also evaluated the thermohydraulic enactment analytically. Deo *et al.* [26] made investigations using multi-gap v-down ribs joined through staggered ribs on the major wall, i.e. on the absorber plate of SAH. Prasad *et al.* [27] analytically inspected the impact of transverse round wire ribs as a fabricated roughness three-side rugged SAH duct, and reported that it is superior as compared to one-sided transverse ribs. Using a mathematical model, the thermal and effective efficiency aspect of discrete v-down rib roughness was inspected by Singh *et al.* [28]. Behura *et al.* [21] experimentally explored the characteristics of heat transfer, friction factor and thermal enactment of an innovative type of three-side artificially roughened SAH with lead crystal shield under completely developed turbulent flow circumstances and stated that three-side artificially roughened SAHs are grander to those of one-side roughened SAHs qualitatively and quantitatively both. Kumar *et al.* [31] empirically inspected the influence of geometrical restrictions of multi v-shaped ribs with a gap on heat transfer and fluid flow characteristics of a four-sided duct SAH over an animated plate having rib roughness on its underneath and found that the maximum increase in the Nusselt number and friction factor are 6.32 and 6.12 times with respect to that of a plain duct, respectively. Different types of rib arrangements are revealed in Table 1.
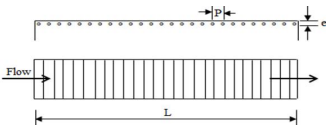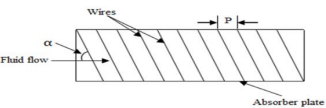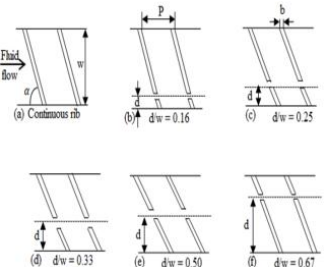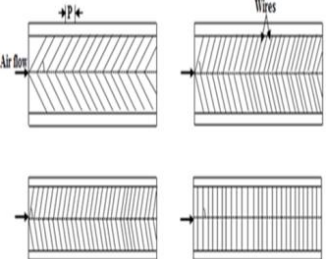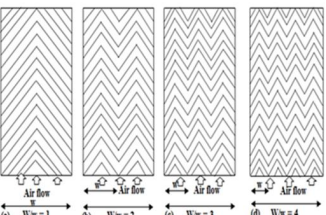
In this exploration, innovative roughness geometry *viz.* an alignment of multiple-v and transverse wire roughness is recommended for tentative inquiry in a SAH with parallel boundary conditions. The main intentions of the present investigations are:

I. To review the effect of relative roughness pitch ($P/e$), and relative roughness height ($e/D_h$) at varying values of Reynolds number (Re) on the heat transfer and friction factor of SAH roughened with three-side (top wall multi-v and two side walls transverse) wire with the existing roughness geometry and compare with the values acquired applying the one-side roughened duct to estimate the improvement in enactment of the solar air heaters.

II. To compare the heat transfer and friction factor for the offered roughness outline of three-side roughened SAHs with other greatest per-

forming outcomes of the multiple-v ribs roughness as stated by Hans *et al.* [30].

III. To recommend the best performing configurations and inspect roughness geometry limitations.

Table 1: Distinct types of rib arrangements

| Arrangement | Roughness limitations | Roughness geometry | Reference |
|---|---|---|---|
| Transverse continuous ribs | $P/e = 10-20$<br>$e/D_h = 0.020-0.033$<br>Re = 5000–50000 |  | Prasad and Saini [15] |
| Inclined continuous ribs | $P/e = 10$<br>$e/D_h = 0.020-0.053$<br>$W/H = 6.8-11.5$<br>$\alpha = 30°-90°$<br>Re = 5000–30000 |  | Gupta *et al.* [25] |
| Inclined with gap ribs | $P/e = 10$<br>$e/D_h = 0.0377$<br>$d/w = 0.167-0.5$<br>$g/e = 0.5-2.0$<br>Re = 5000–30000 |  | Aharwal *et al.* [32] |
| V-shaped continuous ribs | $P/e = 10$<br>$e/D_h = 0.020-0.034$<br>$\alpha = 30°-90°$<br>Re = 2500–18000 |  | Momin *et al.* [33] |
| Multi v-shaped ribs | $P/e = 6-12$<br>$e/D_h = 0.019-0.043$<br>$W/w = 1-10$<br>$\alpha = 30°-75°$<br>Re = 2000–20000 |  | Hans *et al.* [30] |

## 2 Experimental set-up and procedure

The experimental set-up has been elaborated to study the effect of rectangular duct SAH, adopting an alignment of multi-v and transverse wire ribs as a roughness geometry, on heat transfer and fluid flow characteristics. The three-side synthetically roughened SAH duct with a three-side lead crystal cover was investigated. At the same time, a one-side synthetically roughened SAH duct was also considered with only a top-side lead crystal cover. Figure 2 illustrates the three-side synthetically rugged solar air heater duct whereas Fig. 3 illustrates the one-side synthetically roughened SAH. The SAH ducts have a 200 mm × 25 mm flow cross-section as presented in Figs. 2 and 3.
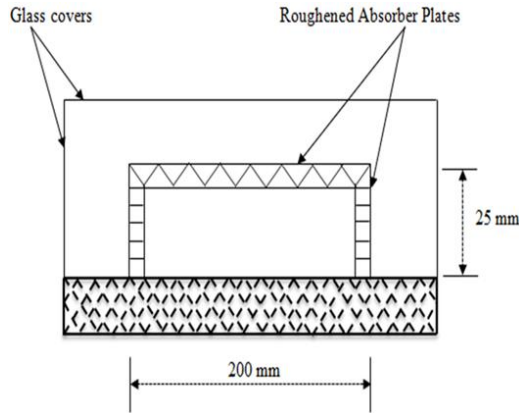


Figure 2: Three-side roughened solar air heater duct.
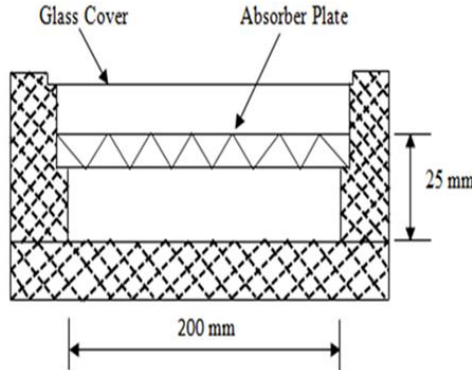


Figure 3: One-side roughened solar air heater duct.

Figures 4 and 5 demonstrate the roughened top and side absorber plates for three-side rugged SAHs having a galvanised iron (GI) sheet of 0.6 mm thickness. The photographic views are also shown in Figs. 6 and 7, respectively. The inner face of the remaining side of the duct is plane wooden. The duct was linked to a single blower to run accurately.
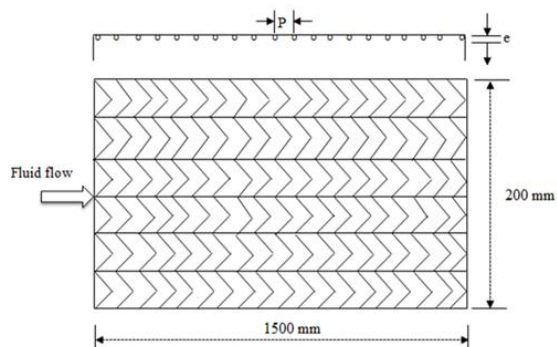
Figure 4: Top absorber plate for both 1-side and 3-side roughened SAH.
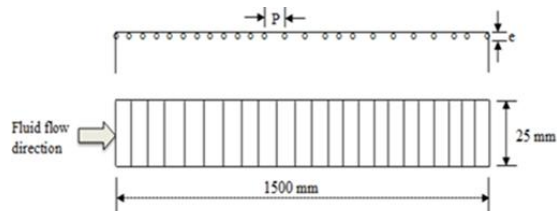
Figure 5: Side absorber plate for 3-side roughened SAH.
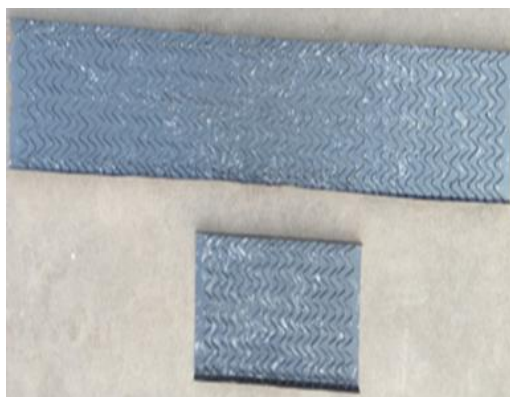
Figure 6: Photograph of the absorber plate for both 1-side and 3-side rugged SAHs.
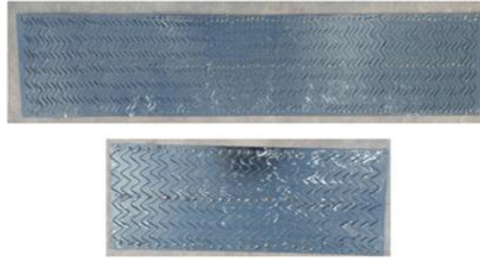
Figure 7: Photograph of top absorber plate for 1-side roughened SAHs.

The schematic presentation of the experimental set-up is shown in Fig. 8. It consists of an entry segment, test segment, a stream meter and a centrifugal blower. The two ducts, both one-side and three-side, are parallel in the measurement and are 2 m long, 0.2 m wide, and 0.025 m high. For both one-side and three-side synthetically rugged SAH ducts, only 1.5 m of duct length acts as the test segment and 0.5 m as the drift equalization bell-connected entrance segment. The solar collector entry segment was prohibited from solar emissions. Subsequently, the flow can be presumed to be absolutely established turbulent flow in the whole test segment length. The mass flow
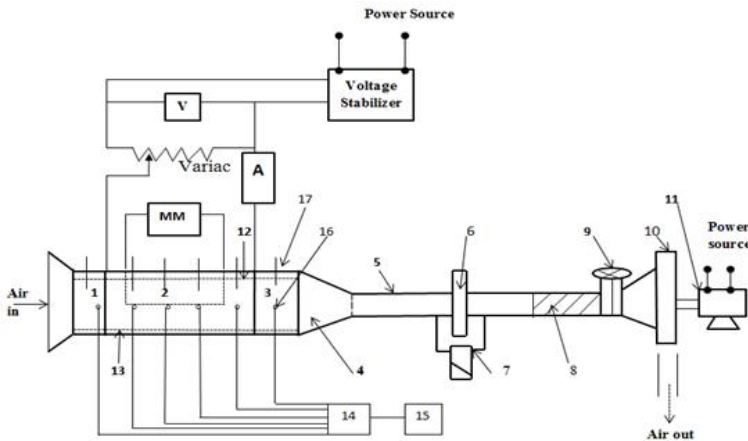


Figure 8: Schematic presentation of the experimental set-up: 1 – unheated entry section, 2 – heated test section, 3 – exit section, 4 – transition section, 5 – flow pipe, 6 – orifice meter, 7 – U-tube manometer, 8 – flexible pipe, 9 – gate valve, 10 – blower, 11 – electric motor, 12 – absorber plate, 13 – bottom of the duct, 14 – selectors switch, 15 – temperature recorder, 16 – thermocouple, 17 – digital thermometer, A – ammeter, MM – micromanometer, V – voltmeter.

rate of air in the duct was measured by a flange-tap orifice meter adapted in the stream channel; a blower using an auto-variac (variable transformer) associated with a stream tube for regulating the mass flow rate.

Figure 9 shows a photograph of the experimental set-up where a duct $P$ is one-side rough, Q is the smooth duct and duct $R$ is three-side roughened duct. To measure the fluid temperature, differential thermometers with a least count of 0.1 K were used, however, copper-constantan thermocouples of 28 SWG (British, Standard Wire Gage) were used for plate temperature measurements. Multi-tube manometers were linked to the pressure taps in the test segment ducts for measuring the pressure gradient. A digital pyranometer driven by a solar panel was used for distinguished measurements of the intensity of solar radiation, as shown in the photograph presented in Fig. 10.



Figure 9: Photographic representation of experimental set-up with three ducts.

Experimental data on heat transfer and friction factor was collected as per the recommendation of ASHRAE standard 93–97 (1977) [29] for the analysis of solar collector performance in an open loop flow mode. The data were gathered from the fluid side of the absorber plate for several arrangements of geometrical restrictions of the proposed synthetic rib roughness. Wood was chosen between other materials to construct the duct as it is cheap, easily obtainable and has also isolating properties. For the three-side roughened SAH, the top wall was set at four values of angle of attack ($\alpha = 30°$, 45°, 60°, and 75°) and side walls were perpendicular to the fluid stream direction at variable values of relative roughness pitch, $P/e$, in the range of 10–25, and relative roughness height, $e/D_h$, in the range of 0.018–0.042. The flow Reynolds number (Re) varied between 3000–12 000. At the initial

Figure 10: Photograph of digital pyranometer system.

stage of each measurement series, it was made sure that all measuring instruments work correctly and that there was no leakage at the joints. All measurements were made under steady-state conditions. For each measurement series, it takes 3–4 hours to reach the steady-state conditions from the start. The steady-state was expected to have been accomplished when no substantial deviation in the plate temperature and outlet air temperature was observed over a period of 15 minutes. The parameters recorded for each set were the following: inlet and outlet air temperature, absorber plate temperature at six points in the span-wise direction of the duct, trial section pressure head and orifice plate pressure gradient. In order to compare the performance of the three-side roughened SAH (top wall multi-v and two side walls transverse) versus one-side rugged SAH duct and the results of heat transfer and friction factor reported by Hans *et al.* [30], the ducts were tested under identical conditions.

# 3   Data collection and reduction

The experimental data were gathered from 12 arrangements of the roughened absorber plates and sixty tests for both one-side and three-side synthetically roughened SAHs simultaneously. The flow constraints remained

identical for both categories of roughened SAHs for an individual test series, the records were made under the actual outdoor conditions. For a particular day, data were collected for an assumed mass stream rate under fluctuating values of intensity of solar radiation between 11:00 a.m. to 2:00 p.m. The hydraulic diameter for both SAH ducts is equal to 0.04444 m and the ducts are arranged in parallel. Some metrological data on a specific day are revealed in Table 2. The range of roughness and flow limitations are exposed in Table 3.

Table 2: Some metrological records

| Metrological parameters | Time (hr) | | | | | | | | | | | | |
|---|---|---|---|---|---|---|---|---|---|---|---|---|---|
| | 11:00 | 11:15 | 11:30 | 11:45 | 12:00 | 12:15 | 12:30 | 12:45 | 13:00 | 13:15 | 13:30 | 13:45 | 14:00 |
| Ambient temperature (°C) | 35.8 | 36.5 | 36.7 | 36.9 | 37.5 | 38.3 | 38.6 | 38.9 | 39.4 | 39.7 | 39.9 | 40.0 | 40.1 |
| Wind speed (m/s) | 0.6 | 1.7 | 1.8 | 2.5 | 2.4 | 1.4 | 2.1 | 1.6 | 2.1 | 0.0 | 4.4 | 1.5 | 2.4 |
| Ambient pressure $\times 10^2$ Pa | 985.7 | 985.5 | 985.5 | 985.3 | 985.1 | 985.0 | 984.8 | 984.0 | 984.0 | 983.0 | 983.4 | 983.3 | 981.5 |
| Total radiation (W/m$^2$) | 878 | 892 | 903 | 903 | 898 | 879 | 868 | 844 | 821 | 808 | 790 | 761 | 729 |
| Diffuse radiation (W/m$^2$) | 279 | 281 | 282 | 287 | 281 | 284 | 288 | 286 | 286 | 271 | 279 | 2264 | 262 |
| Direct radiation (W/m$^2$) | 607 | 611 | 617 | 611 | 612 | 595 | 587 | 580 | 578 | 574 | 574 | 559 | 546 |
| Normal radiation (W/m$^2$) | 621 | 626 | 632 | 631 | 632 | 614 | 601 | 593 | 596 | 592 | 600 | 579 | 567 |
| Relative humidity (%) | 43 | 41 | 41 | 40 | 40 | 38 | 39 | 37 | 35 | 28 | 27 | 29 | 27 |

Table 3: Standards of roughness and flow restrictions

| Parameter | Symbol | Values |
|---|---|---|
| Relative roughness pitch | $P/e$ | 10–25 (4 levels) |
| Relative roughness height | $e/D_h$ | 0.018–0.042 (4 levels) |
| Angle of attack | $\alpha$ | 30°–75° (4 levels) |
| Relative roughness width | $W/w$ | 6 (1 level) |
| Reynolds number | Re | 3500–12 000 (6 levels) |

The experimental records for plate and air temperatures at several positions in the conduit were collected under steady-state conditions for a specified heat flux and mass stream rate of air. The information was used to compute the heat allocation rate to air streaming in the duct. In order to estimate the Nusselt number ($\mathrm{Nu}_r$) and friction factor ($f_r$) the effect of roughness orientation and operating parameters on heat transfer and friction factor was investigated.

The consequent equations have been used for the estimation of mass flow rate ($\dot{m}$), useful heat gain ($Q_u$), heat transfer coefficient ($h$), Nusselt number ($\mathrm{Nu}_r$), Reynolds number (Re) and friction factor ($f_r$). These equations were obtained by adopting experimental observations as described in the subsequent steps.

The mass stream rates have been determined from the pressure gradient measurement across the orifice plate:

$$\dot{m} = C_d A_o \left[ \frac{2\rho \Delta P_o}{1 - \beta^4} \right]^{0.5} . \tag{1}$$

The calibration of the orifice plate against a standard Pitot tube yielded the value of the discharge coefficient $C_d$ as 0.624, where $P_o = g\rho_1 \Delta h_1$.

The rate of heat gain by the air and heat transfer coefficient for one-side and three-side synthetically roughened solar collectors can be determined by adopting a relationship

$$Q_u = \dot{m} C_p (t_o - t_i) = h A_p (t_p - t_f) . \tag{2}$$

The average value of plate temperature ($t_p$) was determined from the detailed temperature profile of the absorber plate indicated by six thermocouples at several positions:

$$t_p = \frac{t_{p1} + t_{p2} + t_{p3} + t_{p4} + t_{P5} + t_{p6}}{6} . \tag{3}$$

The average value of fluid temperature ($t_f$) was determined from the detailed temperature profile of air in the channel by six digital thermometers at several positions in the test section of the duct:

$$t_f = \frac{t_{f1} + t_{f2} + t_{f3} + t_{f4} + t_{f5} + t_{f6}}{6} . \tag{4}$$

The Reynolds number for the one-side and three-side roughened solar collector was calculated assuming an equation

$$\mathrm{Re} = \frac{\rho V D_h}{\mu} . \tag{5}$$

The Nusselt number for the one-side and three-side rugged solar collector was calculated assuming a relation

$$\mathrm{Nu}_r = \frac{hD_h}{k} \,.$$ (6)

The friction factor was determined from the flow velocity ($v$) and pressure drop ($\Delta P_d$) through the test segment by applying the Darcy-Wiesbach equation:

$$f_r = \frac{2\Delta P_d D_h}{4\rho L V^2} \,,$$ (7)

where the hydraulic diameter $D_h = \dfrac{4WH}{2(W+H)}$, and the pressure drop across the duct is equal to

$$\Delta P_d = g\rho_2 \Delta h_2 \,.$$ (8)

The absorber plate area ($A_p$) in Eq. (2) is different for the one-side and three-side rugged SAHs. It is equivalent to the top absorber plate area for the one-side rugged collector, whereas, it is the sum of the top collector area and two-side collector area for the three-side roughened solar air heater.

On the basis of error exploration carried out for different instruments used in measurement [13, 34], the uncertainties in the determination of several quantities are specified below:

1) the Reynolds number: $\pm 1.04\%$,

2) the Nusselt number: $\pm 2.57\%$,

3) the friction factor: $\pm 2.26\%$.

## 4   Validity test

For validation purposes, the Nusselt number ($\mathrm{Nu}_r$) and friction factor ($f_r$) were determined from testing on a multiple-v one-side rugged SAH duct with a fixed value of relative roughness pitch, $P/e = 10$, relative roughness height, $e/D_h = 0.042$, relative roughness width, $W/w = 6$, and angle of attack, $\alpha = 60°$. The respective results of the one-side roughened solar air heater were compared with results obtained from the correlations developed

by Hans *et al.* [30]. For the Nusselt number and friction factor the following expressions were used:

$$\mathrm{Nu}_r = 3.35 \times 10^{-5} \mathrm{Re}^{0.92} \left(\frac{e}{D_h}\right)^{0.77} \left(\frac{W}{w}\right)^{0.43} \left(\frac{\alpha}{90}\right)^{-0.49}$$
$$\times \exp\left[-0.61\ln^2\left(\frac{\alpha}{90}\right)\right] \exp\left[-0.1177\ln^2\left(\frac{W}{w}\right)\right]\left(\frac{P}{e}\right)^{8.54}$$
$$\times \exp\left[-2.0407\ln^2\left(\frac{P}{e}\right)\right], \tag{9}$$

$$f_r = 4.47 \times 10^{-4} \mathrm{Re}^{-0.3188} \left(\frac{e}{D_h}\right)^{0.73} \left(\frac{W}{w}\right)^{0.22} \left(\frac{\alpha}{90}\right)^{-0.39}$$
$$\times \exp\left[-0.52\ln^2\left(\frac{\alpha}{90}\right)\right] \exp\left[-2.133\ln^2\left(\frac{P}{e}\right)\right]\left(\frac{P}{e}\right)^{8.9}. \tag{10}$$

The comparison of values of ($\mathrm{Nu}_r$) and ($f_r$) obtained from the present experimental work and the work of Hans *et al.* [30] is illustrated in Figs. 11 and 12, respectively. The discrepancy of the obtained experimental values for ($\mathrm{Nu}_r$) is $\pm 2.3\%$ with respect to the theoretical values given in Eq. (9). At the same time, the discrepancy of the obtained experimental values for the friction factor is $\pm 2.27\%$ from the theoretical values given by Eq. (10). This illustrates a good agreement between experimental and theoretical
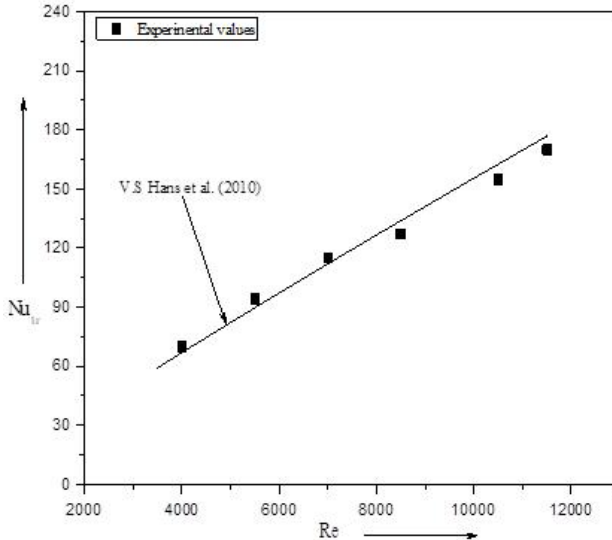


Figure 11: Nusselt number validation.

values, which certifies the correctness of performance of the composed experimental set-up.
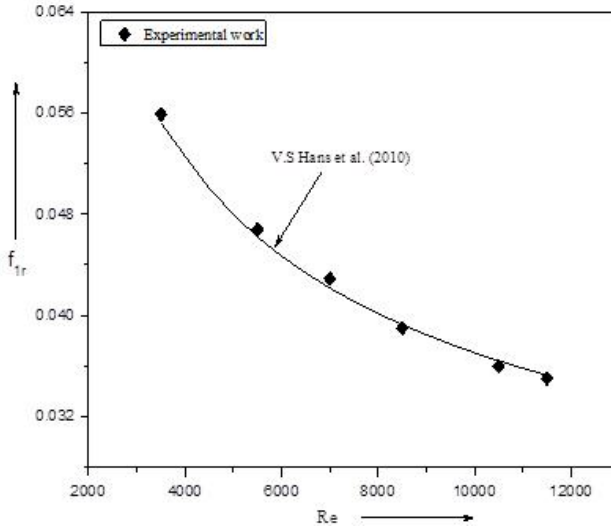


Figure 12: Friction factor validation.

# 5   Results and discussion

The heat transfer and friction characteristics of the three-side roughened rectangular duct SAH with the combination of multiple-v and transverse wire (top wall multi-v and two side walls transverse), computed on the basis of experimental data gathered for several flow and roughness restrictions are  discussed below. These results are compared with those achieved for the case of one-side rugged duct SAH having fixed values of relative roughness pitch, $P/e = 10$, relative roughness height, $e/D_h = 0.042$, angle of attack, $\alpha = 60°$, and relative roughness width, $W/w = 6$, working under parallel circumstances. Figure 13 illustrates the intensity of solar emission and ambient air temperature during a specific day. Figure 14 displays the variation of the plate and air temperature in three-side and one-side roughened SAHs, associated with the variation of the fluid inlet temperature and solar emission. As might be realised from Fig. 13, the ambient temperature changes slowly with time whereas the intensity of solar emission rises up to 11:30 a.m., then decreases abruptly. Figure 14 indicates that both the

plate and air temperature are greater in the three-side roughened collector as related to the one-side roughened collector. Figure 15 displays the change of the mean plate and fluid temperature with the intensity of solar emission. Again both parameters are greater in the three-side roughened SAH as compared to the one-side roughened SAH.
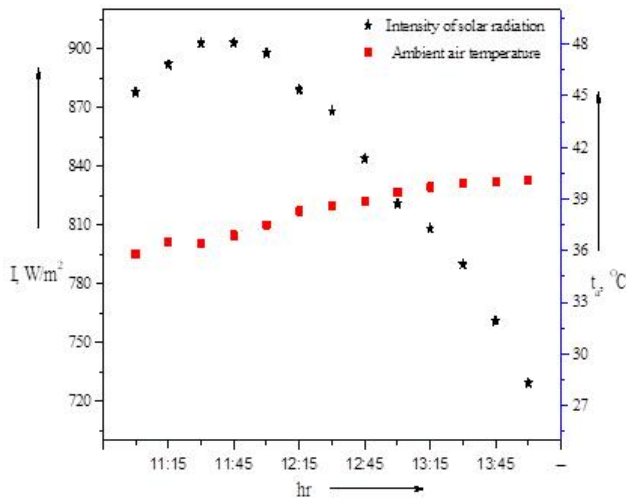


Figure 13: Intensity of solar emission and ambient air temperature during a specific day.
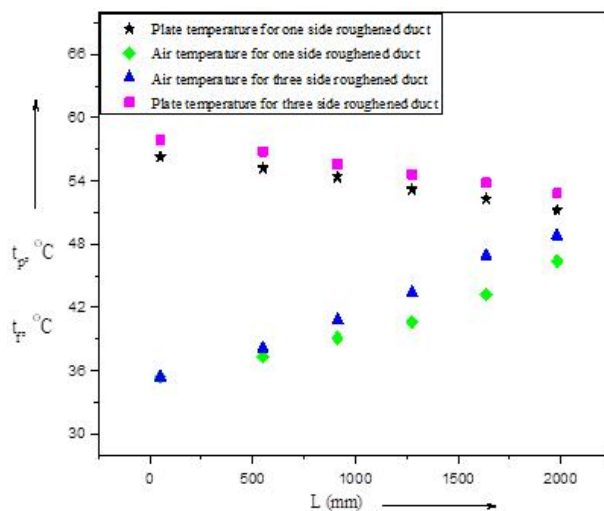


Figure 14: Plate and fluid temperature.
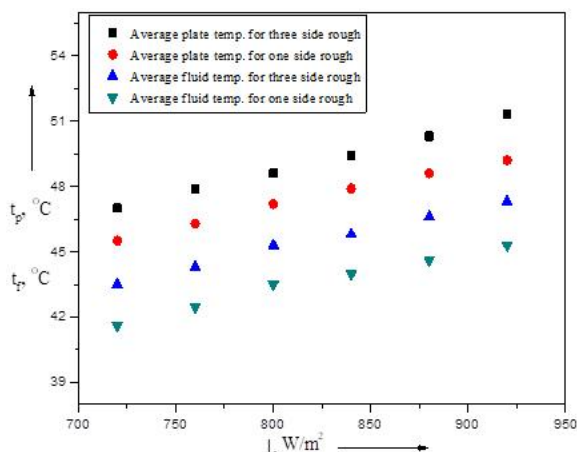
Figure 15: Average plate and fluid temperature.

## 5.1 Comparison of heat transfer and friction factor data

Figure 16 exhibits the comparison of the relevant Nusselt numbers for the one-side and three-side rugged duct SAHs obtained during the present experimental work and those of Hans *et al.* [30]. The evaluation of heat transfer data made for given values of relative roughness pitch, $P/e = 10$, relative roughness height, $e/D_h = 0.042$, angle of attack, $\alpha = 60°$, and fixed value of $W/w = 6$, for the stream Reynolds number Re $= 3500$–$12\,000$. The ex-
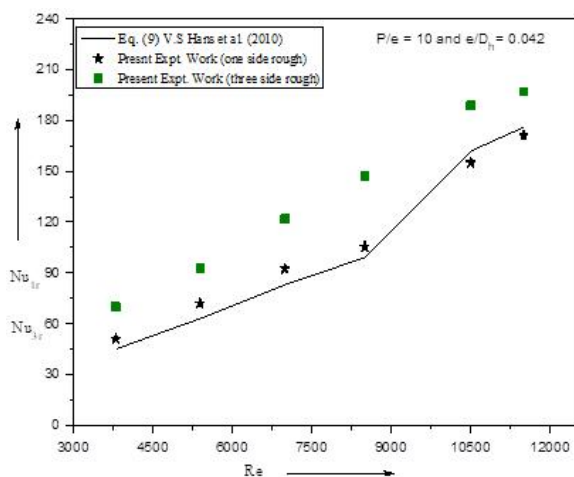
Figure 16: Comparison of $\mathrm{Nu}_r$ data for $e/D_h = 0.042$.

perimental values of $Nu_r$ in the three-side rugged SAH are greater with respect to the one-side rugged SAH. In the same way, Fig. 17 illustrates the change of heat transfer characteristics for given values of $P/e = 10$ and $e/D_h = 0.034$, showing a similar trend with the increasing Reynolds number.
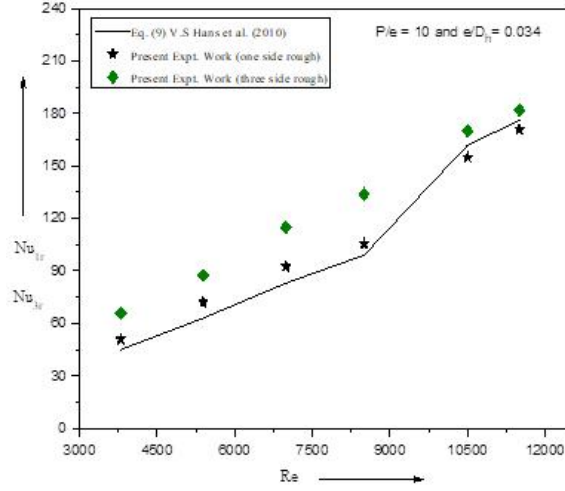


Figure 17: Comparison of $Nu_r$ data for $e/D_h = 0.034$.

Figures 18 and 19 show the assessment of the friction factor for the three-side roughened solar air heater and one-side roughened solar air heater
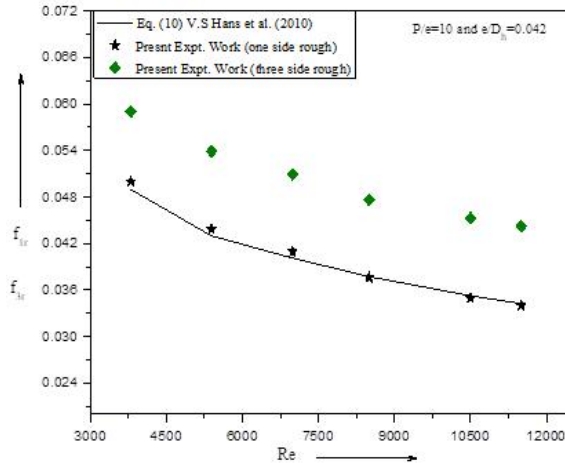


Figure 18: Comparison of $f_r$ data for $e/D_h = 0.042$.

obtained during the present experimental work and a comparison with the results of Hans *et al.* [30]. As can be seen, the three-side solar air heater is characterized by a greater value of friction factor as compared to the one-side roughened solar air heater. The friction factor is also found to increase with the increasing value of relative roughness height.
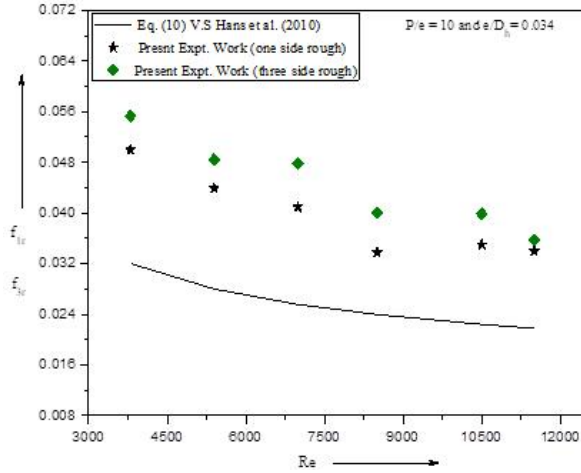


Figure 19: Comparison of $f_r$ data for $e/D_h = 0.034$.

## 5.2    Other Nusselt number and friction factor data

Figures 20 and 21 are presented to realise the influence of roughness and flow restrictions on heat transfer intensification in the three-side roughened SAH as compared to the one-side roughened SAH. Figure 20 illustrates the impact of relative roughness pitch, $P/e$, on the Nusselt number, $Nu_{3r}$, for the three-side rugged collector and $Nu_{1r}$ for the one-side rugged collector, for given values of relative roughness height, $e/D_h = 0.042$, and angle of attack, $\alpha = 60°$, within a range of Reynolds numbers. Figure 21 exhibits the effect of relative roughness height, $e/D_h$, on $Nu_{3r}$ for the three-side roughened collector and $Nu_{1r}$ for the one-side roughened collector, for a given value of relative roughness pitch, $P/e = 10$, and angle of attack, $\alpha = 60°$, within the investigated range of Reynolds numbers. The Nusselt number $Nu_{3r}$ for the three-side roughened collector is increased by an extent of 24–76% over that of $Nu_{1r}$ for the one-side roughened collector.

Figures 22 and 23 illustrate the effect of flow restrictions on friction factor in the three-side roughened and one-side roughened SAHs. Figure 22
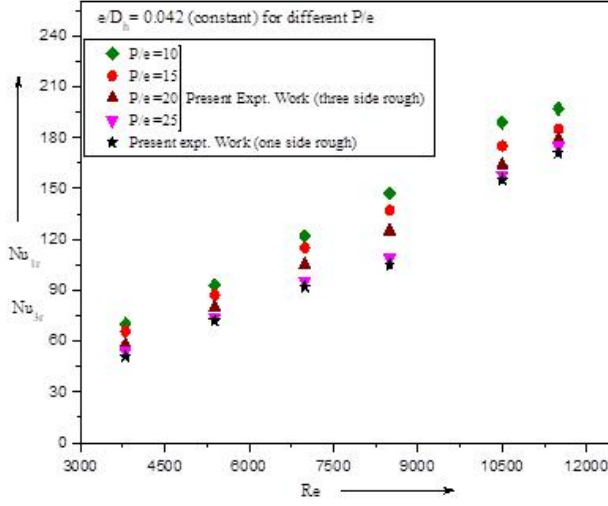
Figure 20: Effect of $P/e$ on $\mathrm{Nu}_{1r}$ in three-side roughened SAHs.
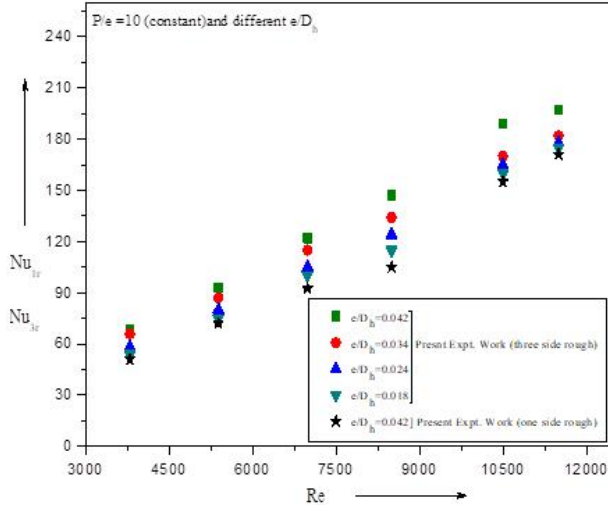


Figure 21: Effect of $e/D_h$ on $\mathrm{Nu}_r$ in three-side rugged SAHs.

exhibits the impact of relative roughness pitch, $P/e$, on the friction factor $f_{3r}$ for the three-side roughened collector and $f_{1r}$ for the one-side roughened collector, for given values of relative roughness height, $e/D_h = 0.042$, and angle of attack, $\alpha = 60°$, for a given range of Reynolds numbers. Figure 23 illustrates the effect of relative roughness height, $e/D_h$, on the friction factor

$f_{3r}$ for the three-side roughened collector and $f_{1r}$ for the one-side roughened collector, for given values of relative roughness pitch, $P/e = 10$, and angle of attack, $\alpha = 60°$, for a given range of Reynolds numbers. The values of friction factor $f_{3r}$ in the three-side roughened collector exceed by 4–36% those of $f_{1r}$ for the one-side roughened collector.
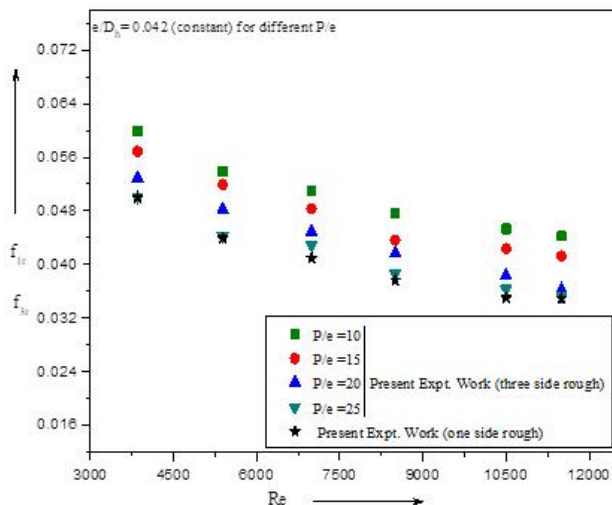


Figure 22: Effect of $P/e$ on $f_r$ in three-side roughened SAHs.
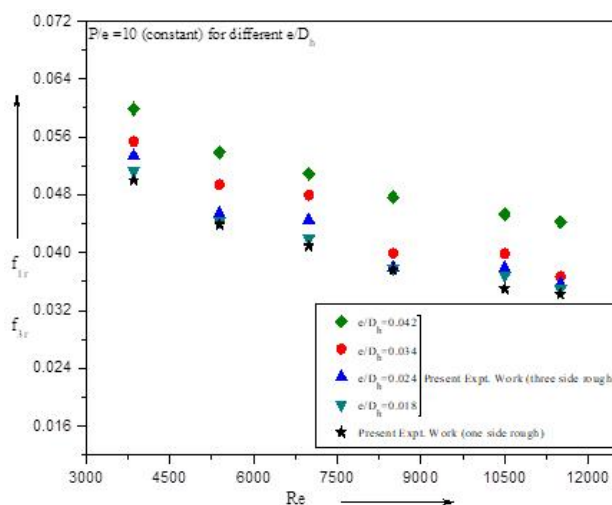


Figure 23: Effect of $e/D_h$ on $f_r$ in three-side roughened SAHs.

## 5.3   Heat transfer enhancement

The heat transfer coefficient in the three-side artificially roughened SAH is greater as compared to the one-side roughened SAH. Figure 24 illustrates the heat transfer enhancement ratio, $(Q_{3r}/Q_{1r})$, versus the intensity of solar radiation, at varying values of Re, for a fixed angle of attack, $\alpha = 60°$. The following equations have been adopted for $Q_{3r}$ and $Q_{1r}$:

$$Q_{3r} = h_{3r}A_{p3r}\Delta t_3 \,, \tag{11}$$

$$Q_{1r} = h_{1r}A_{p1r}\Delta t_1 \,. \tag{12}$$

It might be realised that the heat transfer enhancement ratio increases with the rising value of Reynolds number and the increasing intensity of solar emission. The three-side roughened SAHs are thermally superior over the one-side roughened SAHs; their performance is also boosted at larger Reynolds numbers and larger intensities of solar radiation.
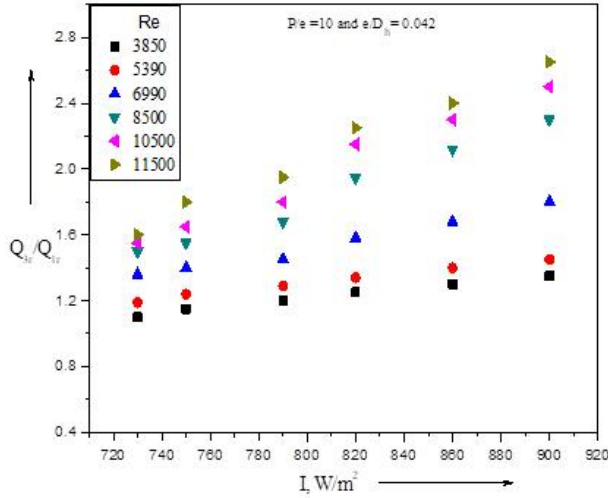


Figure 24: Heat transfer enhancement ratio.

# 6   Conclusions

Based on the experimental exploration of heat transfer and friction factor in the three-side artificially roughened rectangular duct SAHs with an arrangement of multiple-v (top wall multi-v and two side walls transverse), the following conclusions can be drawn:

- The value of Nusselt number increases whereas the friction factor drops as the Reynolds number increases.

- The Nusselt number and friction factor increase with the increasing value of relative roughness height ($e/D_h$) and decreases with the increasing value of relative roughness pitch ($P/e$).

- The Nusselt number and friction factor in three-side artificially roughened SAHs are increased by 24–76% and 4–36%, respectively, over those of one-side roughened SAHs for similar operating conditions.

- The maximum value of heat transfer enrichment ratio for the three-side roughened SAH with respect to the one-side roughened SAH is found to be 2.80.

- Three-side artificially rugged SAHs are superior as compared to one-side artificially roughened SAHs qualitatively and quantitatively.

# References

[1] Bhatti M.S., Shah R.K.: *Turbulent and Transition Flow Convective Heat Transfer Handbook of Single Phase Convective Heat Transfer*. Wiley, New York 1987.

[2] Garg H.P., Prakash J.: *Solar Energy Fundamentals and Applications* (1st Edn.). Tata McGraw-Hill, New Delhi 2000.

[3] Kumar D., Prasad L.: *Performance analysis of three side's solar air heater having roughness elements as a combination of multiple-v and transverse wire on the absorber plate.* Arch. Thermodyn. **41**(2020), 3, 125–146.

[4] Al-Joboory H.N.S.: *Experimental and theoretical investigation of an evacuated tube solar water heater incorporating wickless heat pipes.* Arch. Thermodyn. **41** (2020), 3, 3–31.

[5] Menni Y., Chamkha A.J., Zidani C., Benyoucef B.: *Analysis of thermo-hydraulic performance of a solar air heater tube with modern obstacles.* Arch. Thermodyn. **41**(2020), 3, 33–56.

[6] Kumar V.: *Augmentation in heat transfer and friction of three sides over one side dimple roughened solar duct.* Arch. Thermodyn. **41**(2020), 3, 57–89.

[7] Sahu M.K., Matheswaran M.M., Bishnoi P.: *Experimental investigation of augmented thermal and performance characteristics of solar air heater ducts due to varied orientations of roughness geometry on the absorber plate.* Arch. Thermodyn. **41**(2020), 3, 147–182.

[8]  Ghritlahre H.K., Sahu P.K.: *A comprehensive review on energy and exergy analysis of solar air heaters*. Arch. Thermodyn. **41**(2020), 3, 183–222.

[9]  Ghritlahre H.K., Chandrakar P., Ahmad A.: *Solar air heater performance prediction using artificial neural network technique with relevant input variables*. Arch. Thermodyn. **41**(2020), 3, 255–282.

[10] Ghritlahre H.K.: *An experimental study of solar air heater using arc shaped wire rib roughness based on energy and exergy analysis*. Arch. Thermodyn. **41**(2021), 3, 115–139.

[11] Kumar V., Prasad L.: *Thermal performance investigation of three side's concave dimple roughened solar air heaters*. Sol. Energy **188**(2019), 361–379.

[12] Kumar D., Prasad L.: *Analysis on optimal thermohydraulic performance of solar air heater having multiple V-shaped wire rib roughness on absorber plate*. Int. Energy J. **18**(2018), 153–170.

[13] Holman J.P.: *Experimental Method for Engineers*. McGraw-Hill, New York 2007.

[14] Prasad B.N.: *Thermal performance of artificially roughened solar air heaters*. Sol. Energy **91**(2013), 59–67.

[15] Prasad B.N., Saini J.S.: *Effect of artificial roughness on heat transfer and friction factor in a solar air heater*. Sol. Energy **41**(1988), 6, 555–60.

[16] Kumar D., Prasad L.: *Heat transfer augmentation of various roughness geometry used in solar air heaters*. Int. J. Mech. Eng. Technol. **12**(2017), 8, 491–508.

[17] Zidani C., Benyoucef B., Didi F., Guendouz, N.: *Simulation and numerical analysis of a rectangular pipe with transversal baffle – comparison between zigzag and plane baffles*. Arch. Thermodyn. **41**(2020), 4, 269–283.

[18] Kumar D., Prasad L.: *Thermo-hydraulic performance of solar air heater having multiple V-shape rib on absorber plates*. Carbon-Sci. Tech. **10**(2018), 1, 39–50.

[19] Daghsen K., Lounissi, D., Bouaziz, N.: *A universal model for solar radiation exergy accounting: Case study of Tunisia*. Arch. Thermodyn. **43**(2022), 2, 97–118.

[20] Kumar A., Layek A.: *Energetic and exergetic performance evaluation of solar air heater with twisted rib roughness on absorber plate*. J. Clean. Prod. **232** (2019), 617–628.

[21] Behura A.K., Prasad B.N., Prasad L.: *Heat transfer friction factor and thermal performance of three sides artificially roughened solar air heaters*. Sol. Energy **130**(2016), 46–59.

[22] Karwa R., Chitoshiya G.: *Performance study of solar air heater having v-down discrete ribs on absorber plate*. Energy **55**(2013), 939–955.

[23] Kumar A., Saini R.P., Saini J.S.: *Development of correlations for Nusselt number and friction factor for solar air heater with roughened duct having multi v-shaped with gap ribs as artificial roughness*. Renew. Energ. **58**(2013), 151–163.

[24] Maithani R., Saini J.S.: *Heat transfer and friction factor correlations for a solar air heater duct artificially with v-ribs with symmetrical gaps*. Exp. Therm. Fluid Sci. **70**(2016), 220–227.

[25] Gupta D., Solanki S.C., Saini J.S.: *Thermohydraulic performance of solar air heaters with roughened absorber plates*. Sol. Energy **61**(2000), 33–42.

[26] Deo N.S., Chander S., Saini J.S.: *Performance analysis of solar air heater duct roughened with multigap V-down ribs combined with staggered ribs*. Renew. Energ. **91**(2016), 484–500.

[27] Prasad B.N., Behura A.K., Prasad L.: *Fluid flow and heat transfer analysis for heat transfer enhancement in three sided artificially roughened solar air heater*. Sol. Energy **105**(2014), 27–35.

[28] Singh S., Chander S., Saini J.S.: *Thermal and effective efficiency based analysis of discrete V down rib roughened solar air heaters*. J. Renew. Sust. Energ. **3**(2011), 023107–023126.

[29] American Society of Heating, Refrigerating and Air-Conditioning Engineers: *Method of Testing to Determine the thermal performance of solar collectors* (ASHRAE Standard 93-97). New York 1977.

[30] Hans V.S., Saini R.P., Saini J.S.: *Heat transfer and friction factor correlations for a solar air heater duct roughened artificially with multiple v-ribs*. Sol. Energy **84**(2010), 898–911.

[31] Kumar A., Saini R.P., Saini J.S.: *Experimental Investigation on heat transfer and fluid flow characteristics of air flow in a rectangular duct with multi v-shaped rib with gap roughness on the heated plate*. Sol. Energy **86**(2012), 1733–1749.

[32] Aharwal K.R., Gandhi B.K., Saini J.S.: *Experimental investigation on heat transfer enhancement due to a gap in an inclined continuous rib arrangement in a rectangular duct of solar air heater*. Renew. Energ. **33**(2008), 585–596.

[33] Momin A.M.E., Saini J.S, Solanki S.C.: *Heat transfer and friction in solar air heater duct with v-shaped rib roughness on absorber plate*. Int. J. Heat Mass Tran. **45**(2002), 3383–3396.

[34] Kline S.J., Mcclintok F.A.: *Describing uncertainties in single sample experiment*. Mech. Eng. **75**(1953), 1, 3–8.

# New environmentally friendly low-pressure refrigerants mini-channel

**MAŁGORZATA SIKORA**[*]
**TADEUSZ BOHDAL**

Koszalin University of Technology, Śniadeckich 2, 75-453 Koszalin, Poland

**Abstract** Nowadays, in addition to the thermodynamic properties of refrigerants, their impact on the environment is of high significance. Hence, it is important to use refrigerants with the lowest possible values of ozone depletion potential and global warming potential indices in refrigeration, organic Rankine cycle (ORC), air conditioning, and heat pump systems. Natural refrigerants are the most environmentally friendly; unfortunately, they have less favourable thermodynamic properties. Currently, low-pressure refrigerants from the FC (fluorocarbons, fluorine liquids) and HFE (hydrofluoroether) groups are increasingly used. This paper presents the most important properties and applications of selected refrigerants from these groups and also reviews the literature on their use.

**Keywords:** Refrigerants; Global warming potential; Ozone depletion potential; Fluorinert liquid; Hydrofluoroether

## Nomenclature

| | | |
|---|---|---|
| $c_p$ | – | specific heat |
| $D$ | – | diameter |
| $G$ | – | mass flux density |
| GWP | – | global warming potential |

---

[*]Corresponding Author. Email: malgorzata.sikora@tu.koszalin.pl

| $d_h$ | – | hydraulic diameter |
| $L$ | – | length of the channel |
| $m_c,\ m_r$ | – | mass flux of coolant and refrigerant |
| ODP | – | ozone depletion potential |
| $q$ | – | flux density |
| $t$ | – | temperature |
| $t_s$ | – | saturation temperature |
| $x$ | – | coordinate along the channel |

**Greek symbols**

| $\alpha$ | – | heat transfer coefficient |
| $\eta$ | – | kinematic viscosity |
| $\mu$ | – | dynamic viscosity |
| $\lambda$ | – | heat conductivity |
| $\sigma$ | – | surface tension |
| $\rho$ | – | density |
| $\varphi$ | – | void fraction |

**Subscripts**

| $l$ | – | liquid phase |
| $v$ | – | vapor phase |

**Acronyms**

| CFC | – | chlorofluorocarbon |
| FC | – | fluorocarbon |
| HCFC | – | hydrochlorofluorocarbon |
| HFE | – | hydrofluoroether |
| ORC | – | organic Rankine cycle |
| PFC | – | perfluorocarbons |

# 1   Introduction

The current state of the environment causes increasing pressure on all industries to minimize the harmful effects of human activities. This includes the refrigeration, air conditioning, and heat pump industries in the broadest sense. The primary indicators describing the environmental impact of a refrigerant are ozone depletion potential (ODP) and global warming potential (GWP). ODP is a measure of the destructive effect of a substance on the ozone layer. This index was referred to as Freon R11, for which ODP = 1. ODP values for individual substances are published in the Montreal Protocol (Annex E of PN–EN 378-1). The GWP index, on the other hand, is the greenhouse effect potential, i.e., it compares how much heat

is retained by a certain mass of a gas in relation to the amount of heat retained by the same mass of carbon dioxide ($CO_2$).

As of 2022 year, the GWP index for refrigerants used in new refrigeration/air conditioning systems should be below 150, except for first-stage refrigeration circuits in cascade systems, where it can be up to 1500. Accordingly, work is underway on substances that meet these requirements and are suitable for refrigeration applications. Research is also carried out on the use of low-pressure substances from the fluorocarbons (FCs) and hydrofluoroethers (HFEs) groups sold by 3M Company for this purpose. These are primarily degreasing, foaming, or fire-extinguishing substances with relatively good thermal properties. Some of them are already used in the electronics industry. Table 1 shows the most important properties of substances from the HFE group (liquids sold commercially by the 3M Company as Novec-engineered fluid), and Table 2 shows those of substances from the FC group.

Table 1: Thermodynamic properties of hydrofluoroether group substances at atmospheric pressure and 20°C [1].

| Property | Unit | Novec 7000 | Novec 7100 | Novec 7200 | Novec 7300 | Novec 7500 | Novec 7600 | Novec 649 |
|---|---|---|---|---|---|---|---|---|
| Boiling point | °C | 34 | 61 | 76 | 98 | 128 | 131 | 49 |
| Molar mass | g/mol | 200 | 250 | 264 | 350 | 414 | 346 | 316 |
| Critical temperature | °C | 165 | 195 | 210 | 243 | 261 | 260 | 169 |
| Critical pressure | MPa | 2.48 | 2.23 | 2,01 | 1.88 | 1.55 | 1.67 | 1.88 |
| Evaporation heat | kJ/kg | 142 | 112 | 119 | 102 | 89 | 116 | 88 |
| Liquid density | kg/m$^3$ | 1400 | 1510 | 1420 | 1660 | 1614 | 1540 | 1600 |
| Kinematic viscosity coefficient | mm$^2$/s | 0.32 | 0.38 | 0.41 | 0.71 | 0.77 | 1.1 | 0.4 |
| Specific heat | J/(kgK) | 1300 | 1183 | 1220 | 1140 | 1128 | 1319 | 1103 |
| Heat conductivity | W/(mK) | 0.075 | 0.069 | 0.068 | 0.063 | 0.065 | 0.071 | 0.059 |
| Surface tension | mN/m | 12.4 | 13.6 | 13.6 | 15 | 16.2 | 17.7 | 10,8 |
| GWP | | 420 | 297 | 59 | 210 | 100 | 700 | 1 |

Table 2: Thermodynamic properties of FC group substances (fluorinert liquids) at atmospheric pressure and 20°C [1].

| Property | Unit | FC-3284 | FC-72 | FC-84 | FC-770 | FC-3283 | FC-40 | FC-43 |
|---|---|---|---|---|---|---|---|---|
| Boiling point | °C | 50 | 56 | 80 | 95 | 128 | 155 | 174 |
| Molar mass | g/mol | 299 | 338 | 388 | 399 | 521 | 650 | 670 |
| Critical temperature | °C | 161 | 176 | 202 | 238 | 235 | 270 | 294 |
| Critical pressure | MPa | 1.94 | 1.83 | 1.75 | 2.47 | 1.22 | 1.18 | 1.13 |
| Evaporation heat | kJ/kg | 105 | 88 | 90 | 86 | 78 | 68 | 70 |
| Liquid density | kg/m$^3$ | 1710 | 1680 | 1730 | 1793 | 1820 | 1850 | 1860 |
| Kinematic viscosity coefficient | mm$^2$/s | 0.42 | 0.38 | 0.53 | 0.79 | 0.75 | 1.8 | 2.5 |
| Specific heat | J/(kgK) | 1100 | 1100 | 1100 | 1038 | 1100 | 1100 | 1100 |
| Heat conductivity | W/(mK) | 0.062 | 0.057 | 0.060 | 0.063 | 0.066 | 0.065 | 0.065 |
| Surface tension | mN/m | 13 | 10 | 12 | 15 | 15 | 16 | 16 |

# 2 Properties of low-pressure refrigerants

HFE and FC group technical fluids are substances that can be used in heat transfer issues with an emphasis on cooling. This is related to their thermal properties. Since there is insufficient information on the thermophysical properties of HFE group refrigerants, many chemists investigate them in relation to the saturation temperature. Muñoz-Rujas *et al.* [2] conducted a study of the thermophysical properties of the HFE7200 refrigerant in the temperature range of 20–60°C. Zheng *et al.* [3] conducted similar studies in the temperature range of –27.53–80.46°C for the HFE7200 and HFE7500 refrigerants. Table 3 shows a comparison of the thermal properties of HFE7000, HFE7100, water, and R134a refrigerant.

Raush *et al.* [5] carried out tests of density, liquid kinematic viscosity coefficient, and surface tension of HFEs, depending on the saturation temperature. They performed density tests for different saturation temperatures using a vibrating densimeter with a measurement error of about

Table 3: Characteristic properties of HFE7100, HFE7000, water, and R134a refrigerants at normal pressure [4].

| Property | Refrigerant | | | |
|---|---|---|---|---|
| | HFE7100 | HFE7000 | Water | R134a |
| Flash-point | – | – | non-flammable | non-flammable |
| Toxicity | low | low | – | – |
| ODP | 0 | 0 | 0 | 0 |
| GWP | 320 | 530 | 0 | 1300 |
| Freezing point, °C | −135 | −122.5 | 0 | −96.7 |
| Boiling point, °C | 61 | 34 | 99.98 | −26.074 |
| Critical temperature, °C | 195.3 | 165 | 373.94 | 101.06 |
| Critical pressure, MPa | 2.23 | 2.48 | 22.06 | 4.0593 |

0.02%. The liquid-phase kinematic viscosity and surface tension were determined by surface light scattering measurements in the temperature range of 0–100°C with relative measurement uncertainties of 2% and 1.5%, respectively [5]. Figure 1 shows the dependence of the quantities presented in the aforementioned paper on the saturation temperature.

Awareness of the environmental impact of greenhouse gas emissions has led to a search for alternatives to chlorofluorocarbons (CFCs), hydrochlorofluorocarbons (HCFCs), and perfluorocarbons (PFCs) refrigerants that will not exhibit undesirable environmental effects. Since HFE fluids have become a good alternative to old refrigerants (including FC group fluids), it is important to understand their thermophysical properties, which describe their suitability for heat transfer, in both single-phase and two-phase processes. Figure 2 shows the specific heat and thermal conductivity of the liquid phase of selected HFE and FC group substances, while Fig. 3 shows the same for the gas phase. As can be seen, the most favourable heat capacity is that of Novec 649, in terms of both liquid and gas phases, while the lowest heat capacity is that of FC72.

In terms of thermal conductivity, the HFE7100 refrigerant shows the most favourable properties, and FC72 has the lowest ones. As can be seen, in addition to environmental aspects, HFE group refrigerants have an advantage over FC group refrigerants in terms of thermal properties. Novec 649 (fluorinated ketone, $C_2F_5C(O)CF(CF_3)_2$) is currently being considered an environmentally friendly alternative for cooling electronics due to its high
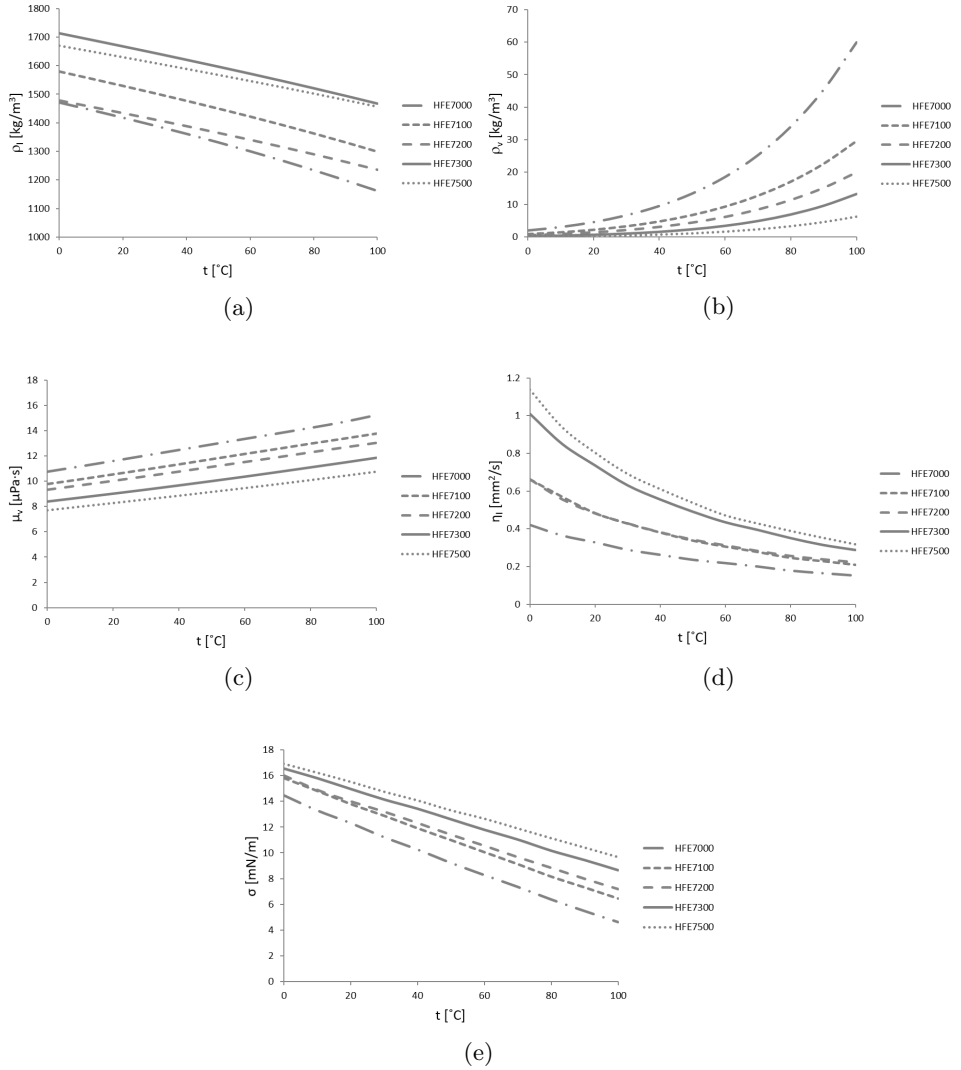
Figure 1: Properties of hydrofluoroether group fluids studied by Rausch *et al.* [5].

dielectric strength and low GWP. It exhibits very low toxicity with long-term stability. Forrest *et al.* [12] conducted a study of this refrigerant boiling in volume in order to cool a nickel resistance wire at a saturation temperature of 49°C. The heat transfer coefficient for Novec 649 is higher than for FC72 under the same conditions. Thus, Novec 649 is considered an alternative to FC72 refrigerant for immersion cooling of electronics.
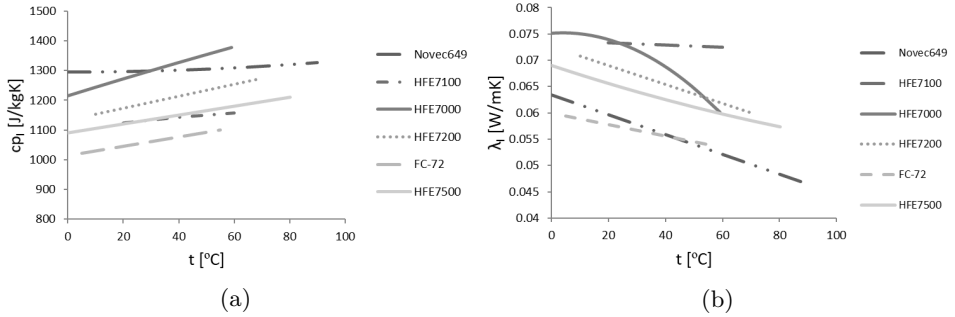
Figure 2: Thermal properties of the liquid phase of selected hydrofluoroether and FC fluids [1, 6–11].
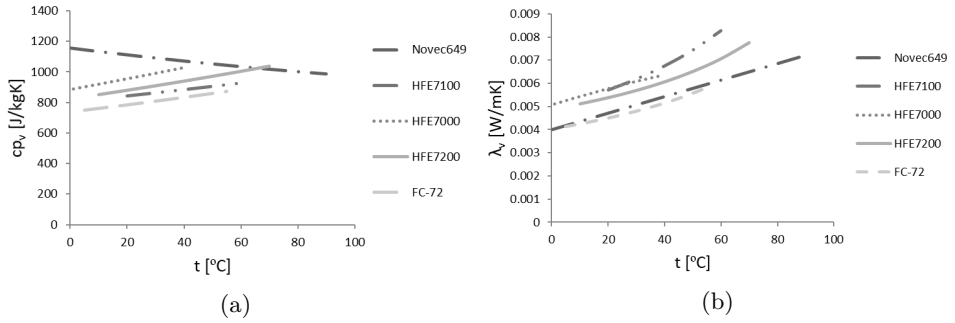


Figure 3: Thermal properties of the gas phase of selected hydrofluoroether and FC fluids [1, 6–11].

# 3 Application of low-pressure refrigerants in scientific research

In the literature, the use of low-pressure refrigerants in the heat exchange process is increasingly observed, including the use of phase transformations. Bonk *et al.* [13] described an organic Rankine cycle (ORC) microsystem they designed for teaching and research purposes. The goal of this research was to propose a safe and environmentally friendly microscale heat engine.

An organic fluid called 3M Novec 649 was used as the working medium in this system. The tested system had an output of 1 kW, and the supply temperature was 140°C. The authors studied the effect of the circuit parameters on its efficiency using the mentioned working medium [13]. Bruder *et al.* [14, 15], on the other hand, conducted a study of the boiling process of this medium in a vertical copper channel. They conducted studies of the

temperature distribution on the surface of the channel wall for different flow rates of the medium and performed temperature and heat flux studies using a fibre optic probe and thermocouples. The same authors also presented the results of a study of the boiling process in a 40 mm × 40 mm rectangular channel at a mass flux density of 1000 kg/m²s [15]. The study was conducted from single-phase convection to fully developed boiling. Fu and Lin, on the other hand, conducted a study of the effects of mass flow rate, system pressure, and vertical mini-channel diameter on the supercritical heat transfer characteristics of the Novec 649 medium. Experimental results showed that the heat transfer coefficient increases significantly with increasing mass flux, especially for small channel diameters. An increase in mass flux can also result in a smaller decrease in the heat transfer coefficient when the pseudocritical temperature is reached. The heat transfer coefficient decreases sharply when the fluid temperature reaches the pseudocritical temperature and then increases again when the fluid temperature exceeds the pseudocritical temperature. The authors developed an empirical correlation for Novec 649 working fluid to describe the heat transfer

$$\mathrm{Nu} = 3.37 \times 10^3 \mathrm{Re}^{0.47} \mathrm{Pr}^{1.05} \left(\frac{\overline{C}_p}{C_{pw}}\right)^{0.91} \left(\frac{\mathrm{Gr}}{\mathrm{Re}^2}\right)^{-0.36} \left(\frac{D}{L}\right)^{2.16}, \quad (1)$$

where $\overline{C}_p/C_{pw}$ is the dimensionless specific heat capacity ($C_{pw}$ – specific heat in wall temperature), Nu is the Nusselt number, Re is the Reynolds number, Pr is the Prandtl number, and Gr is the Grashof number, $D$ and $L$ denotes the diameter and length, respectively. Equation (1) was developed based on the Jackson method. The deviation of the calculated results according to the correlation from the experimental results is about 20%, and the average absolute error is only 11.4% [16].

Cao *et al.* [17] conducted boiling studies in a volume of HFE7200 medium using nanoparticles. They studied the effect of nanoparticle surface on heat transfer and found that its shape could increase the heat transfer coefficient and critical heat flux by up to 60%. In addition, mathematical modelling was successfully carried out using Zuber's hydrodynamic instability model. Cao *et al.* conducted boiling investigations of a few HFE refrigerants [18,19].

Adebayo *et al.* [20] investigated the use of HFE7000 and HFE7100 refrigerants in cascade systems in combination with $CO_2$. The use of $CO_2$ in refrigeration and heat pump systems is also now widely discussed in the literature. Mikielewicz and Andrzejczyk [21–23] conducted condensation studies of HFE7000 and HFE7100 refrigerants in mini-channels. They

focused on issues of flow resistance in the condensation process in a pipe channel with an internal diameter of 2.3 mm. They studied the effects of heat flux, fluid flow rate, vapour quality, and saturation temperature on flow resistance. The experimental results were compared with correlations of other authors, and the best fit of the results with the model of Fronk and Garimelli [24] was found [25]. Bohdal and Sikora [26–29] conducted similar studies of the condensation process of Novec 649, HFE7000, and HFE7100 working fluids in single tubular mini-channels with diameters in the range of 2.0–0.5 mm. In addition to heat transfer and flow resistance studies, the authors conducted a flow structure study [27]. Figure 4 shows a comparison of the results of the two teams. Figure 5 shows an example of the results of flow structures during the condensation of the HFE7000 refrigerant in a mini-channel pipe with an internal diameter of 0.8 mm. Al-Zaidi *et al.* [30] also studied the flow structures formed during the condensation of the HFE7100 refrigerant; however, they used multiports made of rectangular mini-channels with hydraulic diameter $d_h = 0.57$ mm, saturation temperature $t_s = 60°$C, and mass flux density $G = 48-126$ kg/m$^2$s.
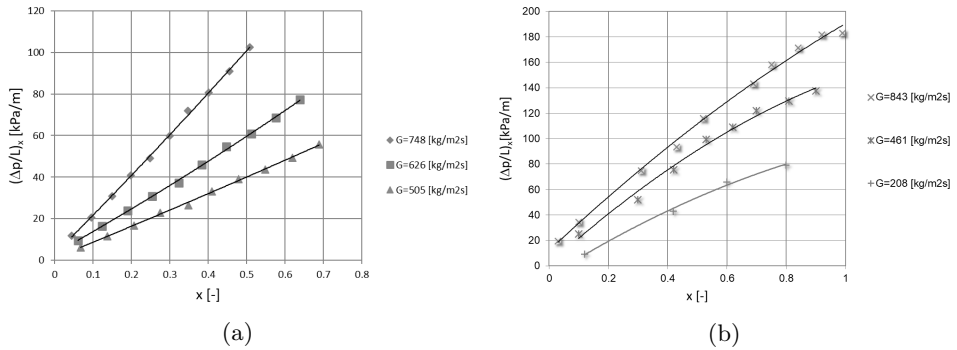


Figure 4: Dependence of flow resistance in the condensation process of HFE7000 refrigerant in a mini-channel according to: a) Mikielewicz, Andrzejczyk [21] for $d_h = 2.3$ mm and $t_s = 52°$C; b) Sikora, Bohdal and Formela [27] for $d_h = 2.0$ mm and $t_s = 46°$C.

Pastuszko *et al.* [4] conducted a study on the effect of surface microdevelopment on heat transfer. They investigated the boiling process of water, ethanol, Novec 649, and FC72 at atmospheric pressure to select such parameters of the developed surface to obtain the highest possible heat transfer coefficient. Three types of structural surfaces were used: smooth microribs with a height of 1.0 mm (designated MF), reinforced surfaces made by sintering micro-rib tips with perforated copper foil (MF+F), and structural
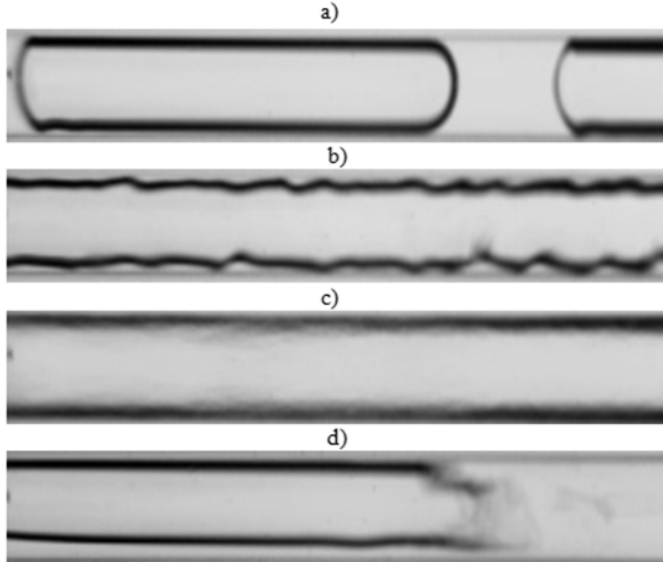
Figure 5: Results of flow structures obtained by Sikora [31] during condensation of HFE7000 refrigerant in a pipe mini-channel with an inner diameter $d_h = 0.8$ mm: a) plug structure $G = 197$ kg/m$^2$s, $x = 0.004$, $\varphi = 0.44$, $t_s = 31^\circ$C; b) annular-wave structure $G = 369$ kg/m$^2$s, $x = 0.012$, $\varphi = 0.69$, $t_s = 32.5^\circ$C; c) annular structure $G = 491$ kg/m$^2$s, $x = 0.032$, $\varphi = 0.82$, $t_s = 41^\circ$C; d) slug structure $G = 639$ kg/m$^2$s, $x = 0.003$, $\varphi = 0.34$, $t_s = 29^\circ$C.

surfaces formed by sintering braided copper wire mesh with micro-rib tips (MF+M). They reported a simplified semi-analytical model to determine the total heat flux for the studied surfaces.

Piasecka *et al.* [32] conducted extensive research on the boiling process of refrigerants with low ODPs and GWPs. They presented the results of a study of the heat transfer process during subcooled boiling in a multiport constructed of three or five mini-channels 1 mm high. FC72 fluid was used in the study. The mini-channel was lined with a thin film, the temperature of which on the outer surface was measured by infrared thermography. Temperature distributions obtained from the finite elements method (FEM) calculations performed by ADINA software [33] were presented. Sample boiling curves indicating nucleation hysteresis were presented and discussed. Another paper focused on the study of heat transfer during the boiling process in the flow of FC72, HFE649, HFE7000, and HFE7100 fluids in a single 1.7-mm-high mini-channel, oriented vertically or horizontally [34]. Infrared thermography was used to measure the temperature. Observations

of flow structures were also made. The results were presented as the change in the heat transfer coefficient along the length of the channel (Fig. 6) and as boiling curves. These authors compared their results with the results of calculations according to the correlations of various authors, and the best match was obtained for the correlation of Mikielewicz [35]. For saturated boiling, their own correlation was proposed

$$\mathrm{Nu} = 4.19 \mathrm{We}^{-4.12} \mathrm{Pr}^{0.74} \mathrm{Bo}^{-2.16}, \tag{2}$$

where We is the Weber number and Bo is the Bond number.
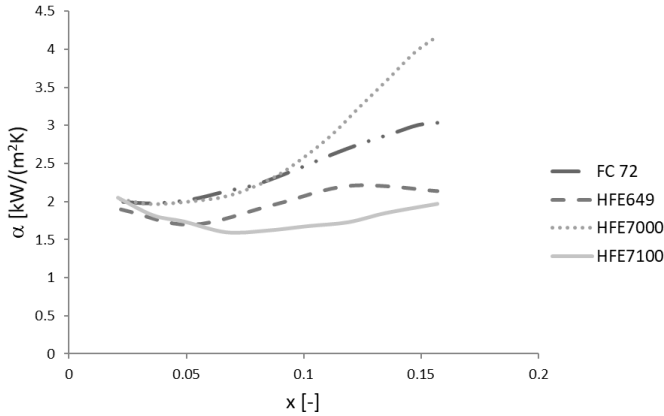


Figure 6: Change in the heat transfer coefficient along the mini-channel during the boiling process of the studied refrigerants at a heat input flux density of $q = 65$ kW/m$^2$ [32].

Piasecka and Strąk [34, 36, 37] presented the results of similar tests carried out in a single rectangular channel of 180 mm in length and a bundle of five parallel mini-channels of 32 mm in length. The effects of the slope angle of the channels and the porosity of the heating surface on the boiling process were analyzed, and the results of heat transfer during refrigerant flow in rectangular mini-channels under stationary conditions were presented. The influence of selected parameters on the boiling process was discussed, including thermal flow parameters, dimensions, and orientation of the channels. The highest values of the heat transfer coefficient were obtained for channel angles of 0 and 270°. The boiling process of refrigerant from the HFE and FC groups is quite extensively reported in the literature. Cao *et al.* [18] dealt with the process of heat transfer intensification during boiling of HFE7200 and Novec 649.

In order to intensify heat transfer, nanoparticles were used to coat the heat transfer surface. This treatment improved the value of the heat transfer coefficient during boiling of the HFE7200 medium by 190%. At the same time, visualization studies of vapour bubble formation were carried out to determine the diameter and velocity of bubbles detached from the heat transfer surface [18, 19]. A study of the boiling process of HFE refrigerants was also published in the work of Eraghubi *et al.* [38].

Boiling and condensation are of great importance in the cooling process because some of the HFE and FC group refrigerants are nonconductive and can be used to cool electronic components. Since such components are small in size, there is a trend toward the miniaturization of heat exchangers while intensifying heat transfer. Kruzel, Bohdal and Dutkowski [39] presented the results of a study of the condensation process of HFE7000 and HFE7100 refrigerants in a shell-and-tube heat exchanger built with 4- to 6-mm-diameter channels and a shell with an inner diameter of 30 mm. The condensation process took place on the surface of the tube bundle, and water was used as the cooling medium. The authors conducted thermal flow tests under the following conditions: $G = 20-700$ kg/m$^2$s, $q = 3000-60000$ W/m$^2$, $t_s = 40-80°$C. The same authors conducted tests using HFE7000 refrigerant and a mixture of water and phase-change microcapsules in a shell-and-tube heat exchanger. They showed that, particularly around the phase transition temperature of the phase-change material, there is a sharp increase in the heat transfer coefficient on the side of the mixture of water and microcapsules. This is due to an increase in the heat capacity of this mixture. This results in an increase in the heat exchanger's thermal efficiency in this range of operating parameters. The tests were carried out under the following conditions: mass flux of refrigerant $m_r = 0.0014–0.0015$ kg/s, mass flux coolant $m_c = 0.014-0.016$ kg/s, refrigerant saturation temperature $t_s = 55-60°$C, inlet coolant temperature $t_{cin} = 20-32°$C, and heat flux density $q = 7000-7450$ W/m$^2$. The average increase in the heat transfer coefficient was 13% [40]. Woodoc *et al.* [41], on the other hand, investigated the use of the HFE7000 refrigerant in an 800-µm-thick silicon mini-heat exchanger (MECH-X). The exchanger was used to cool electronic components, which were heated to 90°C. What is more, Andrzejczyk and Muszyński [23] conducted studies on the influence of refrigerant properties and geometry on the performance of two-phase closed thermosiphon (TPCT). The tests were carried out on HFE7100 refrigerant as well as water, R134a, SES36 and ethanol. The presented constructions of thermosyphons were to be used to recover heat from

industrial wastewater, which is of great importance in terms of the energy economy.

# 4 Conclusions

This article presented a review of available information on new working fluids with low GWP and ODP values. As discussed earlier, refrigerants from the HFE group can be successfully used in a wide range of thermal transformations. They can successfully replace refrigerants from the FC group, which are less environmentally friendly but have similar application ranges. The Novec 649 refrigerant has both a higher heat capacity and thermal conductivity (at least to some extent) than the FC72 refrigerant. Other refrigerants in the HFE group also show better thermal properties than the FC72 refrigerant. Thus, these substances can be used in a wide range of thermal processes as follows:

- for both single-phase and two-phase cooling electronics, also by immersion,

- in ORC systems and other high-temperature refrigeration systems, and

- in cascade heat pumps and refrigeration systems.

In order to intensify heat transfer, HFE group refrigerants can also be used in combination with phase-change materials. Novec 649 and HFE7200 fluids have the lowest environmental impact due to their low GWP, so they are most often preferred over less environmentally friendly refrigerants with similar operating parameters. HFE7500 and HFE7600 refrigerants have saturation temperatures at normal pressure above 100°C, which limits their use in phase transformation (boiling or condensing).

# References

[1] 3M: 3M Thermal Management Fluids. https://multimedia.3m.com/mws/media/56 9860O/3mtm-thermal-management-fluids-for-military-aerospace-apps.pdf (acessed 4 Sep. 2018).

[2] Muńoz-Rujas N., Aguilar F., García-Alonso J.M., Montero E.A.: *Thermodynamics of binary mixtures 1-ethoxy-1,1,2,2,3,4,4,4-nonafluorobutane (HFE-7200) + 2-propanol: High pressure density, speed of sound and derivative properties.* J. Chem. Thermodyn. **131**(2019), 630–647. doi: 10.1016/j.jct.2018.12.018

[3] Zheng Y., Gao H., Chen Q., Meng X., Wu J.: *Isobaric heat capacity measurements of liquid HFE-7200 and HFE-7500 from 245 to 353K at pressures up to 15MPa.* Fluid Phase Equilibr. **372**(2014), 56–62. doi: 10.1016/j.fluid.2014.03.017

[4] Pastuszko R., Kaniowski R., Wójcik T.M.: *Comparison of pool boiling performance for plain micro-fins and micro-fins with a porous layer.* Appl. Therm. Eng. **166**(2020), 114658. doi: 10.1016/j.applthermaleng.2019.114658

[5] Rausch M.H., Kretschmer L., Will S., Leipertz A., Fröba A.P.: *Density, surface tension, and kinematic viscosity of hydrofluoroethers HFE-7000, HFE-7100, HFE-7200, HFE-7300, and HFE-7500.* J. Chem. Eng. Data. **60**(2015), 3759–3765. doi: 10.1021/acs.jced.5b00691

[6] 3M: 3M Novec 7100 Engineered Fluid. https://multimedia.3m.com/mws/media/ 199818O/3m-novec-7100-engineered-fluid.pdf (acessed 9 Sep. 2009).

[7] 3M: 3M Fluorinert Electronic Liquid FC-72. https://multimedia.3m.com/mws/ media/64892O/3m-fluorinert-electronic-liquid-fc72-en.pdf (acessed 09 Sep. 2009).

[8] 3M: 3M Novec 649 Engineered Fluid. https://multimedia.3m.com/mws/media/ 569865O/3m-novec-engineered-fluid-649.pdf (acessed 9 Sep. 2009).

[9] 3M: 3M Novec 7200 Engineered Fluid. https://multimedia.3m.com/mws/media/ 199819O/3m-novec-7200-engineered-fluid-en.pdf (acessed 9 Sep. 2009).

[10] 3M: 3M Novec 7500 Engineered Fluid. https://multimedia.3m.com/mws/media/ 65496O/3m-novec-7500-engineered-fluid.pdf (acessed 9 Sep. 2008).

[11] 3M: 3M Novec 7000 Engineered Fluid. https://multimedia.3m.com/mws/media/ 121372O/3m-novec-7000-engineered-fluid-tds.pdf (acessed 9 Sep. 2021).

[12] Forrest E., Hu L.-W., Buongiorno J., MCKrell T.: *Pool boiling performance of NovecTM 649 engineered fluid.* In: Proc. ECI Int. Conf. on Boiling Heat Transfer. Florianópolis-SC-Brazil, 2009, 1–7.

[13] Bonk C.D., Laux C., Rödder M., Neef M.: *Design of a 1 kW organic Rankine cycle for teaching and research issues.* Energy Proced. **129**(2017), 931–938. doi: 10.1016/j.egypro.2017.09.117

[14] Bruder M., Sembach L., Krumova V., Sattelmayer T.: *Local data of heat flux, wall temperature and the void phase along the boiling curve during vertical subcooled flow boiling of refrigerant Novec 649 at a copper wall.* Data Br. **21**(2018), 1415–1429. doi: 10.1016/j.dib.2018.10.138

[15] Bruder M., Sembach L., Lampl D., Hirsch C., Sattelmayer T.: *Local measurements on vertical subcooled flow boiling of refrigerant Novec 649.* Int. J. Multiphas. Flow **119**(2019), 108–122. doi: 10.1016/j.ijmultiphaseflow.2019.07.012

[16] Fu B.-R., Lin W.-J.: *Supercritical heat transfer of NOVEC 649 refrigerant in horizontal minichannels.* Int. Commun. Heat Mass Transf. **117**(2020), 104740. doi: 10.1016/j.icheatmasstransfer.2020.104740

[17] Wu Z., Cao Z., Sundén B.: *Saturated pool boiling heat transfer of acetone and HFE-7200 on modified surfaces by electrophoretic and electrochemical deposition.* Appl. Energ. **249**(2019), 286–299. doi: 10.1016/j.apenergy.2019.04.160

[18] Cao Z., Wu Z., Sundén B.: *Pool boiling of NOVEC-649 on microparticle-coated and nanoparticle-coated surfaces.* Heat Transf. Eng. **42**(2021), 19–20, 1732–1747. doi: 10.1080/01457632.2020.1818419

[19] Cao Z., Wu Z., Sundén B.: *Heat transfer prediction and critical heat flux mechanism for pool boiling of NOVEC-649 on microporous copper surfaces.* Int. J. Heat Mass Transf. **141**(2019), 818–834. doi: 10.1016/j.ijheatmasstransfer.2019.07.036

[20] Adebayo V., Abid M., Adedeji M., Dagbasi M., Bamisile O.: *Comparative thermodynamic performance analysis of a cascade refrigeration system with new refrigerants paired with $CO_2$.* Appl. Therm. Eng. **184**(2021), 116286. doi: 10.1016/j.applthermaleng.2020.116286

[21] Mikielewicz D., Andrzejczyk R., Mikielewicz J.: *Pressure drop of HFE7000 and HFE7100 in flow condensation in minichannels with account of non-adiabatic effects.* In: Proc. MATEC Web Conf. **18**(2014), 01007. doi: 10.1051/matecconf/20141801007

[22] Mikielewicz D., Wajs J., Andrzejczyk R., Klugmann M.: *Pressure drop of HFE7000 and HFE7100 during flow condensation in minichannels.* Int. J. Refrig. **68**(2016), 226–241. doi: 10.1016/j.ijrefrig.2016.03.005

[23] Andrzejczyk R., Muszyński T.: *The performance of H2O, R134a, SES36, ethanol, and HFE7100 two-phase closed thermosyphons for varying operating parameters and geometry.* Arch. Thermodyn. **38**(2017), 3–21. doi: 10.1515/aoter-2017-0013

[24] Fronk B.M., Garimella S.: *Measurement of heat transfer and pressure drop during condensation of carbon dioxide in microscale geometries.* In: Proc. 14th Int. Heat Transfer Conf. 2010, Vol. 2. ASMEDC, 2010, 235–243.

[25] Mikielewicz D., Andrzejczyk R., Jakubowska B., Mikielewicz J.: *Comparative study of heat transfer and pressure drop during flow boiling and flow condensation in minichannels.* Arch. Thermodyn. **35**(2014), 3, 17–37. doi: 10.2478/aoter-2014-0019

[26] Sikora M., Bohdal T.: *Heat and flow investigation of NOVEC649 refrigerant condensation in pipe minichannels.* Energy **209**(2020), 118447. doi: 10.1016/j.energy.2020.118447

[27] Sikora M., Bohdal T., Formela K.: *Experimental study of HFE 7000 refrigerant condensation in horizontal pipe minichannels.* Materials (Basel) **14**(2021), 6886. doi: 10.3390/ma14226886

[28] Bohdal T., Charun H., Sikora M.: *Condensation of Novec 649 refrigerant in pipe minichannels.* E3S Web Conf. **70**(2018), 02002. doi: 10.1051/e3sconf/20187002002

[29] Sikora M., Bohdal T.: *Application of computer image analyses in the investigation of refrigerants condensation in minichannels.* Arch. Thermodyn. **40**(2019), 1, 103–114. doi: 10.24425/ather.2019.128292

[30] Al-Zaidi A.H., Mahmoud M.M., Karayiannis T.G.: *Condensation flow patterns and heat transfer in horizontal microchannels.* Exp. Therm. Fluid Sci. **90**(2018), 153–173. doi: 10.1016/j.expthermflusci.2017.09.009

[31] Sikora M.: *Flow structure investigations during novec refrigerant condensation in minichannels.* Materials (Basel) **14**(2021), 6889. doi: 10.3390/ma14226889

[32] Piasecka M., Maciejewska B., Łabędzki P.: *Heat transfer coefficient determination during FC-72 flow in a minichannel heat sink using the Trefftz functions and ADINA software.* Energies. **13**(2020), 6647. doi: 10.3390/en13246647

[33] https://www.adina.com/index.shtml (acessed 9 Sep. 2009).

[34] Piasecka M., Strąk K., Maciejewska B.: *Heat transfer characteristics during flow along horizontal and vertical minichannels.* Int. J. Multiph. Flow. **137**(2021), 103559. doi: 10.1016/j.ijmultiphaseflow.2021.103559

[35] Mikielewicz J.: *Semi-empirical method of determining the heat-transfer coefficient for subcooled, saturated boiling in a channel.* Int. J. Heat Mass Transf. **17**(1974), 1129–1134. doi: 10.1016/0017-9310(74)90114-8

[36] Piasecka M., Strąk K.: *Characteristics of refrigerant boiling heat transfer in rectangular mini-channels during various flow orientations.* Energies **14**(2021), 4891. doi: 10.3390/en14164891

[37] Strąk K., Piasecka M.: *The applicability of heat transfer correlations to flows in minichannels and new correlation for subcooled flow boiling.* Int. J. Heat Mass Transf. **158**(2020), 119933. doi: 10.1016/j.ijheatmasstransfer.2020.119933

[38] Eraghubi M., Di Marco P., Robinson A.J.: *Low mass flux upward vertical forced flow boiling of HFE7000.* Exp. Therm. Fluid Sci. **102**(2019), 291–301. doi: 10.1016/j.expthermflusci.2018.11.011

[39] Kruzel M., Bohdal T., Dutkowski K.: *External condensation of HFE 7000 and HFE 7100 refrigerants in shell and tube heat exchangers.* Materials (Basel) **14**(2021), 6825. doi: 10.3390/ma14226825

[40] Kruzel M., Bohdal T., Dutkowski K., Radchenko M.: *The effect of microencapsulated PCM slurry coolant on the efficiency of a shell and tube heat exchanger.* Energies **15**(2022), 5142. doi: 10.3390/en15145142

[41] Woodcock C., Ng'oma C., Sweet M., Wang Y., Peles Y., Plawsky J.: *Ultra-high heat flux dissipation with Piranha Pin Fins.* Int. J. Heat Mass Transf. **128**(2019), 504–515. doi: 10.1016/j.ijheatmasstransfer.2018.09.030

# A qualitative study of mixing a fluid inside a mechanical mixer with the effect of thermal buoyancy

**SOUAD HASSOUNI**[a]
**HOUSSEM LAIDOUDI**[b*]
**OLUWOLE DANIEL MAKINDE**[c]
**MOHAMED BOUZIT**[b]
**BOUMEDIENE HADDOU**[a]

[a] University of Science and Technology of Oran Mohamed-Boudiaf, Faculty of Chemistry, BP 1505, El-Menaouer, Oran, 31000, Algeria

[b] University of Science and Technology of Oran Mohamed-Boudiaf, Laboratory of Sciences and Marine Engineering, Faculty of Mechanical Engineering, BP 1505, El-Menaouer, Oran, 31000, Algeria

[c] Stellenbosch University, Faculty of Military Science, Private Bag X2, Saldanha 7395, South Africa

**Abstract**  This paper is concerned with the rotational motion of the impeller and the thermal buoyancy within a mechanical mixer. The task was investigated numerically using the ANSYS-CFX simulator. The programmer is based on the finite volume method to solve the differential equations of fluid motion and heat transfer. The impeller has hot surfaces while the vessel has cold walls. The rotational movement of the impeller was controlled by the Reynolds number, while the intensity of the thermal buoyancy effect was controlled by the Richardson number. The equations were solved for a steady flow. After analyzing the results of this research, we were able to conclude that there is no effect of the values of Richardson number on the power number. Also, with the presence of the thermal buoyancy effect, the quality of the fluid mixing becomes more important. The increasing Richardson number increases the value of the Nusselt number of the impeller.

**Keywords:** Mechanical agitation; Mixing process; Heat transfer; Thermal buoyancy; Power number

---

*Corresponding Author. Email: houssem.laidoudi@univ-usto.dz

# 1   Introduction

The fluid mixing process is one of the important processes in the industry, and we mention the following: pharmaceutical products, food products such as chocolate, cosmetic products, milk products and so on. The fluid mixing process is usually carried out in a container of a certain geometric shape with a mechanical mixer inside it. The rotational motion of the impeller mixes the fluid. The quality of the mixture of the fluid depends mainly on the geometry of the impeller and the container (vessel), as well as the speed of rotation of the mixer.

A group of investigations have been aligned for the purpose of understanding the mixing process of the mechanical agitator, in order to arrive at the method that allows for increasing the mixing speed and decreasing the mechanical energy of the impeller. Among these important works, we mention the following. Hadjeb *et al.* [1] performed numerical research on a two-bladed agitator; this work was addressed for highly viscous fluids. Some geometrical changes of the mixer were made in order to increase the blending efficiency of the mixing process. Ameur studied the effect of the shape of the vessel on the mixing process. The impeller used in this work was that of a six-curved-blade [2]. The studied shapes of the container were: a cylindrical vessel of flat bottom, cylindrical vessel of dished bottom and closed spherical vessel. The Herschel-Bulkley model was used to define the apparent viscosity of the fluid. The results showed that the last form of the vessel generated a uniform flow in the vessel. Ameur *et al.* [3] examined the hydrodynamic behaviour of highly viscous fluid in the mechanical agitator with the presence of a maxblend impeller. The investigations showed the effects of rotational speed, rheological characteristics and impeller clearance on the power consumption. Ameur and Bouzit simulated the rotation of a disc turbine impeller in the unbaffled vessel [4]. The working fluid was shear-thinning. It is a complex fluid whose dynamic viscosity depends on the shear rate. The results of this paper show the evolution of counter-rotating zones in the vessel with respect to pertinent parameters. Also, Ameur *et al.* investigated the mixing process for different shapes of impeller and vessel. The principal purpose of works [5–10] was to determine the best design of the impeller as well as of the vessel.

Cudak studied the agitation of a gas-liquid medium in a pseudophase system. The impeller of the mixing process was a Rushton turbine. The results of simulation were presented as contours of velocity and vectors [11]. Laidoudi presented a numerical work on a two-bladed impeller placed in an

unbaffled vessel [12]. Some new geometrical modifications were considered to improve the performance of the impeller. The results showed that the holed blades of the impeller are optimal. Foukrach *et al.* [13] simulated the turbulent flow in a cylindrical and polygonal vessel. The vessel in this research has vertical baffles. The $k-\varepsilon$ closure was used to model the turbulent flow. The results showed that the presence of vertical baffles in the vessel acts to improve the mixing process. Mishra *et al.* [14] simulated turbulent flow in a tank with a disc turbine. The work was to estimate rates of energy dissipation. Youcefi *et al.* [15] presented 3D simulations of turbulent flow in an unbaffled vessel. The purpose of the work was the estimation of the flow structure in the vessel. Torré *et al.* [16] presented experimental and numerical investigations of the impeller in an unbaffled vessel. Particle image velocimetry (PIV) was the experimental technique used for measuring the flow velocity. On the other hand, the standard $k - \varepsilon$ closure was also used to model the turbulent flow.

In addition to this, there are also some recently published papers [17–25], which on aggregate are hydrodynamic studies of the mixing process. The ultimate purpose of all these works is to reach a more efficient impeller that allows for speeding up the mixing process while reducing the consumption of mechanical energy. On other hand, thermal buoyancy can be defined as a force that allows hot fluid layers to move upwards, because they become less dense due to their high temperature. In fact, there is a group of papers that exploited this thermal property in enhancing thermal activity and controlling fluid movement such as [26–32].

In many industrial activities, we encounter the mixing process with the presence of heat transfer. However, after reviewing previous research papers in this field, it is clear that there is a lack of works that combine mechanical mixing and heat transfer. Therefore, through this work, we decided to support new findings in this area.

## 2   Geometrical description and mathematical modeling

Figure 1 shows the physical domain. It is formed of a cylindrical vessel (container) with a four-bladed impeller presented in Fig. 1a. Figure 1b shows the cross-section of the studied domain. The diameter of the vessel is given by $D$, while the diameter of the impeller is given $d$. The ratio between the two diameters is given as $d/D = 0.5$. The vessel also contains

four internal inflections. The radius of each cavity ($e$) is given by the ratio $e/D = 0.13$. Figure 1c shows the longitudinal view of the domain. The ratio between the height of the vessel ($H$) and its diameter is $H/D = 1$. The width of the blade of the impeller ($a$) is given by $a/D = 0.17$. The gap ($c$) between the flatted bottom of the vessel and the impeller is $c/D = 0.067$. The vessel is completely filled with a Newtonian fluid (water). However, the impeller surfaces have a high temperature ($T_h$) and the lateral walls of the vessel have a cold temperature ($T_c$). The flatted bottom and the top of the vessel have an adiabatic condition.
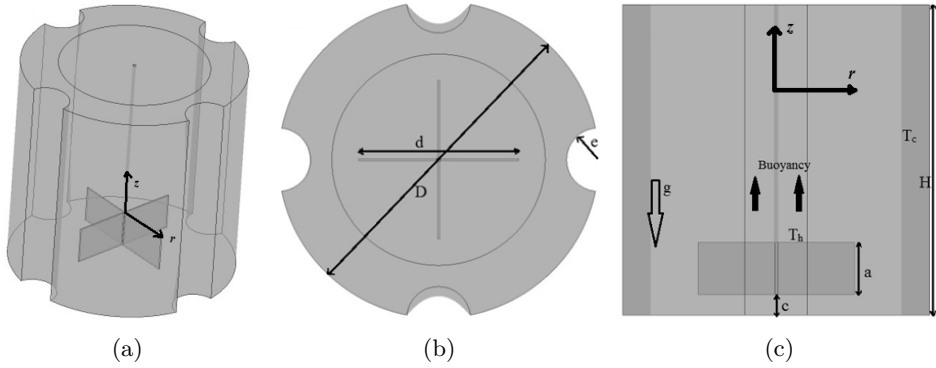


Figure 1: The studied domain: a) general view, b) cross-section view, c) longitudinal view.

We note that the rotation of the impeller creates a flow inside the vessel, and these results generate the forced convection heat transfer. On the other hand, the gradient temperature between the impeller and vessel surfaces generates a natural convection heat transfer. Together we get the mixed convection.

The Reynolds number controls the rotational speed of the impeller as

$$\text{Re} = \frac{\rho N D^2}{\mu} \, , \tag{1}$$

where $\rho$, $N$, and $\mu$ are the fluid density, rotational speed, and dynamic viscosity, respectively.

The Prandtl number defines the thermophysical proprieties of the fluid:

$$\text{Pr} = \frac{\vartheta cp}{k} \, , \tag{2}$$

where $\upsilon$, $cp$, and $k$ are the kinematic viscosity, heat capacity of the fluid, and thermal conductivity, respectively. Indeed, $\text{Pr} = 6.01$ in this paper.

The Richardson number defines the intensity of thermal buoyancy.

$$\text{Ri} = \frac{g\beta_T \Delta T D^3}{(ND)^2},\tag{3}$$

where $g$ and $\beta_T$ are the gravitational acceleration and dilatation coefficient of the fluid, and $\Delta T = (T_h - T_c)$ is the difference in temperature between the hot temperature of the impeller surfaces and a cold temperature of the lateral walls of the vessel.

The power number characterizes the consumption power and is given as:

$$\text{Np} = \frac{P}{\rho N^3 D^5},\tag{4}$$

where $P$ is the mechanical power and it is calculated as a volume integral:

$$P = \mu \int\limits_{\text{vessel\_volume}} Q_v \, dv,\tag{5}$$

where $Q_v$ denotes viscous dissipation. For the cylindrical coordinate system $(r, \theta, z)$ $dv$ is expressed in the form

$$dv = r \, dr \, d\theta \, dz,\tag{6}$$

and we have

$$Q_v = \frac{1}{\mu^2}\left(2\tau_{rr}^2 + 2\tau_{\theta\theta}^2 + 2\tau_{zz}^2 + 2\tau_{rz}^2 + 2\tau_{r\theta}^2 + 2\tau_{z\theta}^2\right),\tag{7}$$

where

$$\tau_{rr} = -2\mu\left(\frac{\partial v_r}{\partial r}\right),\tag{8}$$

$$\tau_{r\theta} = -\mu\left[r\frac{\partial(v_\theta/r)}{\partial r} + \frac{1}{r}\frac{\partial v_r}{\partial\theta}\right],\tag{9}$$

$$\tau_{rz} = -\mu\left[\frac{\partial v_r}{\partial z} + \frac{\partial v_z}{\partial r}\right].\tag{10}$$

The average Nusselt number of the impeller is calculated through the integration of the local Nusselt number $(\text{Nu}_L)$ over all impeller surfaces $(A)$ as

$$\text{Nu} = \frac{1}{A}\int \text{Nu}_L \, dA,\tag{11}$$

where

$$\text{Nu}_L = \left(\frac{\partial\theta}{\partial n_s}\right)_{\text{wall}}\tag{12}$$

and $n_s$ is the normal unit vector.

# 3   Simulation steps

Gambit was used for the design and generation of the mesh grid. The grid has unstructured elements with non-uniform distribution as shown in Fig. 2. The concentration of elements is around the impeller. The number of meshing elements was selected after the grid independence test. The results of the grid independence test are presented in Table 1. It is clear that grid G2 is sufficient for the present computation, because the difference between this grid (G2) and the third one (G3) is very small (around 0.12%).
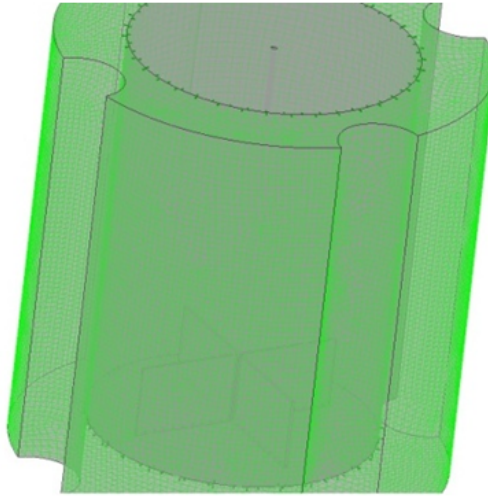


Figure 2: Grid quality for the studied domain.

Table 1: Results of grid independence test, for Re = 30, Ri = 0 and Pr = 6.01

| Case | Elements | Np | Variation, % |
|------|----------|-----|--------------|
| G 1 | 231.500 | 0.006945 | 7.79 |
| G 2 | 463.000 | 0.007532 | 0.12 |
| G 3 | 926.000 | 0.007541 | – |

The simulations were carried out using the finite volume method (ANSYS-CFX simulator [33]). The SIMPLEC (semi-implicit method for pressure linked equations-consistent) algorithm was used for coupling pressure and velocity. Meanwhile, the high-resolution discretisation scheme was used for solving the convective term. The relative errors of the computations are

$10^{-8}$ for the continuity and momentum equations and $10^{-6}$ for the energy equation. Furthermore, the multi-reference frame (MRF) method was used for this simulation [33]. The inner impeller was created in the rotating domain, while the rest of the domain was selected fixed.

In this section, the validation test is described where the present numerical methodology has been proofed. The results of the validation test are shown in Fig. 3. Indeed, a good agreement is shown between our results and the results of Ameur *et al.* [9]. The notable difference between the results of our simulation (present data) and the previous work (Ameur *et al.* [9]) is due to the uncertainty involved in the method used in the calculation of correlation of Ameur *et al.*
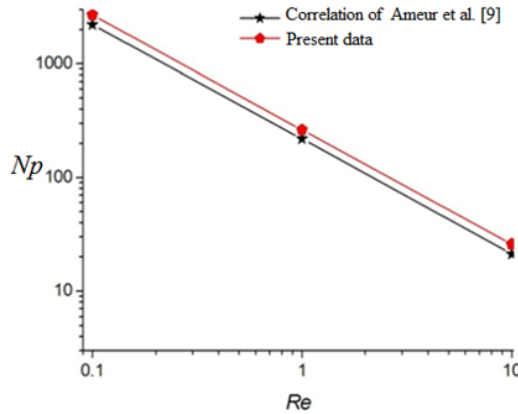


Figure 3: Validation test.

# 4   Results and discussion

The results of this work include mechanical agitation and mixed convection heat transfer for a fluid inside a cylindrical vessel. The vessel has four cavities of a semi-circular shape and a flat base. However, the impeller has also four blades. The purpose of this research is to predict the movement of the fluid inside the vessel due to the rotation of the impeller.

Figure 4 presents the dimensionless velocity distribution over the cross-section of height $Z = 0.35$ as defined in relation to the total height of the vessel ($Z = z/H$). The flow velocity is made dimensionless with respect to speed rotation of the impeller. Figure 4 shows the effect of the rotational speed of the impeller on the movement of the fluid without the effect of

thermal buoyancy (Ri = 0). It is clear that the maximum value of the velocity is at the head of the blades while it gradually decreases as we move towards the wall of the vessel from the centre of the impeller. It is also noted that there is no noticeable influence of the studied values of the Reynolds number on the fluid motion.
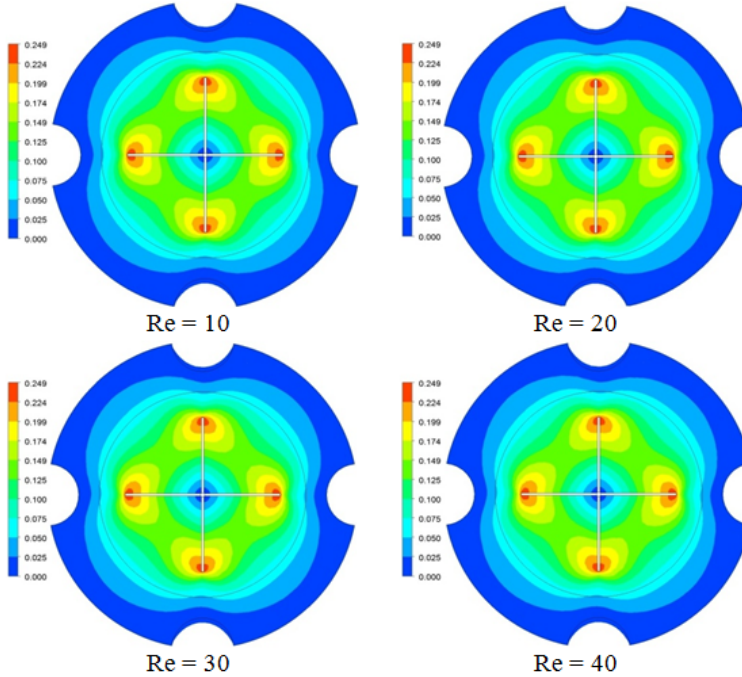


Figure 4: Contours of dimensionless velocity for different Re at Ri = 0.

Figure 5 shows the gradual effect of thermal buoyancy on the dynamic behaviour of the flow for a constant value of Reynolds number (Re = 40). Increasing the value of Richardson number indicates an increase in the thermal buoyancy effect. Figure 5 illustrates the variation in velocity distribution in the same section as in Fig. 4. We note that the higher the value of Ri, the greater the flow velocity. It can be concluded that the fluid movement is very important in this case, which makes the fluid mixing process better and faster.

Figure 6 exhibits the dimensionless velocity distribution contours for different Richardson numbers in the longitudinal section of the vessel with the impeller at Re = 40. Note that in the case Ri = 0, the velocity diffusion is
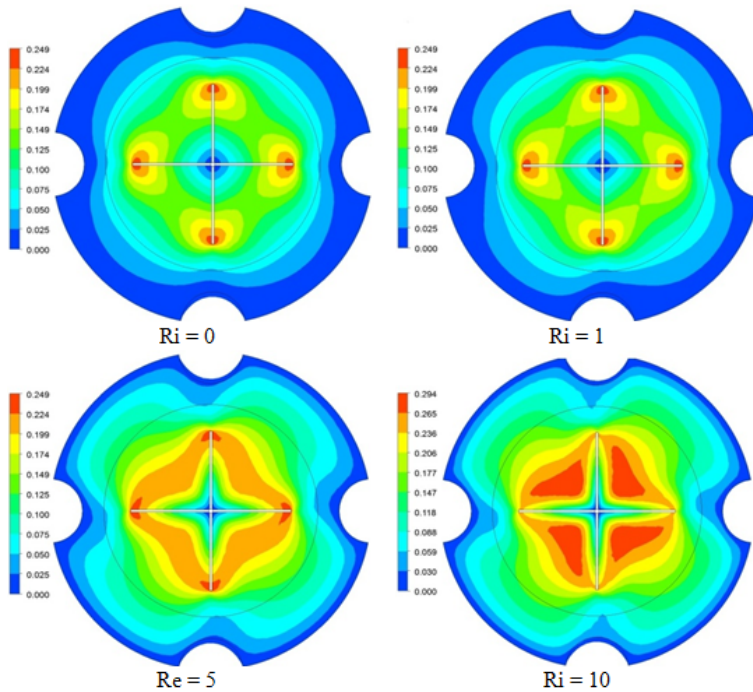
Figure 5: Contours of dimensionless velocity for different Ri at Re = 40.

only at the bottom near the impeller blades. Whereas, the higher the value of the Richardson number, the greater the velocity spread to the top. This phenomenon is explained by the following: the fact that the mixer is hot is what pushes the hot fluid particles upward, and this is what makes the fluid velocity increasing with (increasing) Richardson number. It is also noted from Fig. 6 that the mixing process of the fluid due to the thermal buoyancy phenomenon is very significant compared to the mechanical mixing of the impeller.

Figures 7 and 8 show the isotherms for different Ri and for Re = 40. Figure 7 forms a cross-sectional view at the height $Z = 0.35$, whereas Figure 8 is a longitudinal view of isotherms. It is clear that the dissipation of gradient temperature around the impeller decreases with the increasing Richardson number, which means that the temperature gradient becomes important with the increasing Richardson number. So, we can predict that the heat transfer between the impeller and the fluid increases gradually with the increasing Richardson number. It appears clear from Fig. 7 that
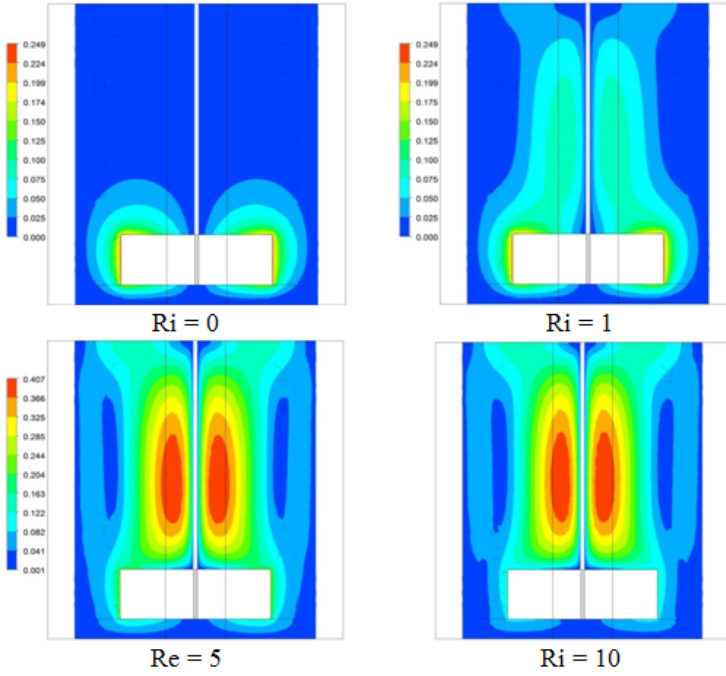
Figure 6: Contours of dimensionless velocity for different Ri at Re = 40 (longitudinal section).
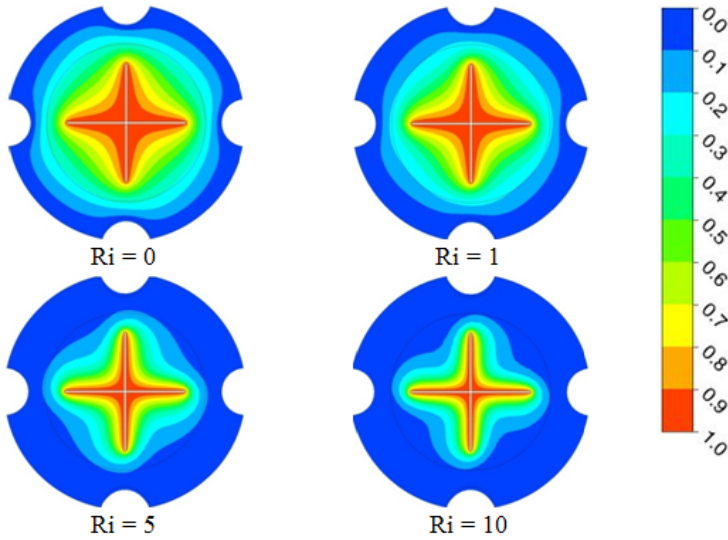


Figure 7: Isotherms (dimensionless temperature) at cross-section Z = 0.35 for different Ri for Re = 40.

the lower side of the impeller experiences a larger rate of heat transfer as compared to the upper side. In addition to this, it can be seen that the fluid motion intensifies with increasing thermal buoyancy and this confirms the previous results.
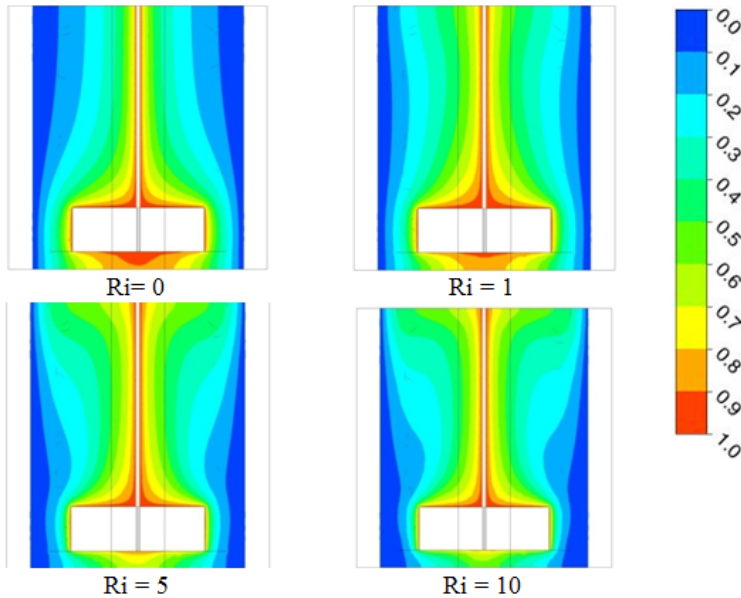


Figure 8: Longitudinal view of isotherms (dimensionless temperature) for different Ri for Re = 40.

Figure 9 presents the variation of the dimensionless velocity component $W$ along the radius of the vessel at the height $Z = 0.5$. The first thing that can be seen is that the velocity $W$ increases with the increasing value of Richardson number. Near the impeller, the velocity sign is positive, that is the flow is directed upwards, while near the vessel wall, the velocity sign is negative, meaning that the direction of the flow is downward. It is also noted that the value of the maximum velocity of the upward flow is much greater than the value of the maximum velocity of the downward flow.

Figure 10 shows the variation of power number with Reynolds number and Richardson number. It is clear that increasing the Reynolds number decreases the value of power number. On the other hand, there is no change in the power number with respect to the Richardson number. This confirms that there is no effect of thermal buoyancy on the mechanical energy of the impeller.
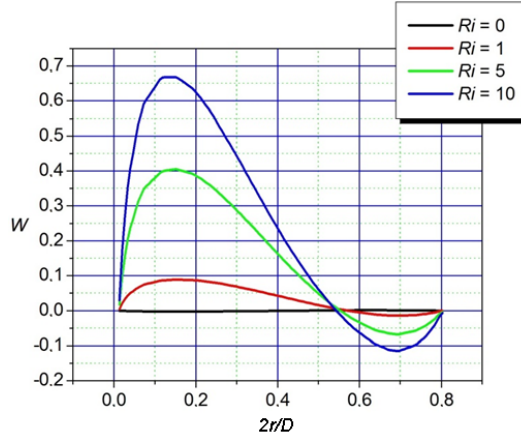
Figure 9: Dimensionless velocity along the vessel radius as a function of Ri for Re = 40.
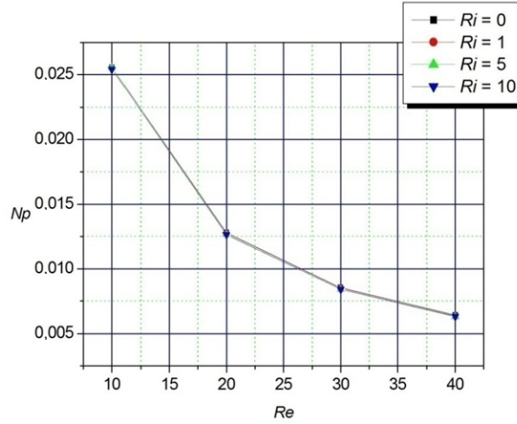


Figure 10: Variation of power number *versus* Re and Ri.

Figure 11 shows the evolution of the Nusselt number with the Richardson and Reynolds numbers. Note that since the heat transfer is of the forced convection type (Ri = 0), raising the Reynolds number does not effectively influence the value of the Nusselt number. On the other hand, in the mixed-type heat transfer (Ri $\neq$ 0), raising the value of the Reynolds number positively affects the value of the Nusselt number. It is noted that the effect of Reynolds number on Nusselt number is large whenever the value of Richardson number is significant.
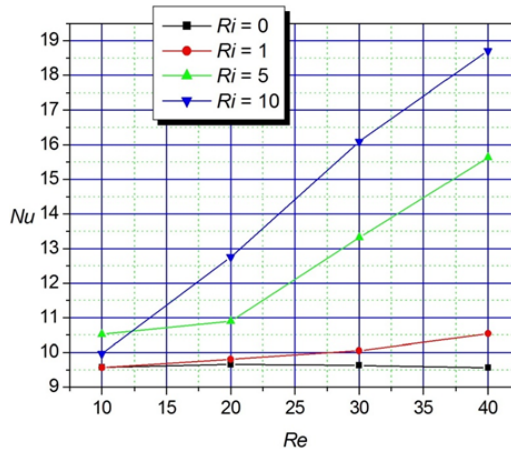
Figure 11: Variation of Nusselt number *versus* Re and Ri.

# 5  Summary

The research is concerned with 3D numerical simulation of a mechanical agitator. The impeller is a four-bladed turbine. The impeller has an elevated temperature while the vessel is cold. The impeller rotates at a constant speed. The purpose of this research is to study the effect of the impeller rotation speed and the thermal buoyancy factor on fluid motion in the vessel. After studying and analyzing the results, we have reached the following conclusions:

- Fluid motion within the vessel is intensified after the thermal buoyancy effect is added.

- When Ri = 0, increasing the Reynolds number does not affect the value of Nusselt number.

- The higher the value of Richardson number, the greater the effect of the value of Reynolds number on Nusselt number.

- With the presence of the thermal buoyancy effect, the quality of the fluid mixing is significantly increased.

- There is no effect of Richardson number on the power number.

Through the results of this work, we can suggest some new conditions for the intensification of the mixing process: such as the use of some complex fluids or the change in the configuration of the hot spots inside the vessel.

# References

[1] Hadjeb A., Bouzit M., KamlaY., Ameur H.: *A new geometrical model for mixing of highly viscous fluids by combining two-blade and helical screw agitators.* Pol. J. Chem. Technol. **19**(2017), 83–91.

[2] Ameur H.: *Agitation of yield stress fluids in different vessel shapes.* Eng. Sci. Technol. Int. J. **19**(2016), 189–196.

[3] Ameur H., Bouzit M., Helmaoui M.: *Hydrodynamic study involving a maxblend impeller with yield stress fluids.* J. Mech. Sci. Technol. **26**(2012), 1523–1530.

[4] Ameur H., Bouzit M.: *Numerical investigation of flow induced by a disc turbine inunbaffled stirred tank.* Acta Sci. **35**(2013), 469-476.

[5] Ameur H., Bouzit M.: *3D hydrodynamics and shear rates variability in the United-States Pharmacopeia paddle dissolution apparatus.* Int. J. Pharm. **452**(2013), 42–51.

[6] Ameur H., Bouzit M., Ghenaim A.: *Numerical study of the performance of multistage Scaba 6SRGT impellers for the agitation of yield stress fluids in cylindrical tanks.* J. Hydrodyn. Ser. B **27**(2015), 3, 436–442.

[7] Ameur H., Sahel D., Kamla Y.: *Energy efficiency of a deep hollow bladed impeller for mixing viscoplastic fluids in a cylindrical vessel.* Adv. Mech. Eng. **9**(2017), 1–7.

[8] Ameur H., Kamla Y., Sahel D.: *Optimization of the operating and design conditions to reduce the power consumption in a vessel stirred by a paddle impeller.* Period. Polytech. Mech. Eng. **62**(2018), 312–319.

[9] Ameur H., Bouzit M.: *Power consumption for stirring shear thinning fluids by two-blade impeller.* Energy **50**(2013), 326–332.

[10] Ameur H., Bouzit M., Helmaoui M.: *Numerical study of fluid flow and power consumption in a stirred vessel with a Scaba 6SRGT impeller.* Chem. Process Eng. **32**(2011), 351–366.

[11] Cudak M.: *Numerical analysis of hydrodynamics in a mechanically agitated gas-liquid pseudophase system.* Chem. Pap. **73**(2018), 481–489.

[12] Laidoudi H.: *Hydrodynamic analyses of the flow patterns in stirred vessel of two bladed impeller.* J. Serb. Soc. Comput. Mech. **14**(2020), 117–132.

[13] Foukrach M., Bouzit M., Ameur H., Kamla Y.: *Influence of the vessel shape on the performance of a mechanically agitated system.* Chem. Pap. **73**(2018), 469–480.

[14] Mishra V.P., Kumar P., Joshi J.B.: *Flow generated by a disc turbine in aqueous solutions of polyacrylamide.* Chem. Eng. J. **71**(1998), 11–21.

[15] Youcefi S., Bouzit M., Ameur H., Kamla Y., Youcefi A.: *Effect of some design parameters on the flow fields and power consumption in a vessel stirred by a Rushton turbine.* Chem. Process Eng. **34**(2013), 293–307.

[16] Torre J.P., Fletcher D.F., Lasuye T., Xuereb C.: *Single and multiphase CFD approaches for modelling partially baffled stirred vessels: Comparison of experimental data with numerical predictions.* Chem. Eng. Sci. **62**(2007), 6246–6262.

[17] Heidari A.: *CFD simulation of impeller shape effect on quality of mixing in two-phase gas-liquid agitated vessel*. Chinese J. Chem. Eng. **28**(2020), 2733–2745.

[18] Ghotli R.A., Shafeeyan M.S., Abbasi M.R., Ramand A.A.A., Ibrahim S.: *Macromixing study for various designs of impellers in a stirred vessel*. Chem. Eng. Process. – Process Intensific. **148(**2020), 107794.

[19] Ghotli R.A.R, Abbas M.R., Bagheri A.H., Raman A.A.A., Ibrahim S., Bostanci H.: *Experimental and modeling evaluation of droplet size in immiscible liquid-liquid stirred vessel using various impeller designs*. J. Taiwan Inst. Chem. Eng. **100**(2019), 26–36.

[20] Yamamoto T., Fang Y., KomarovS.V.: *Surface vortex formation and free surface deformation in an unbaffled vessel stirred by on-axis and eccentric impellers*. Chem. Eng. J. **367**(2019), 25–36.

[21] Yang F., Zhou S., An X.: *Gas-liquid hydrodynamics in a vessel stirred by dual dislocated-blade Rushton impellers*. Chinese J. Chem. Eng. **23**(2015), 1746–1754.

[22] Magelli F., Montante G., Pinelli D., Paglianti A.: *Mixing time in high aspect ratio vessels stirred with multiple impellers*. Chem. Eng. Sci. **101**(2013), 712–720.

[23] Takahashi K., Motoda M.: *Chaotic mixing created by object inserted in a vessel agitated by an impeller*. Chem. Eng. Res. Des. **87**(2009), 386–390.

[24] Cudmore G.C., Holloway A.G.L., Gerber A.G.: *A model of impeller whirl for baffled mixing vessels*. J. Fluid. Struct. **54**(2015), 719–742.

[25] Woziwodzki S.: *Mixing of viscous Newtonian fluids in a vessel equipped with steady and unsteady rotating dual-turbine impellers*. Chem. Eng. Res. Des. **92**(2014), 3, 435–446.

[26] Laidoudi H.: *Enhancement of natural convection heat transfer in concentric annular space using inclined elliptical cylinder*. J. Nav. Arch. Mar. Eng. **17**(2020), 89–99.

[27] Aliouane I., Kaid N., Ameur H., Laidoudi H.: *Investigation of the flow and thermal fields in square enclosures: Rayleigh-Bénard's instabilities of nanofluids*. Therm. Sci. Eng. Prog. **25**(2021), 100959.

[28] Laidoudi H., Bouzit M.: *The effects of aiding and opposing thermal buoyancy on downward flow around a confined circular cylinder*. Period. Polytech. Mech. Eng. **62**(2018), 42–50.

[29] Godoy T.: *Singular elliptic problems with Dirichlet or mixed Dirichlet-Neumann non-homogeneous boundary conditions*. Opuscula Math. **43**(2023), 19–46.

[30] Szymański P., Mikielewicz D.: *Challenges in operating and testing loop heat pipes in 500–700 K temperature ranges*. Arch. Thermodyn. **43**(2022), 2, 61–73.

[31] Cyklis P.: *Heat transfer in falling film evaporators during the industrial process of apple juice concentrate production*. Arch. Thermodyn. **39**(2018), 3, 3–13.

[32] Bulat P.V., Volkov K. N.: *Fluid/solid coupled heat transfer analysis of a free rotating disc*. Arch. Thermodyn. **39**(2018), 3, 169–192.

[33] ANSYS-CFX. https://www.ansys.com/products/fluids/ansys-cfx (acessed 11 Aug. 2022).

# Modeling the phenomena accompanying the condensation of environmentally friendly refrigerants in mini-channels

## WALDEMAR KUCZYŃSKI[*]

Koszalin University of Technology, Faculty of Mechanical Engineering, Department of Power Engineering, Racławicka 15-17, 75-625 Koszalin, Poland

**Abstract**   This paper presents the results of an experimental study and mathematical modeling of the effect of dynamic instabilities on the condensation phase transformation of the refrigerants homogeneous R134a and its replacement in the form of isomers R1234yf and R1234ze and R404A or R507 and R448A in pipe mini-channels. In the case of homogeneous chlorofluorocarbons (CFCs), it is the 1234 isomers that are envisioned as substitutes for the withdrawn ones with high ozone depletion potential and global warming potential. For zeotropic and azeotropic mixtures, for example, these are R507 or R448A. The paper presents a dimensional analysis procedure based on the Buckingham Π theorem to develop a regression velocity model of pressure dynamic instabilities. The experimental part of the work was carried out with the use of tubular mini-channels with internal diameter 1.40–3.3 mm.

## 1   Introduction

In the many papers, the possibility of using computational models developed to describe the impact of dynamic instabilities on the process of condensation of refrigerants in pipe mini-channels is demonstrated [1, 4, 9, 10,

---

[*]Corresponding Author. Email: waldemar.kuczynski@tu.koszalin.pl

13, 18]. These methods refer to the computational determination of the velocity of displacement of pressure instabilities, and the velocity of the liquefaction front.

It should be noted that in the literature there is a lack of publications describing dynamic instabilities with unitary characteristics and, in particular, a lack of computational models. Filling this information gap are the author's models presented in this paper. They concern the modeling of the propagation of pressure instabilities and the movement of liquefaction front, resulting from non-stable interactions of unitary nature [17]. The given solution can be applied to the phase transformation of refrigerant liquefaction implemented in mini-channels [3, 16, 20, 26]. A regression function was used to describe the velocity of the displacement of the pressure change signal and the temperature change signal. It describes the dependence of the expected value of a variable (in this case, the magnitudes of the velocity of displacement of pressure instabilities and the velocity of the liquefaction front) on the explanatory variables Buckingham $\Pi$ theorem, assuming that the number of dimensionless modules is equal to the number of independent physical parameters, minus the number of basic dimensions [5,6,8]. The presented method of determining dimensionless numbers, describing the speed of propagation of instability and the unknowns occurring in the regression equations, is included, as constant quantities and exponents of powers.

The magnitude of the velocity of the movement of the pressure change signal caused by instabilities of a unitary dynamic nature (velocity of movement of pressure instabilities) was functionally dependent on the following parameters:

$$v_p = f(\Delta p, \, p_o, \, v, \, d, \, w), \tag{1}$$

where: $\Delta p$ – amplitude of condensing pressure oscillations during disturbances, $p_o$ – average condensing pressure of the refrigerant, $\upsilon$ – kinematic viscosity coefficient of the two-phase mixture, $d$ – internal diameter of the mini-channel, $w$ – average velocity of the two-phase refrigerant mixture.

Equation (1) shows that the speed of movement of unit dynamic instabilities depends on the amplitude and frequency of their generation and the physical properties of the refrigerant. The magnitude of the amplitude of pressure oscillations ($\Delta p$) depends, in turn, on the step (unit) change in this value. In the case under consideration, there is a sudden disappearance or development of the condensation phase transformation process, caused by the sudden closure (or opening) of the shut-off valve on the refrigerant supply to the pipe mini-channel.

The primary quantity affecting the generation of dynamic instabilities, both pressure and temperature, is the mass flow rate of the refrigerant. Instabilities of this type are associated with mass flux density disturbances [7].

In the case of dynamic instabilities of the mass flow rate ($\dot{m}$) of the refrigerant, there is an impulsive (one-time) change in this quantity. The velocity of the two-phase refrigerant mixture in this case is determined by the relation

$$\dot{m}_{\text{mix}} = w\rho_{\text{TFP}}A \quad \Rightarrow \quad w = \frac{\dot{m}_{\text{dist}}}{\rho_{\text{TFP}}A}\,, \tag{2}$$

where: $A$ – cross-sectional area of the mini-channel, $\rho_{\text{TFP}}$ – density of the two-phase mixture is determined from the relation

$$\rho_{\text{TFP}} = \frac{\rho_L \rho_G}{\rho_G + x\left(\rho_L - \rho_G\right)}\,, \tag{3}$$

where the subscripts $G$ and $L$ stand for gas and liquid, respectively. The vapor quality ($x$) of the refrigerant in the sections of the mini-channel was calculated according to publications on the subject [15, 21].

Performing the procedures related to the application of dimensional analysis to relation (1) led to the dimensionless propagation velocity of unitary pressure instabilities:

$$v_p^+ = C\,\text{Re}_{\text{TPF}}^a \left(\Delta p^+\right)^b, \tag{4}$$

where: $a, b$ – exponents; $C$ – constant; $\Delta p^+$ – dimensionless pressure drop, $\text{Re}_{\text{TPF}}$ – Reynolds number for two-phase flow.

The dimensionless propagation velocity of pressure instabilities was determined by the ratio of the propagation ($v_p$) of the displacement of the pressure change signal to the average velocity in the two-phase mixture $(w)$, $\left(v_p^+ = \dfrac{v_p}{w}\right)$ and the dimensionless pressure drop was defined by the ratio of the amplitude ($\Delta p$) of pressure to the pressure ($p_o$) of condensing refrigerant $\left(\Delta_p^+ = \dfrac{\Delta p}{p_o}\right)$. The Reynolds number for two-phase flow in a mini-channel can, with the internal diameter $d$, be expressed as

$$\text{Re}_{\text{TPF}} = \frac{w\rho_{\text{TPF}}d}{\eta}\,,$$

where $\eta$ is the dynamic viscosity.

Equation (4) reduces to the following linear form:

$$\log v_p^+ = \log C + a\log\text{Re}_{\text{TPF}} + b\log\Delta p^+. \tag{5}$$

The value of the constant $C$ and the exponents $a$ and $b$ were calculated using a nonlinear regression model. The method used the procedure of highest reliability, which is an alternative to the method of least squares. The standard deviation of the observed value from the predicted value was determined using the so-called loss function. Maximization of the credibility function (selection of appropriate parameters satisfying this condition) was performed using the quasi-Newton and symplex methods, which are standard calculation modules in the Statistica software package. Equilibrium calculus was carried out (for a given refrigerant) for an appropriate number of equations built on the basis of experimental results for the range of applied disturbances.

In an analogous way to the regression function for unit pressure instabilities, the values of the dimensionless velocity of propagation of the liquefaction front were determined relating to the movement of temperature instabilities:

$$v_T = f(\Delta T, T_o, v, d, w), \tag{6}$$

where $\Delta T$ is the temperature oscillation and $T_o$ is the refrigerant condensation temperature. The application of dimensional analysis procedures made it possible to formulate the relationship for dimensionless velocity in the form of

$$v_T^+ = C \mathrm{Re}_{\mathrm{TPF}}^a \left(\Delta T^+\right)^b, \tag{7}$$

where $\Delta T^+$ is the dimensionless temperature drop determined by the ratio of the amplitude of the temperature oscillation, to the magnitude of the refrigerant condensation temperature $\left(\Delta T^+ = \dfrac{\Delta T}{T_o}\right)$.

Relationship (7) was also reduced to linear form:

$$\log v_T^+ = \log C + a \log \mathrm{Re}_{\mathrm{TPF}} + b \log \Delta T^+. \tag{8}$$

Calculation of the constant $C$ and the exponents $a$ and $b$ in Eq. (8) were performed according to the same calculation procedures as for the nonlinear regression model defined by relation (5).

The developed regression model was used to determine the propagation velocity of pressure and temperature instabilities occurring during the generation of unitary instabilities. The occurrence of physical phenomena of such instability character is associated with the process of rapid development or disappearance of refrigerant condensation, for example, in heat exchangers built of conventional channels, as well as mini-channels [14].

## 2   Methodology of experimental research

The realization of experimental studies was carried in accordance with for the identification of the effect of instabilities of a dynamic nature on the condensation of R404A and R134a refrigerants in mini-channels of pipes [12–14]. In the case of R507 and R448A refrigerants, the detailed parameters under which the tests were carried out were as follows:

- refrigerants – R404A, R507 and R448A;

- internal diameters $d = 3.3, 2.3, 1.9, 1.44$, and 1.40 mm;

- single channel configuration;

- refrigerant mass flux $G = 60$–316 kg/(m$^2$·s);

- refrigerant inlet pressure $p_{in} = 1.09$–7.5 MPa (saturation temperature in the range of 42.6–45.5°C.

Figure 1 shows a general view of the experimental station, while Fig. 2 shows a view of the measurement section, the schematic of which is presented in Fig. 3.
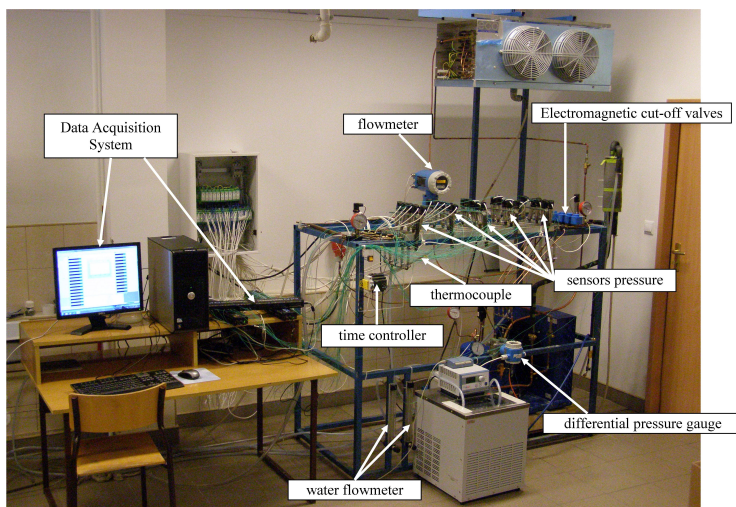


Figure 1: View of the test site [12–14].

Using electromagnetic cut-off valves (Fig. 1), instabilities of a dynamic nature were generated. The experiment was performed in a methodology that
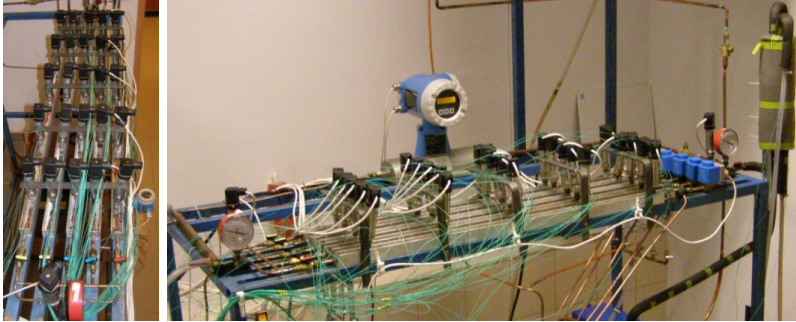
Figure 2: View of channels for studying heat transfer during refrigerant condensation in mini-channels of pipes with pressure and temperature sensors installed [12–14].
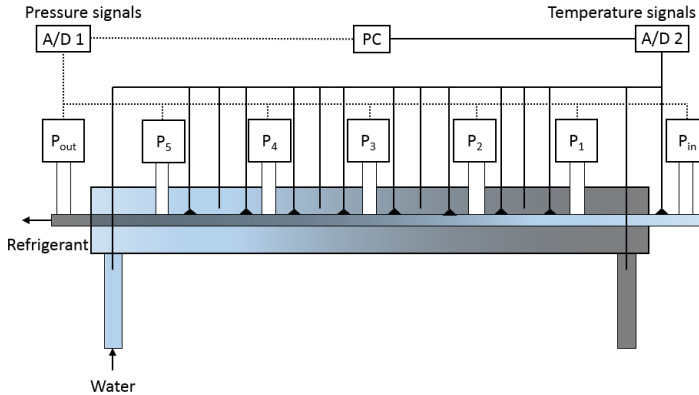


Figure 3: Schematic diagram of the measurement section [12–14].

allows identification of the development and disappearance of the condensation process of the studied refrigerants [2, 12, 19].

In order to achieve intensification of the liquefaction process, the method of increasing the mass flux by means of opening the supply valve with adjustable time ($t$) was used. On the other hand, the disappearance of the liquefaction process was obtained by abruptly closing the shut-off valve [12–14]. This allowed us to determine the minimum time at which the response of the system to the induced dynamic was noticeable is $t_o = 0.3$ s. Tests were carried out in the range of valve opening and closing times $t_o = 0.3$–3.5 s, using an increase or decrease in this time every 0.05 s in successive measurements. Figure 4 shows the results of the tests on the issue under consideration [12].

Condensation development process          Condensation fading process

R404A

R507

R448A
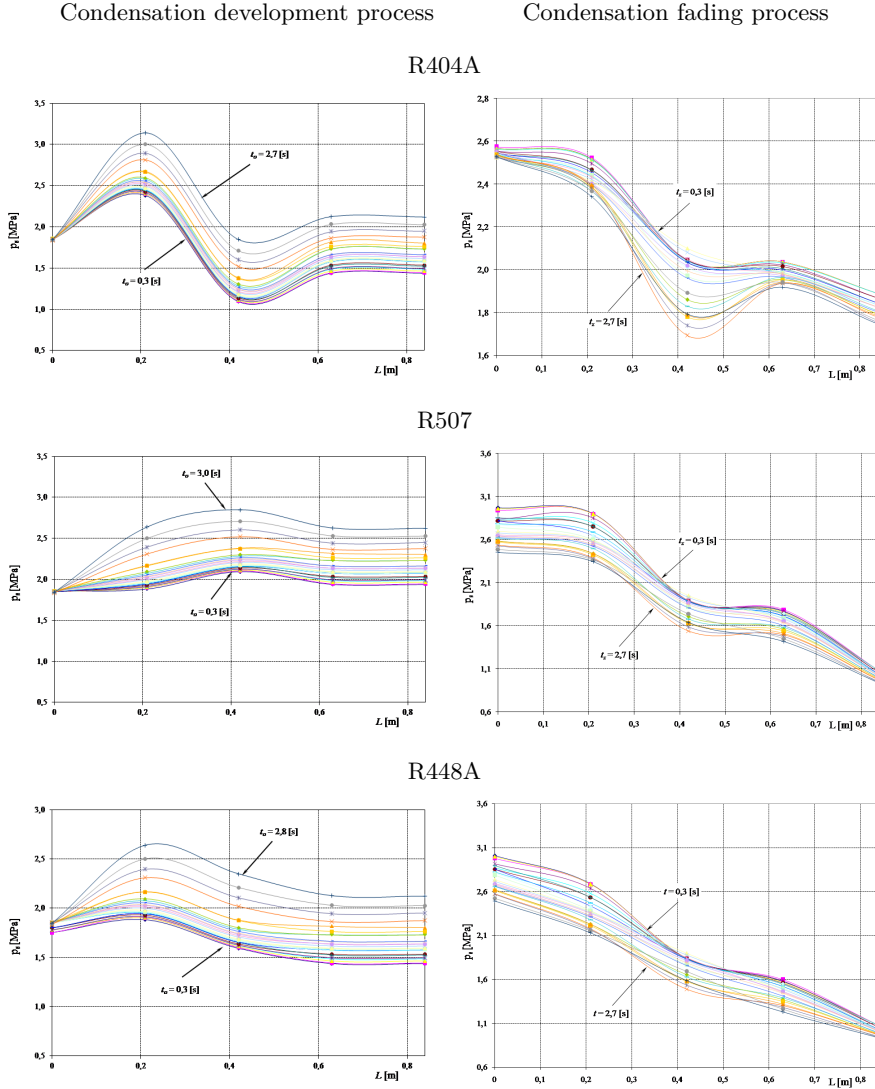
Figure 4: Distribution of pressure of the tested refrigerants depending on the time of closure ($t_c$) and opening ($t_o$) of the shut-off valve for the inner diameter of the tested mini-channel $d = 3.30$ m.

The result of the rapid influx of refrigerant vapors into the mini-channel is the displacement of the pressure change signal, which refers to the speed of propagation of pressure instabilities ($v_p$). Figure 5 illustrates the pressure change signal identified for R404A, R507A, and R448A mixtures.

Condensation development process          Condensation fading process

R404A



R507A



R448A
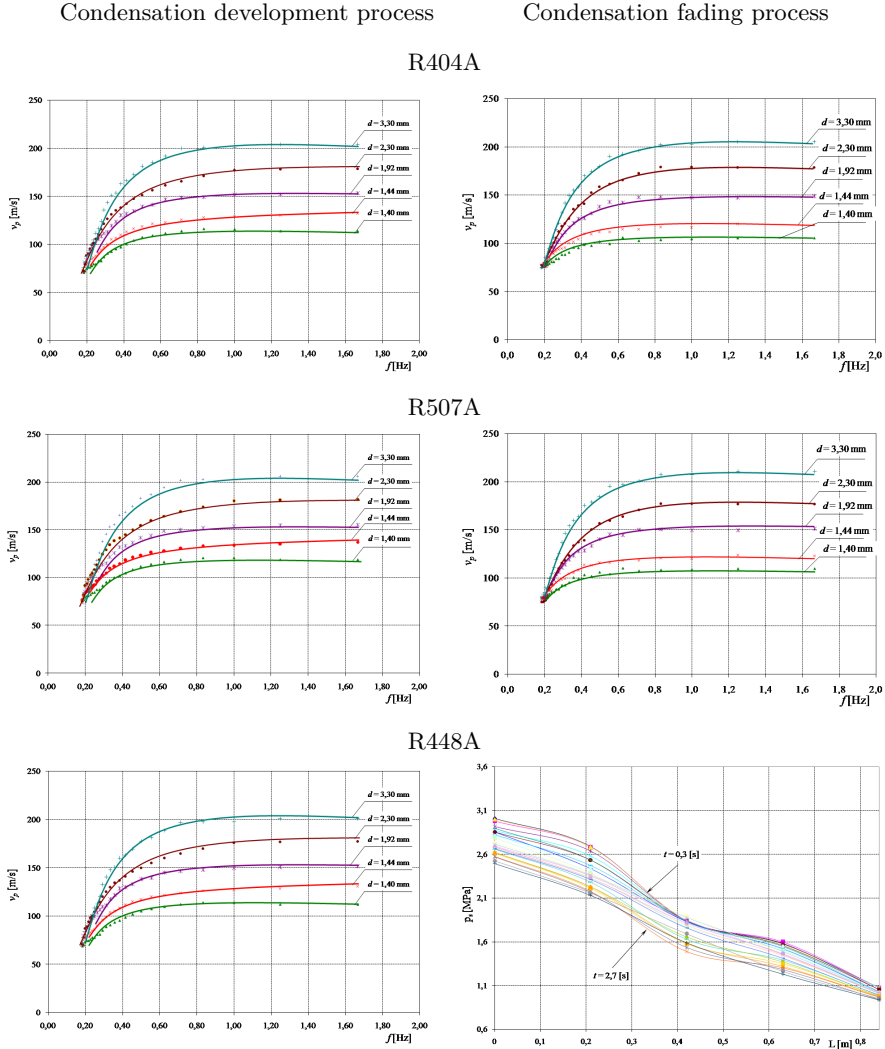


Figure 5: Speed of propagation pressure instabilities depending on the frequency of gener-
ated unit disturbances during liquefaction of tested refrigerants in mini channels
of pipes.

The movement of pressure instabilities ($v_p$) is accompanied by the propa-
gation of temperature instabilities ($v_T$). These are referred to the so-called
the velocity of the condensation front ($v_{FC}$). It was observed that in the
case of the development of the condensation process there is a decrease in
the velocity of propagation of the condensation front, which moved in ac-

cordance with the direction of steam flow in the mini-channel. The decrease in velocity is due to an increase in the frequency of generated disturbances, which corresponds to a decrease in the opening time of the shut-off valve (Fig. 6). On the other hand, when the condensation process disappeared, the instability moved in the direction opposite to the incoming steam, re-
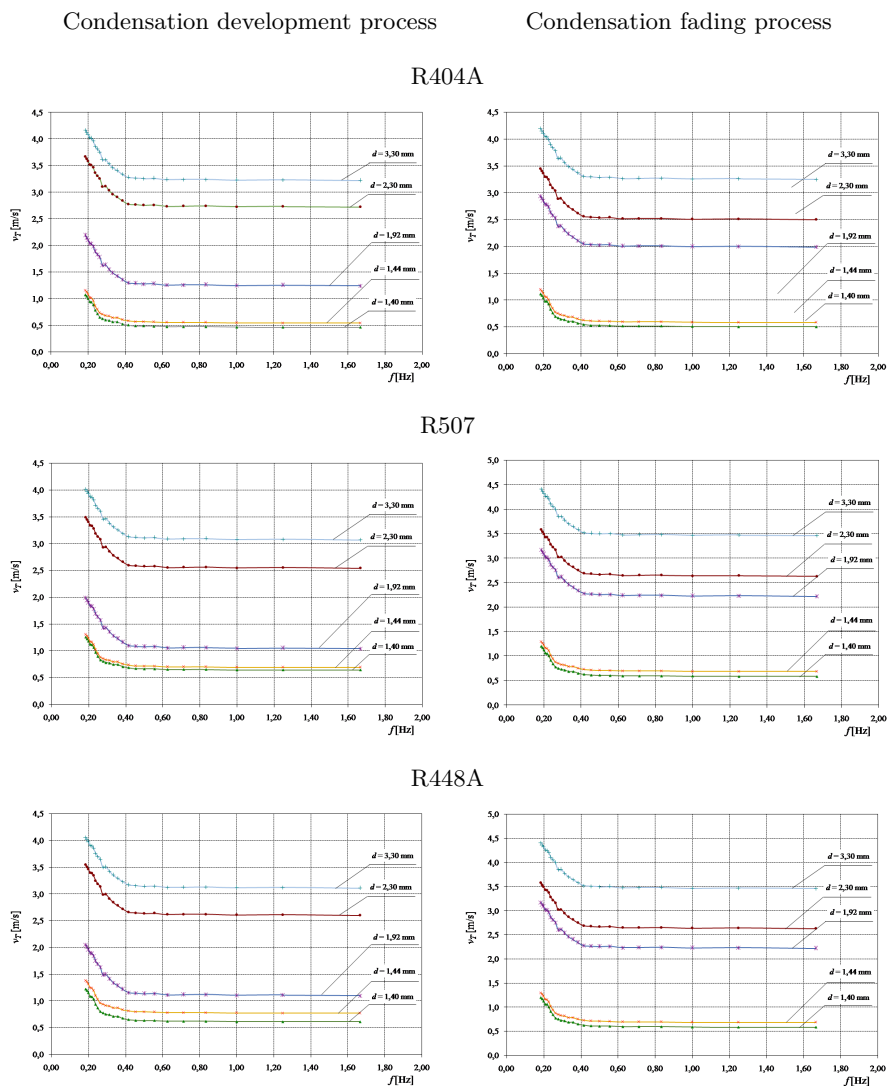


Figure 6: Dependence of the velocity of propagation of temperature instabilities on the frequency of generated unit instabilities for the studied refrigerants.

sulting in a reduction in the most effective area of condensation proper in terms of heat transfer [11, 22, 24, 26]. Figure 7 shows example distributions of pressure and temperature instability precipitates for R134A refrigerants and R1234ze and R1234yf isomers.

Pressure propagation velocity $v_p$     Temperature propagation velocity $v_T$

R134a

R1234yf

R1234ze
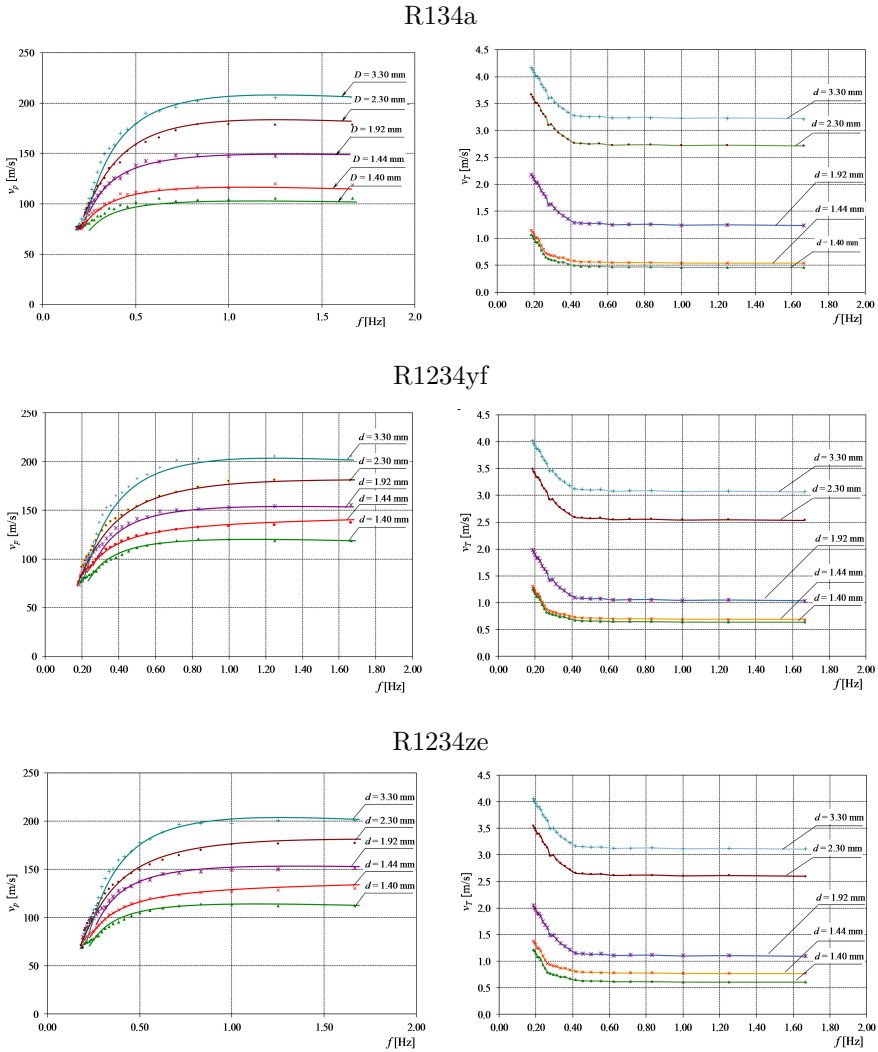
Figure 7: Propagation velocities of pressure ($v_p$) and temperature ($v_T$) instabilities as a function of the frequency of singular instabilities during condensation of tested refrigerants inside tubular mini-channels

# 3    Comparative comparison of computational models describing dynamic instabilities of unit liquefaction of pro-environmental agents in pipe mini-channels

For the studied refrigerants, the application of regression functions for the unit pressure and temperature instabilities occurring during the liquefaction process, the values of the unknowns $C$, $a$, and $b$ were determined according to relations (4) and (7) with the corresponding variance from population ($\sigma^2$) and $r$-Pearson significance coefficients. Example calculation results for the studied refrigerants R448A and R1234yf are presented below.

In the case of the R448A refrigerant, for pressure instabilities occurring during the development of the liquefaction process, the following values were obtained: $C = 327.8$, $a = -0.52$, $b = -1.11$ with a variance of 96% and a significance factor $R = 0.91$. This allowed to, formulate the relationship in the following form:

$$v_p^+ = 327.8 \mathrm{Re}_{\mathrm{TPF}}^{-0.52} \Delta p^{+-1.11}. \tag{9}$$

The results of calculations according to Eq. (9) on the dimensionless velocity $v_p^+{}_{\mathrm{reg}}$ were compared with the results of experimental studies $v_p^+{}_{\mathrm{exp}}$, obtaining satisfactory agreement in the 25% range, as shown in Fig. 8.
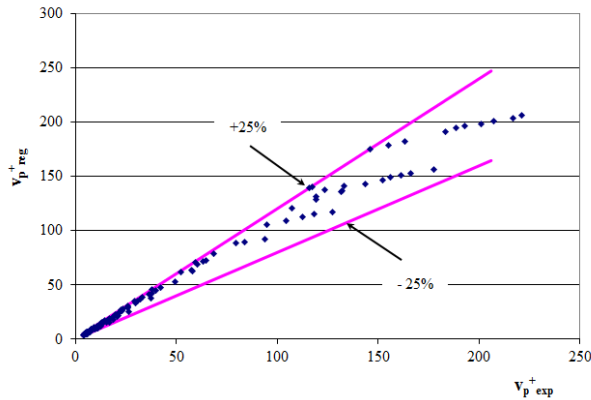


Figure 8: Dependence of dimensionless velocity ($v_p^+{}_{\mathrm{reg}}$) from the value obtained in experimental studies ($v_p^+{}_{\mathrm{exp}}$) for R448A refrigerant during the development of the condensation process.

Figure 9 presents the correlations obtained by means of applied statistical software for the parameters on which the regression model was based.
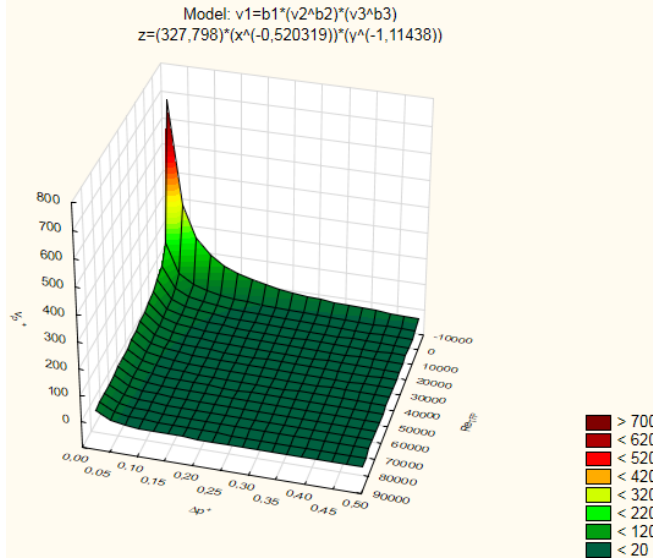


Figure 9: Interdependence of quantities forming the regression model ($V_p^+$, $\Delta p^+$, $\mathrm{Re_{TPF}}$, Eq. (9)) for R448A refrigerant during the development of the condensation process.

Analogous to the regression model of pressure instabilities, the values of the constants of the equation describing the dimensionless velocity speed of propagation of temperature instabilities were determined $v_T^+$ for the refrigerant R1234yf. The following values were obtained: $C = 0.00079$; $a = 0.34$; $b = -1.43$; with a variance of 98% and significance coefficient $R = 0.99$. Consequently, the following form of the regression function was obtained:

$$v_T^+ = 0.00079\mathrm{Re_{TPF}^{0.34}}\Delta T^{+^{-1.43}}. \tag{10}$$

Comparison of computational results obtained from relation (10) with experimental results showed a concordance of $\pm 25\%$ (Fig. 10). Figure 11 shows the correlations obtained by means of applied statistical software for the parameters on which the regression relationship was formulated for speed $v_{T\,\mathrm{reg}}^+$ in condensing refrigerant R1234yf.

Table 1 presents a summary of the quantities that form correlations, describing the dimensionless speed of propagation of pressure $(v_p^+)$ and temperature $(v_T^+)$ instabilities developed for refrigerants R134a, R1234yf,
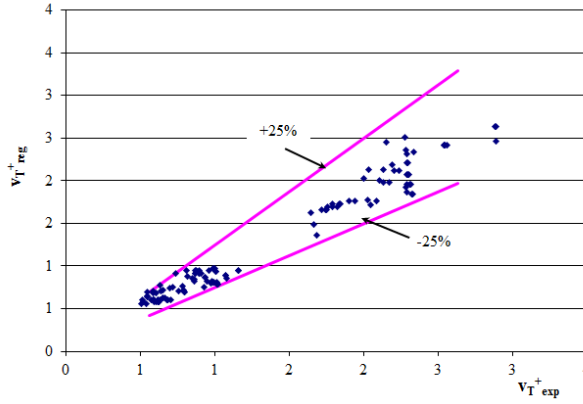
Figure 10: Dependence of dimensionless velocity $v^+_{T\,\mathrm{reg}}$ from the value obtained in experimental studies $v^+_{T\,\mathrm{exp}}$ for the refrigerant R1234yf, during the development of the condensation process.
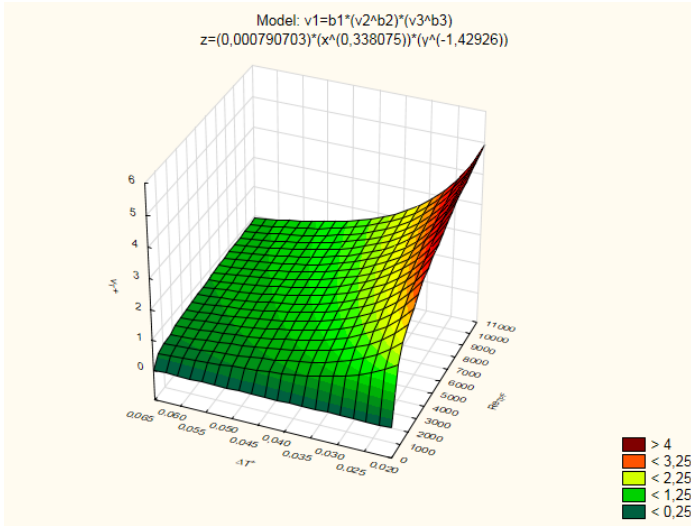


Figure 11: Interdependence of quantities forming the regression model ($V^+_T$, $\Delta T^+$, $\mathrm{Re_{TPF}}$, Eq. (10)) for R1234yf refrigerant during the development of the condensation process.

R1234ze, R404A, R507, and R448A. The tabular statement also indicates the range of accuracy of comparison of calculation results ($v^+_{p\,\mathrm{reg}}$) with experimental ($v^+_{p\,\mathrm{exp}}$). It was within the range of $\pm25\%$.

Table 1: Summary of computational correlations describing quantities $v_p^+$ and $v_T^+$ for the tested refrigerants.

**Regression model of impulsive pressure instabilities** $v_p^+ = C \cdot \mathrm{Re}_{TPF}^a \cdot (\Delta p^+)^b$

| The model refers to | | | R134a | R1234yf | R1234ze | R404A | R507 | R448A |
|---|---|---|---|---|---|---|---|---|
| rapid development of the condensation process | Values of unknowns | $C$ | $18.52 \cdot 10^5$ | $1.85 \cdot 10^{-6}$ | $3.29 \cdot 10^6$ | 302.96 | $4.67 \cdot 10^9$ | 327.8 |
| | | $a$ | -1.06 | -1.06 | -1.05 | -0.48 | -2.27 | -0.52 |
| | | $b$ | 1.05 | 1.05 | 1.72 | -1.05 | 1.33 | -1.11 |
| | Significance coefficient $r$-Pearson | | 0.99 | 0.93 | 0.99 | 0.99 | 0.99 | 0.91 |
| | Variance from population $\sigma^2$ | | 99% | 87% | 99% | 98% | 98% | 96% |
| | Scope of model compatibility | | ±20% | ±20% | ±20% | ±25% | ±25% | ±25% |
| rapid disappearance of the condensation process | Values of unknowns | $C$ | $46.22 \cdot 10^4$ | $38.36 \cdot 10^{-4}$ | $95.54 \cdot 10^4$ | 85.95 | 34.6 | 16.46 |
| | | $a$ | -0.94 | -0.90 | -0.99 | 0.0095 | 0.12 | 0.18 |
| | | $b$ | 0.84 | 0.85 | 0.89 | -1.034 | -1.04 | -0.80 |
| | Significance coefficient $r$-Pearson | | 0.98 | 0.93 | 0.99 | 0.97 | 0.96 | 0.97 |
| | Variance from population $\sigma^2$ | | 97% | 97% | 99% | 93% | 91% | 93% |
| | Scope of model compatibility | | ±20% | ±20% | ±20% | ±20% | ±20% | ±20% |

**Regression model of impulsive temperature instabilities** $v_T^+ = C \cdot \mathrm{Re}_{TPF}^a \cdot (\Delta T^+)^b$

| The model refers to | | | R134a | R1234yf | R1234ze | R404A | R597 | R448A |
|---|---|---|---|---|---|---|---|---|
| rapid development of the condensation process | Values of unknowns | $C$ | 0.00079 | 0.00079 | $1.78 \cdot 10^{-6}$ | $3.04 \cdot 10^{14}$ | $7.58 \cdot 10^{11}$ | $9.97 \cdot 10^{11}$ |
| | | $a$ | 0.34 | 0.34 | -0.99 | -2.49 | -2.20 | -2.28 |
| | | $b$ | -1.43 | -1.43 | 0.89 | 3.93 | 2.80 | 2.64 |
| | Significance coefficient $r$-Pearson | | 0.99 | 0.99 | 0.99 | 0.96 | 0.99 | 0.95 |
| | Variance from population $\sigma^2$ | | 98% | 98% | 99% | 92% | 98% | 96% |
| | Scope of model compatibility | | ±20% | ±25% | ±25% | ±20% | ±20% | ±20% |
| rapid disappearance of the condensation process | Values of unknowns | $C$ | 29.42 | 0.014 | 0.013 | $101 \cdot 10^9$ | $4.67 \cdot 10^9$ | $1.54 \cdot 10^9$ |
| | | $a$ | 0.65 | -0.23 | -0.20 | -2.47 | -2.67 | -2.13 |
| | | $b$ | 2.97 | -1.99 | -1.79 | 1.85 | 1.33 | 1.22 |
| | Significance coefficient $r$-Pearson | | 0.99 | 0.99 | 0.99 | 0.96 | 0.99 | 0.99 |
| | Variance from population $\sigma^2$ | | 98% | 98% | 98% | 89% | 98% | 98% |
| | Scope of model compatibility | | ±20% | ±25% | ±20% | ±20% | ±20% | ±20% |

# 4   Conclusions

The paper proposes proprietary computational models for determining the propagation velocity of pressure and temperature instabilities during the development or disappearance of the liquefaction process of existing and new environmentally friendly refrigerants. The proposed calculation methods were based on a regression function in which the expected value of the explained variable depends on the explanatory variables. In the case under consideration, the explanatory variable was the value of the propagation velocity of a given instability, while the explanatory variables were related to the parameters of the system.

Simple dimensional analysis procedures were used, taking into account the Buckingham $\Pi$ theorem. A general form of the regression function was obtained with the help of the values of the dimensionless velocity of propagation of pressure instabilities and the dimensionless velocity propagation of temperature instabilities for different refrigerants. Calculations made according to the developed models were compared with experimental studies. Satisfactory agreement was shown, within $\pm 25\%$, for all analyzed factors. This result should be considered satisfactory and testifies to the applicability of the developed regression models for the computational determination of the propagation speed of pressure and temperature instabilities originating from unitary dynamic interactions. The 25% accuracy interval value for two-phase flows is a very good result in two-phase flow technology, as indicated in the industry literature.

The methodology proposed by the author makes it possible to calculate significant quantities (the dimensionless velocities of propagation of pressure and temperature instabilities) in describing the dynamic unit instabilities that occur in the liquefaction process in mini-channels. Using a relatively simple method, important information was obtained that effectively fills a gap in the literature.

It should be emphasized that the proposed methodology can be applied to new agents that are replacements for phased-out F-gases.

*Received 17 January 2023*

# References

[1] Benzi R., Sutera A., Vulpiani A.: *The mechanism of stochastic resonance.* J. Phys. A: Math. Gen. **14**(1981), 1453–l457.

[2] Bergles A.E., Kandlikar S.G.: *On the nature of critical heat flux in microchannels.* J. Heat Transfer-T ASME **127**(2005), 1, 101–107.

[3] Daisuke J., Mikajiri N., Nobunaga M., Inoue N.: *Condensation heat transfer of pure refrigerants R1234yf and R32 inside multiple circular minichannels.* Int. J. Heat Mass Tran. **195**(2022), 123146.

[4] Darcy D.F.: *On acoustic propagation and critical mass flux in two-phase flow.* J. Heat Transfer-T ASME **93**(1971), 4, 413–421.

[5] Fauve S., Heslot F.: *Stochastic resonance in a bistable system.* Phys. Lett. A **97**(1983), 1–2, 5–7.

[6] Gammaitoni L., Hänggi P., Jung P., Marchesoni F.: *Stochastic resonance.* Rev. Mod. Phys. **70**(1998), 1, 223–287.

[7] Ghiaasiaan S.M.: *Two-Phase Flow, Boiling, and Condensation in Conventional and Miniature Systems.* Cambridge Univ. Press, 2008.

[8] Gmurman W.J.: *Probability and Mathematical Statistics.* WNT, Warszawa 1975.

[9] Gubaidullin D.A., Gubaidullina D.D., Fedorov Y.V.: *About the equilibrium speed of sound in a liquid with gas-vapor bubbles.* J. Phys.: Conf. Ser. **669**(2016), 1, 012011. doi: [10.1088/1742-6596/669/1/012011](10.1088/1742-6596/669/1/012011)

[10] Hanamura K., Kaviany M.: *Propagation of condensation front in steam injection into dry porous media.* Int. J. Heat Mass Tran. **38**(1995), 8, 1377–1386.

[11] Helmholtz H.: Verhandlungen des Naturhistorisch-medizinischen Vereins zu Heidelberg, **III(**1863), 16.

[12] Kuczyński W., Charun H., Piątkowski P., Bałasz B., Chliszcz K.: *A regressive model for dynamic impulsive instabilities during the condensation of R134a, R1234ze(E) and R1234yf refrigerants.* Int. J. Heat Mass Tran. **169**(2021), 120963.

[13] Kuczyński W., Charun H., Bohdal T.: *Impact of periodically generated hydrodynamic disturbances on the condensation efficiency of R134a refrigerant in pipe minichannels.* Exp. Heat Transfer **26**(2013), 1, 64–84.

[14] Kuczyński W., Charun H.: *Modeling of a two-phase region length of the condensation of R134a and R404A refrigerants in pipe minichannels with periodic hydrodynamic instabilities.* Heat Transfer Eng. **35**(2014), 9, 850–862.

[15] Kuo C.-J., Peles Y.: *Flow boiling instabilities in microchannels and means for mitigation by reentrant cavities.* J. Heat Transfer-T. ASME **130**(2008), 7, 072402. (Also Department of Mechanical, Aerospace and Nuclear Engineering, Rensselaer Polytechnic Institute, Troy, NY 12180, **130**(2008)).

[16] Longo G., Mancin S., Righetti G., Zilio C.: *Saturated vapour condensation of R134a inside a 4 mm ID horizontal smooth tube: Comparison with the low GWP substitutes R152a, R1234yf and R1234ze(E).* Int. J. Heat Mass Tran. **133**(2019), 461–473.

[17] López-Belchí A.: *Assessment of a minichannel condenser at high ambient temperatures based on experimental measurements working with R134a, R513A and R1234yf.* Appl. Therm. Eng. **155**(2019), 341–353.

[18] Mainil A.K., Sakamoto N., Ubudiyah H., Miyara A., Kariya K.: *Experimental study and general correlation for frictional pressure drop of two-phase flow inside microfin tubes.* Int. J. Refrig. **144**(2022), 342–353.

[19] Moody F.J.: *A pressure of pulse model for two-phase critical flow and sonic velocity.* J. Heat Transfer-T. ASME **91**(1969), 3, 371–384.

[20] Pham Q.V., Oh J.-T.: *Condensation heat transfer characteristics of R1234yf inside multiport minichannel tube.* Int. J. Heat Mass Tran. **170**(2021), 121029.

[21] Shin J.S., Kim M.H.: *An experimental study of condensation heat transfer inside a minichannel with a new measurement technique.* Int. J. Multiphas. Flow **30**(2004), 311–325.

[22] Teng R., Cheng P., Zhao T.S.: *Instability of condensate film and capillary blocking in small-diameter-thermosyphon condensers.* Int. J. Heat Mass Tran. **42**(1999), 16, 3071–3083.

[23] Wang L., Jiao P., Dang Ch., Hihara E., Dai B.: *Condensation heat and mass transfer characteristics of low GWP zeotropic refrigerant mixture R1234yf/R32 inside a horizontal smooth tube: An experimental study and non-equilibrium film model development.* Int. J. Therm. Sci. **170**(2021), 107090.

[24] Weisman J., Ake T., Knott R.: *Two-phase pressure drop across abrupt area changes in oscillatory flow.* Nucl. Sci. Eng. **61**(1976), 3, 297–309.

[25] Welander P.: *On the oscillatory instability of a differentially heated loop.* J. Fluid. Mech. **29**(1967), 1, 17–30.

[26] Yuncu H., Yildirim O.T., Kakac S.: *Two-phase flow instabilities in a horizontal single boiling channel.* J. Appl. Sci. Res. **48**(1991), 83–104.

# Notes for Contributors

ARCHIVES OF THERMODYNAMICS publishes original papers which have not previously appeared in other journals. The journal does not have article processing charges (APCs) nor article submission charges. The language of the papers is English. The paper should not exceed the length of 25 pages. All pages should be numbered. The plan and form of the papers should be as follows:

1. The heading should specify the title (as short as possible), author, his/her complete affiliation, town, zip code, country and e-mail. Please indicate the corresponding author. The heading should be followed by *Abstract* of maximum 15 typewritten lines and *Keywords*.

2. More important symbols used in the paper can be listed in *Nomenclature*, placed below *Abstract* and arranged in a column, e.g.:
   $u$ – velocity, m/s
   $v$ – specific volume, m/kg
   etc.
   The list should begin with Latin symbols in alphabetical order followed by Greek symbols also in alphabetical order and with a separate heading. Subscripts and superscripts should follow Greek symbols and should be identified with separate headings. Physical quantities should be expressed in SI units (*Système International d'Unités*).

3. All abbreviations should be spelled out first time they are introduced in the text.

4. The equations should be each in a separate line. Standard mathematical notation should be used. All symbols used in equations must be clearly defined. The numbers of equations should run consecutively, irrespective of the division of the paper into sections. The numbers should be given in round brackets on the right-hand side of the page.

5. Particular attention should be paid to the differentiation between capital and small letters. If there is a risk of confusion, the symbols should be explained (for example *small c*) in the margins. Indices of more than one level (such as $B_{f_a}$) should be avoided wherever possible.

6. Computer-generated figures should be produced using **bold lines and characters**. No remarks should be written directly on the figures, except numerals or letter symbols only. Figures should be as small as possible while displaying clearly all the information requires, and with all lettering readable. The relevant explanations can be given in the caption.

7. The figures, including photographs, diagrams, etc., should be numbered with Arabic numerals in the same order in which they appear in the text. Each figure should have its own caption explaining the content without reference to the text.

8. Computer files on an enclosed disc or sent by e-mail to the Editorial Office are welcome. The manuscript should be written as a MS Word file – *∗.doc*, *∗.docx* or LaTeX file – *∗.tex*. For revised manuscripts after peer review process, figures should be submitted as separate graphic files in either vector formats (PostScript (PS),

Encapsulated PostScript (EPS), preferable, CorelDraw (CDR), etc.) or bitmap formats (Tagged Image File Format (TIFF), Joint Photographic Experts Group (JPEG), etc.), with the resolution not lower than 300 dpi, preferably 600 dpi. These resolutions refer to images sized at dimensions comparable to those of figures in the print journal. Therefore, electronic figures should be sized to fit on single printed page and can have maximum 120 mm x 170 mm. Figures created in MS World, Exel, or PowerPoint will not be accepted. The quality of images downloaded from websites and the Internet are also not acceptable, because of their low resolution (usually only 72 dpi), inadequate for print reproduction.

9. The references for the paper should be numbered in the order in which they are called in the text. Calling the references is by giving the appropriate numbers in square brackets. The references should be listed with the following information provided: the author's surname and the initials of his/her names, the complete title of the work (in English translation) and, in addition:

   (a) for books: the publishing house and the place and year of publication, for example:

   [1] `Holman J.P.:` *`Heat Transfer`*`. McGraw-Hill, New York 1968.`

   (b) for journals: the name of the journal, volume (Arabic numerals in bold), year of publication (in round brackets), number and, if appropriate, numbers of relevant pages, for example:

   [2] `Rizzo F.I., Shippy D.I.:` *`A method of solution for certain problems of transient heat conduction`*`. AIAA J.` **`8`**`(1970), No.11, 2004–2009.`

   For works originally published in a language other than English, the language should be indicated in parentheses at the end of the reference.

   Authors are responsible for ensuring that the information in each reference is complete and accurate.

10. As the papers are published in English, the authors who are not native speakers of English are obliged to have the paper thoroughly reviewed language-wise before submitting for publication.

**Manuscript submission**   Manuscripts to be considered for publication should be electronically submitted to the Editorial Office via the online submission and reviewing system, the Editorial System, at http://www.editorialsystem.com/aot. Submission to the journal proceeds totally on line and you will be guided stepwise throughout the process of the creation and uploading of your files. The body of the text, tables and figures, along with captions for figures and tables should be submitted separately. The system automatically converts source files to a single PDF file article, for subsequent approval by the corresponding Author, which is then used in the peer-review process. All correspondence, including notification confirming the submission of the manuscripts to the Editorial Office, notification of the Editors's decision and requests for revision, takes place by e-mails. Authors should designate the corresponding author, whose responsibility is to represent the Authors in contacts with the Editorial Office. Authors are requested not to submit the manuscripts by post or e-mail.

The illustrations may be submitted in color, however they will be printed in black and white in the journal, so the grayscale contributions are preferable. Therefore, the figure

caption and the entire text of the paper should not make any reference to color in the illustration. Moreover the illustration should effectively convey author's intended meaning when it is printed as a halftone. The illustrations will be reproduced in color in the online publication.

**Further information** All manuscripts will undergo some editorial modification. The paper proofs (as PDF file) will be sent by e-mail to the corresponding author for acceptance, and should be returned within two weeks of receipt. Within the proofs corrections of minor and typographical errors in: author names, affiliations, articles titles, abstracts and keywords, formulas, symbols, grammatical error, details in figures, etc., are only allowed, as well as necessary small additions. The changes within the text will be accepted in case of serious errors, for example with regard to scientific accuracy, or if authors reputation and that of the journal would be affected. Submitted material will not be returned to the author, unless specifically requested.
A PDF file of published paper will be supplied free of charge to the Corresponding Author.

Submission of the manuscript expresses at the same time the authors consent to its publishing in both printed and electronic versions.

**Transfer of Copyright Agreement** Submission of the manuscript means that the authors automatically agree to assign the copyright to the Publisher. Once a paper has been accepted for publication, as a condition of publication, the authors are asked to send by email a scanned copy of the signed original of the Transfer of Copyright Agreement, signed by the Corresponding Author on behalf of all authors to the Managing Editor of the Journal. The copyright form can be downloaded from the journal's website at http://www.imp.gda.pl/archives-of-thermodynamics/ under Notes for Contributors.

*The Editorial Committee*